博士論文

Development of High-sensitivity Optical Fiber Ultrasonic Sensing Systems for Structural Health Monitoring of CFRP Laminates

(CFRP 積層板の構造ヘルスモニタリングのための高感度光ファイバ超音波センシングシステムの開発)

呉　奇

To my dearest family

ABSTRACT

In this dissertation, systematic theoretical and experimental studies of three ultrasonic optical fiber sensing systems for structural health monitoring of carbon fiber reinforced plastic (CFRP) laminates with their practical applications are presented. These works aim to provide effective solutions to the practical existed problems, including the bandwidth, sensitivity, robustness and system cost, in the interdisciplinary research on optical fiber sensor, ultrasonic detection, composites, and structural health monitoring.

Firstly, a phase-shifted fiber Bragg grating (PS-FBG) is designed and simulated for resolving the conflicts between the effective grating length and grating slope in normal fiber Bragg grating (FBG). According to the simulation results, this special FBG achieves high sensitivity and broad bandwidth simultaneously. Furthermore, experimental researches on its sensitivity distribution properties and related attachment methods direct its application in ultrasonic structural health monitoring.

Based on the PS-FBG sensor, a cascaded PS-FBGs sensing system is proposed and evaluated. Due to its high sensitivity, broad bandwidth and multiplexing ability, this system is suitable for acousto-ultrasonic detections. Real-time detection of ultrasonic Lamb wave in CFRP laminates with modes discrimination ability is achieved by this technique.

In order to improve the sensitivity further for accomplishment of acoustic emission (AE) detection in CFRP laminate, a PS-FBG balanced sensing system is proposed and evaluated. Its sensitivity is improved by balanced demodulation technique; thus it can detect small AE signals, such as transverse crack AE signals. From the results of AE tensile test, Kaiser Effect and Felicity Effect are demonstrated. Discrimination of different damage types are also discussed based on the waveform analysis. From the results of AE three point bending test, the waveforms and continuous wavelet transform results are analyzed further, while position identification ability of this sensing system is verified.

Then, erbium fiber ring laser sensing system with inbuilt PS-FBG is designed not only to fulfill the requirement of robustness, but also improve the sensitivity and bandwidth further. A dynamic model of this laser is proposed and simulated. The experimental results, which fit the simulation prediction very well, shows the sensitivity of this system is about 20 dB higher and the bandwidth is up to 7 MHz compared to traditional piezoelectric ceramic sensor.

Finally, in the summary of this dissertation, these systems are compared, especially, about their applications. These novel sensing techniques have potentials to improve not only the safety of composites, but also the safety of people's lives.

Key words: optical fiber sensor, structural health monitoring, composites, ultrasonic detection.

CONTENTS

INDEX

Figure List

IV

v

Table List

1 INTRODUCTIONS

1.1   Ultrasonic Structural Health Monitoring in Composites

In recent years, composite materials, such as carbon-fiber-reinforced plastic (CFRP), are widely applied in many practical fields, such as aircraft. Composite materials usually consist two parts, which are matrix and reinforcement. In the case of CFRP, the reinforcement is carbon fiber which provides the strength; while the matrix is usually a polymer resin to bind the reinforcement together. In this dissertation, the detection object is mainly CFRP laminate.
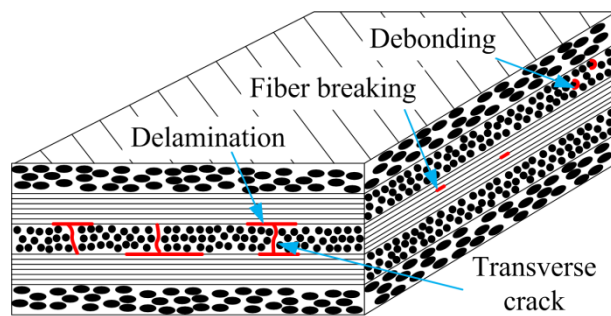
Figure 1.1. Damage types in CFRP laminate.

The CFRP laminate shows some unique mechanical characteristics. It has high strength-to-weight ratio and very good rigidity. On the other hand, unlike isotropic materials such as aluminum or steel, CFRP laminate shows directional properties, depending on the layouts of the carbon fiber and proportion of the carbon fiber and polymer resin. The other problems in the CFRP laminate are the various damage types and complex damage process. The damage types in CFRP laminates include transvers cracks, delaminations, debondings, fiber breakings, *etc*. [1-5]. Figure 1.1 shows some typical damage types in CFRP laminate. It is very difficult to predict and avoid these damages of CFRP laminate. Therefore, monitoring the health condition in CFRP laminates is very important to maintain the performance of the composite materials. Therefore, structural health monitoring (SHM) has been needed. Additionally, non-destructive testing (NDT) is also necessary to check the health condition of CFRP laminates.

Among many SHM or NDT methods, acousto-ultrasonic detection and acoustic emission (AE) detection are mature and widely used techniques, which both use ultrasonic waves to detect and evaluate damages. These two techniques are also the main ultrasonic detection methods discussed in this dissertation. Acousto-ultrasonic detection is an active detection, in which ultrasonic wave is compulsorily generated by transducers and picked up by other transducers under control, as shown in Figure 1.2(a) [6-8]. By analyzing the amplitude attenuation or waveform change, researchers can evaluate the damages in CFRP laminate quantitatively. On the other hand, AE

detection is a passive detection [9-14]. It detects the ultrasonic pulses spontaneously emitted from a defect in the moment of its occurrence, as shown in Figure 1.2(b). By analyzing parameters of cumulative hits, energy distribution, peak frequency, *etc.*, researchers can predict the damage conditions in CFRP laminate or evaluate it qualitatively. Ultrasonic waves in these methods usually have high frequency and weak amplitude. Especially, in the case of AE detection, frequency range is from about 1 kHz to 1 MHz and strain is in the sub-micron level. Therefore, there are two fundamental requirements to the sensing system for detecting ultrasonic waves: broad bandwidth and high sensitivity.
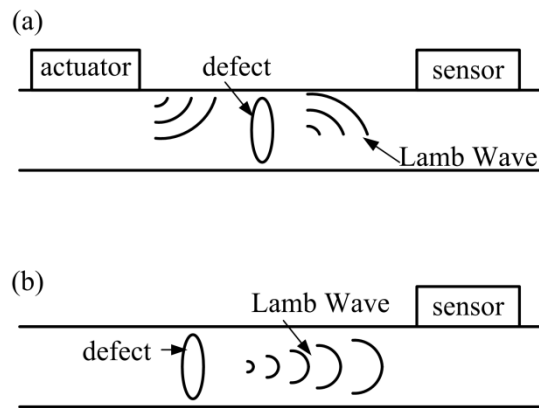
Figure 1.2. Ultrasonic SHM methods. (a) acousto-ultrasonic detection; (b) AE detection.

Furthermore, in the ultrasonic SHM of composite, the detection objects always have plate-like shape [12, 15, 16]. When the thickness of a plate (CFRP laminate) is comparable with or smaller than the wavelength of the ultrasonic wave, i.e., the propagated ultrasonic wave is confined by the dimension of a plate, the ultrasonic wave is a Lamb wave, one kind of guided wave [17-22]. Lamb wave is firstly described by the English Mathematician Horace Lamb in 1917. Unlike other ultrasonic waves with relative short propagation distance, the Lamb wave can propagate a substantially long distance with low attenuation. Due to this important characteristic, the Lamb wave is an ideal ultrasonic wave in SHM or NDT for investigating a large area. The other important characteristic of Lamb wave is dispersion, i.e., the different-frequency wave components have different phase velocities and different group velocities under certain thickness of the plate, leading to the difficulty of analysis. Naturally, based on the presentation of the wave traits, the Lamb wave can be separated into two groups, which are symmetric modes (S modes) and anti-symmetric modes (A mode), as shown in Figure 1.3(a) and (b). In some references, the A mode is also called flexural mode, while the S mode is also called extensional mode. These modes are important in certain discussion because the modes of the Lamb wave contain much useful information to the ultrasonic SHM.
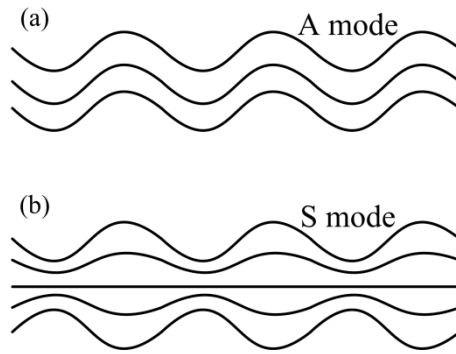
Figure 1.3. Mode types of Lamb wave. (a) Asymmetric mode; (b) Symmetric mode.

1.2 Optical Fiber Sensor for Ultrasonic Detection

Lead-zirconate-titanate (PZT) is a traditional ultrasonic transducer, which satisfies the requirement of high sensitivity and broad bandwidth in ultrasonic SHM [23, 24]. It can transform strain with voltage. In detail, as a sensor, it generates the voltage when its shape is changed by applied strain. On the other hand, as actuator, its shape changes under the certain applied voltage signals. The PZT transducer can be manufactured to different sizes and different shapes, including traditional piezoelectric sensor, piezoelectric wafer, *etc*., according to different specific applications and requirements. However, these sensors also exist some inherent disadvantages, such as bulk size and heavy weight to traditional piezoelectric sensor, easiness of fragile to piezoelectric wafer, and susceptibility to electromagnetic interference (EMI) to all the PZT sensors. Additionally, macro fiber composite (MFC) is an ultrasonic transducer invented by NASA in 1996, which is flexible, durable and relative embeddable [25-27]. However, it as well suffers the problem of EMI due to the fact that the active material in MFC is still piezoceramic material. Figure 1.4 shows several traditional sensors. The two PZT transducers and MFC are used and discussed in this dissertation.
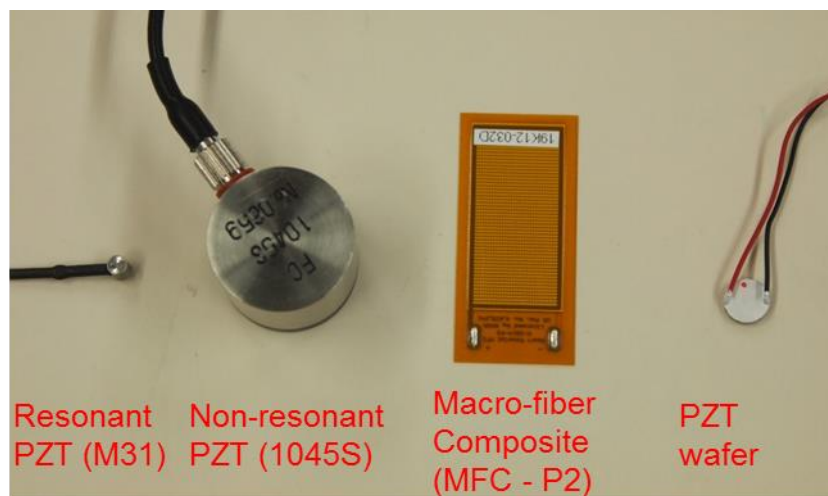
Figure 1.4. Traditional sensors, such as PZTs, MFC and piezoelectric wafer.

In order to solve these above mentioned problems, researchers have investigated optical fiber sensors (OFSs), which is also called fiber optic sensors (FOSs), as effective alternatives due to their advantages of flexibility, immunity to EMI, corrosion resistance, and ability to be embedded into various materials. Optical fiber was predicted by Dr. Kao who was awarded Nobel Prize in Physics in 2009, and was firstly manufactured by Corning Incorporated. In the end of 20th century, the optical fiber technique developed very quickly and many different and useful fiber optical components were designed and manufactured. These optical fiber techniques largely changed people's lives. Especially, the optical communication has become the fundamental technique in today's society. When time goes to 21st century, the other application of optical fiber, such as a sensor, is explored and attempted. Many physical parameters can be measured by OFSs.
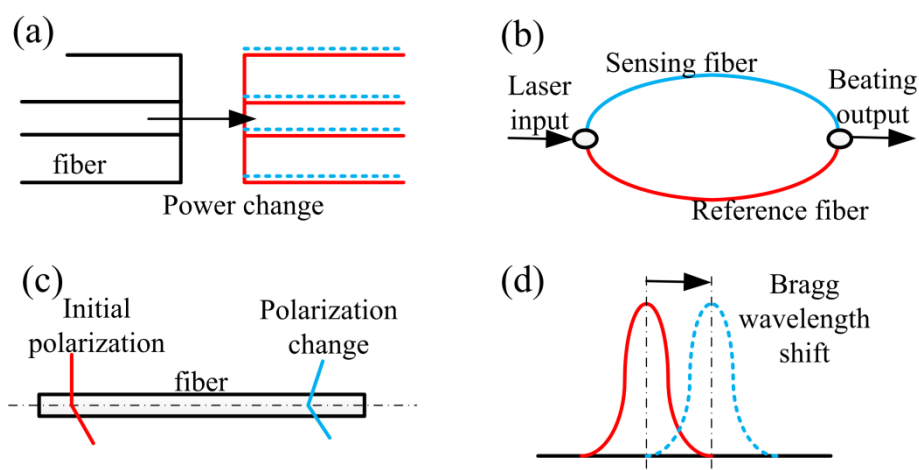
Figure 1.5. Four types of ultrasonic OFSs based on (a) intensity change, (b) interferometer, (c) polarimetric heterodyning, and (d) fiber Bragg grating.

OFSs for measuring static parameters, especially strain and temperate, have been deeply researched, and already commercialized for practical use. However, ultrasonic OFSs are still need to be studied due to some unsolved problems. Herein, we briefly introduce the existed ultrasonic OFS techniques and their corresponding advantages and disadvantages. To the author's knowledge, there are basically four types of ultrasonic OFSs, as shown in Figure 1.5 [8].

The first type of ultrasonic OFS is based on the change of optical intensity. The sensing element suffers different loss when it is influenced by ultrasonic waves. By monitoring the intensity change, the ultrasonic wave can be detected. Based on this concept, the sensing element could be optical coupler [28], optical fiber bending [29], optical fiber misalignment [30], *etc*. However, these techniques have very low sensitivity because the optical power change is very small when the sensing element is compressed, extended or misaligned by small signals.

The second type of ultrasonic OFS is based on interferometer. These interferometers include the designs of Mach-Zender [31], Fabry–Perot [32],

Michelson [33], Sagnac [34], *etc*. This sensing technique can achieve very high sensitivity, but the disadvantage is also apparent. They are very sensitive to static temperature change or strain change; as a result, feedback controller is the additional necessary components, which increase the system cost. Furthermore, because the whole sensing fiber can detect ultrasonic waves, it is difficult to judge the arrival time of the ultrasonic wave which is very important to the position identification in certain SHM applications [35].

The third type of ultrasonic OFS is based on polarimetric heterodyning [36]. The polarization of the fiber will change under the influence of ultrasonic wave. After polarization beating, the ultrasonic signals will be shown. The most successful design according to this theory is polarimetric heterodyning, including the distributed Bragg reflector laser and distributed feedback laser. The advantage of this technique is the ultra-high detectable frequency. However, in the case of SHM, the ultrasonic wave is difficult to couple into the fiber in the transverse direction, where polarization status of the fiber barely changes. Therefore, this type of sensor is more suitable as hydrophone, where the sensor and the object were immersed into water. In other words, it is not suitable to use this sensor in the field of ultrasonic SHM.

The forth type of ultrasonic OFS is based on fiber Bragg grating (FBG) [37-40]. Grating is an optical item with periodical structure which can demodulate the amplitude or/and phase of the input light. When the grating is written in an optical fiber, which is single mode fiber (SMF) in most cases, FBG is manufactured. More details will be expressed in the section of 2.1. Besides the advantages which other OFS techniques also have, FBG sensor has its own unique advantages. Because the grating is written in a small section of SMF, it is a point-like sensor with small size and be able to judge the arrival time of an ultrasonic wave for position identification. Another advantage is multiplexing ability of OFSs, achieved in certain condition and design. It is helpful to simplify the system design and total cost. Furthermore, another major inherent advantage of FBGs emphasized by published research is that the strain caused by ultrasonic waves is encoded in the Bragg wavelength shift of the FBG, which means that detecting strain is irrelevant to other parameters, such as optical power.

When FBG is used to detect static parameters, the Bragg wavelength shift can be read from the optical spectrum analyzer (OSA). The sensitivity is always restricted by the resolution of OSA in this case. Other demodulation systems to decode the Bragg wavelength shift are used to enhance the sensitivity. However, when FBG sensor is used to detect dynamic parameters, especially the ultrasonic wave which has high frequency, using OSA to read the Bragg wavelength shift is obviously not suitable because of the low response time of OSA. Owing to the same reason, demodulation technique should be improved to process high speed-demodulation ability. Furthermore, as said in section 1.1, high sensitivity is also required for precise detection of the ultrasonic wave with low energy usually.

(a)

ASE → Filter → FBG sensor → PD

(b)

TLS ⟶ FBG sensor ⟶ PD
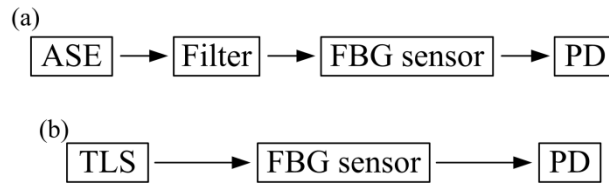
Figure 1.6. Two different FBG ultrasonic demodulation techniques: (a) power detection and (b) edge filter detection.

Nowadays, in order to fit the above mentioned requirements, there are two mainstream methods of using FBG sensors for detecting ultrasonic waves, which are power detection and edge filter detection, as shown in Figure 1.6 [41]. In the power detection method, a broadband light source, such as amplified spontaneous emission (ASE) or super-luminescent diode, is used to illuminate the FBG sensor. A filter, such as an arrayed waveguide grating (AWG) [42-44] and matched FBG [45, 46], is used to demodulate the Bragg wavelength shift of the FBG sensor to optical power fluctuation. This method can achieve multiple channels easily, but it has relative low sensitivity due to the physical nature of the broadband light source. Therefore, this low-cost method is suitable for employment in acousto-ultrasonic detection, where the amplitude of the input signal can be controlled and averaging for noise reduction is also acceptable albeit with expense of lots of time. On the other hand, the edge filter detection method uses a laser as a light source [47-51]. In this system, a tunable laser source (TLS) is adjusted in the linear region of the spectrum of an FBG sensor, which is used as an edge filter. By detecting the reflected or transmitted power of the FBG, the ultrasonic signal can be analyzed. The method has relative high sensitivity because the noise level in TLS is always lower than that in broadband light source. However, multiplexing may be difficult to be satisfied. Recently, pulse interferometry technique was proposed. This technique combines the merits of the power detection method and the edge filter detection method, but high cost is also an issue that must be considered in practical applications [52]. In addition, the sensitivity in this method is comparable to, rather than higher than that of, normal edge filter detection. More information and more introductions on previous researches of demodulation systems will be introduced in beginning of Chapter 3 and 4.

The demodulation technique is very important. It decides the performance and the properties of the whole optical fiber sensing system on a large extent. Furthermore, selecting the most suitable demodulation technique also should be based on certain application field, because each application case has its different demands.

1.3   Target and Structure of the Dissertation

The main target of my research is to develop novel ultrasonic optical fiber sensing systems for SHM of CFRP laminates. Thus, this dissertation includes information of composite materials, ultrasonic guided wave, SHM or NDT technique, and fiber optics. In this research, one novel FBG is proposed and simulated to demonstrate its advantages in ultrasonic detection. Based on this special FBG, three different sensing

systems are developed with different characteristics. Their sensitivities and bandwidths, the parameters of which are most important to ultrasonic sensors, are enhanced. As a result, different suitable applications are demonstrated and verified by experiments.

The structure of this doctoral dissertation is briefly explained in this part.

In the first chapter, the background is introduced. Firstly, we clarify the need of ultrasonic SHM in composite materials and show the common methods of ultrasonic SHM. Then, common ultrasonic detection by OFS is discussed. Additionally, the ultrasonic detection based on FBG and relative demodulation technique is introduced. Furthermore, the scope and structure of this research are explained, as well some equipment and software used in this research are also introduced.

In the second chapter, we propose phase-shifted fiber Bragg grating (PS-FBG) for ultrasonic detection. We simulate the spectrum of PS-FBG and compared it to that of normal FBG. Then, we also simulate the response of PS-FBG to longitudinal ultrasonic waves. According to the results, we found that the PS-FBG is very suitable for ultrasonic detection. Furthermore, the sensitivity distribution properties of PS-FBG and attachment method are experimented. Useful results which can direct following researches are obtained and analyzed.

In the third chapter, a sensing system based on broadband light source is proposed and demonstrated. It is called cascaded PS-FBGs sensing system. This sensing system shows broad bandwidth, relative high sensitivity and multiplexing ability. We apply it in impact detection and real-time acousto-ultrasonic detection on CFRP laminate with mode discrimination ability.

In the fourth chapter, we enhance the sensitivity of the PS-FBG ultrasonic sensing system by using a novel designed demodulation technique, which is called balanced sensing technique. We demonstrate its good performance and confirm its practical application to AE detection in composites. In the first tensile test, we prove Kaiser Effect, separate different damage types in composites, according to the cumulative AE hits or energy distributions. In the second tensile test, we compare the AE phenomena in two CFRP laminates with different structures, and try to relate the AE waveforms to actual damage types. In the other experiment, we detect the transverse crack AE signals in three point bending test. We analyze the waveforms, CWT results and prove the position identification ability of this sensing system.

In the fifth chapter, another sensing system based erbium fiber ring laser with inbuilt PS-FBG is proposed and demonstrated. Besides the ultra-high sensitivity and ultra-broad bandwidth, another advantage is the self-adjustment ability. A dynamic model of erbium fiber laser (EFL) is also established and simulated to explain the physical principle and phenomena in ultrasonic detection by this method. We verify that it can detect very small and high-frequency ultrasonic wave in the acousto-ultrasonic detection without any controller.

In the sixth chapter, all the designed sensing systems are compared. The most suitable application area to each design is clarified according to their different advantages and characteristics. Furthermore, the recommendation of future work is proposed.

1.4 Equipment and Software

For easy and brief expression and presentation, some important equipment and software used in this research are introduced in this section.
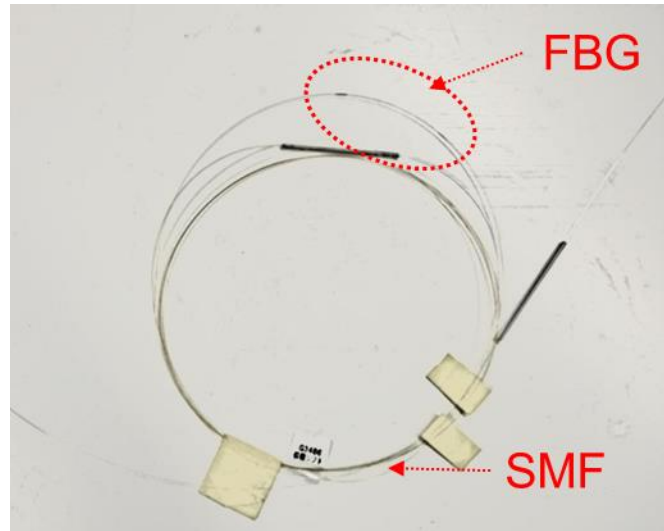
Figure 1.7. Photo of the FBG used in the following experiments.

There are three types of PS-FBGs used in the following experiment, manufactured by Fujikura Company. One of the PS-FBG is show in Figure 1.7. These PS-FBGs are written on SMFs. The fiber is coated by Polyimide for protection; thus the diameter of the fiber is 0.15 mm. The Bragg wavelengths of these PS-FBGs are about 1550 nm. All the PS-FBGs have reflectivity close to 100% near to the phase-shifted area. No chirp or apodize are used in the manufacture process of the PS-FBG. All the PS-FBGs can stand 1% strain for a second. Other parameters, such as the diameter of the core, diameter of the cladding, and index of the fiber, are confidential due to the rule of Fujikura Company. The difference between these three PS-FBGs is the depth of the index variation and length of the grating area, leading to the different shapes of the peak areas in the spectra. For convenient discussion and easy separation, the first group of PS-FBGs with broadest full-width half-maximum (FWHM) is called PS-FBG1, the one with medium FWHM is called PS-FBG2, and the one with narrowest FWHM is called PS-FBG3. The detail spectra will be shown in the following experiment.

There are many equipments used in our experiments. Table 1 shows the names, makers, models and abbreviations of some important equipments and softwares.

Table 1. Equipment and software: name, maker, model and abbreviation.

Name	Maker	Model	Abbreviation
Amplified Spontaneous Emission	FiberLabs	FL7050	ASE
External Cavity Tunable Laser Source	Agilent	81682A	TLS
Erbium Doped Fiber Amplifier	Fiberlabs	AMP-FL8013	EDFA
Photo-detector	Thorlabs	PDA10CS-EC	PD1
Photo-detector	Thorlabs	DET01CFC	PD2
Balanced Photo-detector	New Focus	2117	BPD
Optical Spectrum Analyzer	Anritsu	MS9710C	OSA
Electrical Spectrum Analyzer	Advantest	R3131A	ESA
Normal FBG	Fujikura		
Apodized FBG	Fujikura		AFBG
Oscilloscope	Yokogawa	DL708E	O-scope
Non-resonant PZT	Fuji Ceramics	1045S	N-PZT
Resonant PZT	Fuji Ceramics	M31	R-PZT
Macro Fiber Composite	Smart Material	M-2814-P2	MFC
Functional Generator	NF	WF1974	FG
High Speed Electrical Bipolar Amplifier	NF	HSA4012	E-Amp
Carbon Fiber Reinforced Plastic	Toray Industries	T700S/2500	CFRP
Preamplifier	PAC	1220A	Pre-Amp1
Preamplifier	NF	9917	Pre-Amp2
AE data acquisition system	PAC	DISP-80	AE-DAQ1
AE data acquisition system	NF	7661	AE-DAQ2
Material Testing Machine	Shimadzu	AG-50 kNG	MTM
Data Logger	Keyence	NR-ST04	
Strain Gage	Kyowa	2%-factor	
Microscope	Olympus	BH-2	
Disperse	ICL		
Opti-grating	Optiwave	4.2.2.54	
Matlab	Mathworks	R2007b	

2 PHASE SHIFTED FIBER BRAGG GRATING

2.1 Introduction of Phase Shifted Fiber Bragg Grating

Optical fiber grating has a periodic grating structure in the core of an optical fiber written by ultraviolet light, as shown in Figure 2.1(a) [39]. The optical fiber is usually SMF, and the diameters of the core, cladding and coating are normally about 10 μm, 125 μm and 150 μm, respectively. There are many different kinds of optical fiber grating, for example, long period grating, blazed grating, and FBG. Long period fiber grating has long period of index modulation, blazed grating has tilted shape of the index modulation, while FBG has short period and sinusoidal shape of index modulation as shown in Figure 2.1(b) [37, 39].

Due to this periodic structure, FBG reflects back a part of light in the certain range (near to the Bragg wavelength), while allows other light with different wavelengths pass through without loss. FBG is widely used in optical communication and optical sensing. However, when normal FBGs cannot satisfy some special functions, particular FBGs with complex structures are designed, such as apodized FBG (AFBG) for eliminating sidelobes, chirp FBG (CFBG) for broadening the FWHM, sampled FBG for generating a repeated spectrum. All of them have been found very important applications either in optical communication or optical sensing [37].
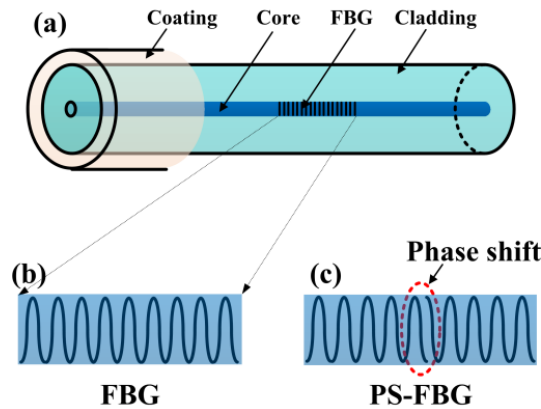
Figure 2.1. Structure of FBG and PS-FBG. (a) structure of FBG based on SMF; (b) periodic index modulation of the normal FBG; (c) a π phase shift in the middle of the grating for PS-FBG.

Among many different FBGs, PS-FBG is another important special FBG, which attracts our attentions. It is manufactured by inserting a π phase-shift in the middle of the grating area, as shown in Figure 2.1(c) [53, 54]. After the phase shift is made, two sections of the normal FBGs beside the phase shift area constitute as a Fabry-Perot structure. Therefore, the spectrum of PS-FBG changes: a very narrow peak will be shown in the middle of the reflected spectrum of FBG [55]. Due to this unique and

interesting structure, the PS-FBG has many applications. The most straightforward application of PS-FBG is used as an optical filter with narrow FWHM. Some researchers used it in optical communication for selecting a channel in wavelength division multiplexing (WDM) system [56]. Some researchers used it in distributed feedback laser establishment [36]. Furthermore, some researchers use it as a sensing element to measure the strain and temperature. Additionally, due to the narrow FWHM, the peak of the PS-FBG is easily separated when the polarization state of the grating area is influenced under the transverse strain [57]. Basically, the above researchers use the narrow FWHM property of the PS-FBG. The spectra properties of PS-FBG will be simulated in section 2.2.

In this study, we found another important characteristic of the PS-FBG in the field of ultrasonic detection. The Bragg wavelength shift of a normal FBG sensor has a linear relationship with the applied static strain [38]. However, when a normal FBG sensor is used for detecting high-frequency ultrasonic waves, the relationship between the Bragg wavelength shift and the strain caused by the ultrasonic wave becomes non-linear according to simulation and experimental results [58, 59]. In other words, there is a conflict between the sensitivity and bandwidth when a normal FBG sensor is used for ultrasonic detection because the effective grating length is inversely proportional to the slope of the spectrum. Therefore, a normal FBG sensor with a short grating length should be used to guarantee ultrasonic detectable bandwidths. As a result, normal FBG sensor needs time-consuming data averaging. However, in the case of PS-FBG, the π phase shift in the middle of the grating simultaneously decreases the effective grating length and enhances the slope [60, 61]. Thus, the sensitivity and detectable bandwidth in the PS-FBG are positive related. According to the experiments done by Rosenthal, the PS-FBGs are very suitable for ultrasonic detection. However, Rosenthal did not simulate the response of PS-FBG to ultrasonic wave. Thus, in section 2.3, we simulate the response of PS-FBG to longitudinal ultrasonic wave. Although, the actual ultrasonic wave which propagates in the CFRP laminate is Lamb wave with dispersion characteristic, our simulation still has reliability to reflect the physical phenomena clearly.

2.2   Simulation of Fiber Bragg Grating

Firstly, the spectra of FBG and PS-FBG are simulated and discussed.

Normally, Eq. 2.1 is used to describe the spatial index variation in the FBG:

$$n_{eff}(z) = n_{eff0} + \Delta n \left[1 + \cos\left(\frac{2\pi}{\Lambda} z + \phi(z) \right) \right] \qquad (2.1)$$

where n_{eff0} is the unperturbed effective refractive index, Δn is the maximum index change, Λ is the grating period, and $\phi(z)$ is grating chirp which we omitted because CFBG is not discussed in this dissertation.

Using the above equation and associate coupled-mode theory, the reflection property of FBG with a simple description can be obtained by direct-integration

approach. However, if we would like to simulate of some special FBGs, including AFBG, CFBG or PS-FBG, straightforwardly solving the coupled-mode equation is difficult because the index modulation changes along the SMF. Thus, researches always use transfer matrix method, which was proposed by Yamada and Sakuda [62], because of its high speed and high accuracy. According to this method, the whole FBG with length of L is divided into several small uniform sections [63]; therefore, every section can be treated as a uniform FBG, described by a matrix F_i. Every transfer matrix has format expressed in Eq. 2.2.

$$F_i = \begin{bmatrix} \cosh(\gamma_B \Delta z) - i\dfrac{\hat{\sigma}}{\gamma_B}\sinh(\gamma_B \Delta z) & -i\dfrac{\kappa}{\gamma_B}\sinh(\gamma_B \Delta z) \\ i\dfrac{\kappa}{\gamma_B}\sinh(\gamma_B \Delta z) & \cosh(\gamma_B \Delta z) + i\dfrac{\hat{\sigma}}{\gamma_B}\sinh(\gamma_B \Delta z) \end{bmatrix} \quad (2.2)$$

where Δz is the length of the i th uniform section, the "AC" coupling coefficient κ and the general "dc" self-coupling coefficient $\hat{\sigma}$ are the local values in the i th section, and $\gamma_B \equiv \sqrt{\kappa^2 - \hat{\sigma}^2}$. The detailed definitions of these parameters are shown in the references [37, 63].

In the AFBG, the index is different in every section because the index change has a Gaussian or raise cosine or other functional envelop. Eq. 2.3 describes the AFBG with Gaussian envelop.

$$n_{eff}(z) = n_{eff0} + \Delta n \cdot \sin^2\left(\frac{\pi}{\Lambda_0}z\right) \cdot \exp\left(-4\ln(2)\left(\frac{z-L/2}{L/3}\right)^2\right) \quad (2.3)$$

In the PS-FBG, there is a π phase shift matrix in the middle of grating, described by Eq. 2.4.

$$F_\pi = \begin{bmatrix} \exp(-i\pi) & 0 \\ 0 & \exp(i\pi) \end{bmatrix} \quad (2.4)$$

The whole transfer matrix of the FBG is obtained by multiplying all transfer matrixes in every section sequentially, as described in Eq. 2.5. Then, the reflectivity and transmittance of the FBG can be calculated by Eq. 2.6 and Eq. 2.7, respectively.

$$F = F_1 \cdot F_2 \cdot \ldots \cdot F_i \cdot \ldots \cdot F_m \quad (2.5)$$

$$R(\lambda) = \left|\frac{F_{21}(\lambda)}{F_{11}(\lambda)}\right|^2 \quad (2.6)$$

$$T(\lambda) = 1 - R(\lambda) \quad (2.7)$$

where $R(\lambda)$ is the reflectivity, and $T(\lambda)$ is the transmittance. By solving the above equations, the formula of spectra of FBG and PS-FBG are expressed in Eq. 2.8 and 2.9.

$$R(\lambda)_{FBG} = \left| \frac{-\kappa \sinh(\gamma_B L)}{\hat{\sigma} \sinh(\gamma_B L) + i\gamma_B \cosh(\gamma_B L)} \right|^2 = \frac{\sinh^2(\gamma_B L)}{\cosh^2(\gamma_B L) - \dfrac{\hat{\sigma}^2}{\kappa^2}} \quad (2.8)$$

$$R(\lambda)_{PS-FBG} = \left| \frac{2\kappa\hat{\sigma}\gamma_B \sinh^2(\gamma_B L)}{\kappa^2 - \hat{\sigma}^2 - i\hat{\sigma}\gamma_B \sinh(2\gamma_B L) - 2\hat{\sigma}^2 \sinh^2(\gamma_B L)} \right|^2$$

$$= \frac{2\hat{\sigma}}{\kappa \left[\left(\dfrac{\gamma_B}{\kappa \tanh(\gamma_B L/2)} - \dfrac{i\hat{\sigma}}{\kappa} \right)^2 - 1 \right]} \quad (2.9)$$

One important parameters in the spectra of FBG and PS-FBG is the Bragg wavelength. Although, the spectral equations of FBG and PS-FBG are different, the Bragg wavelength of both has the same and very simple expression, as shown in Eq. 2.10.

$$\lambda_B = 2n\Lambda \quad (2.10)$$

Figure 2.2 shows nine simulation results of FBG's spectra. In this simulation, n_{eff0} is 1.45, λ_B is 1550 nm, grating length L and index modulation Δn are changed depending on different conditions. Figure 2.2(a), (b) and (c) show the spectra of normal FBGs with different lengths and different index modulations. According to the simulation results, the FWHM of the spectra, the slope of the peak and the reflectivity are determined by the grating length and the index modulation. The FWHM increases with the decrement of grating length and increment of index modulation. The slope of the peak increases with the increment of grating length and index modulation. The reflectivity increases with the increment of grating length and index modulation. Figure 2.2(d) shows the spectrum of AFBG. While Gaussian function is used to modulate the index, we can see that the sidelobes which always exist in the normal FBG are depressed. However, it sacrifices the slope and reflectivity. Figure 2.2(e), (f) shows the PS-FBG with grating length of 5 mm, while with different index modulation. In the PS-FBG, due to the phase-shift in the middle of the grating, a narrow peak is generated, which is demonstrated by comparison of Figure 2.2(c) and (e), because they have the same parameters. We mainly focus on the peak area in the PS-FBG's spectrum. Four apparent characteristics of the peak area of the PS-FBG are shown in Figure 2.2(g), which shows the transmittance of the grating in Figure 2.2(e) with amplified X axis. Firstly, the peak is very narrow, which means it has limited dynamic range. Secondly, the slope of the peak is very steep, which means that it has very high sensitivity. Thirdly, beside the peak, there are relative flat ranges without sidelobes, which means that it is easy to be demodulated especially in the power detection method. Fourthly, the slope of the peak area of PS-FBG has better linear trend compared to normal FBG. Compared with Figure 2.2(e) and (f), or compared with Figure 2.2(h) and (i) which show the transmittance of the grating in Figure 2.2(e) and (f) via logarithmic scale. We also demonstrate that the peak area of PS-FBG is also determined by the grating length and the index modulation as normal FBG. For

example, by increasing the index modulation, the FWHM of the peak becomes narrower and the slope of the peak becomes steeper.
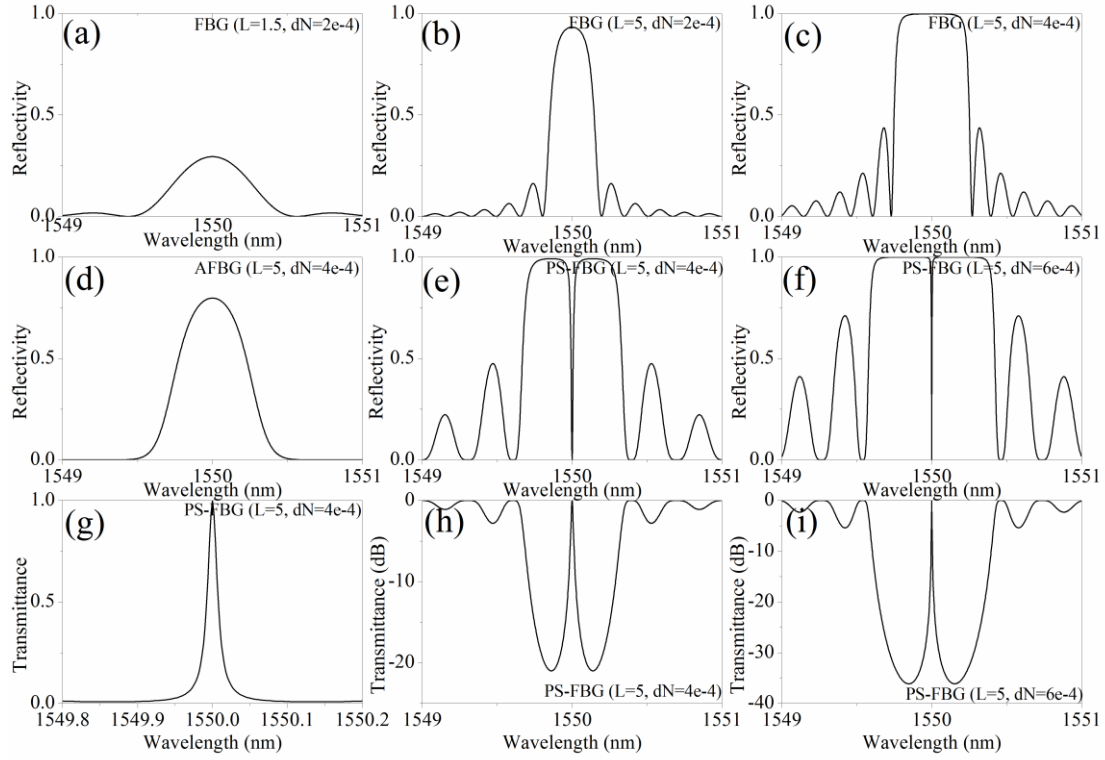
Figure 2.2. FBG spectral simulation. L is the grating length, dN is the index modulation.

The grating shown in Figure 2.2(a) can correspond to the normal FBG used in our lab's previous system [44], which will be also used as the reference in the following experiment. The grating shown in Figure 2.2(e) and (f) can correspond to the PS-FBG1 and PS-FBG2 used in our experiment. The exact spectra are of course different to the ones in this simulation because of the process error or other influences. The exact spectra of the actual PS-FBGs are always broader than the simulated ones, and the spectra are always not symmetric. However, this simulation and the simulation in the following section will have certain ability to reflect the physical principle of the PS-FBG. Thus, in section 2.3, we compare the different responses of FBG (Figure 2.2(b)), PS-FBG1 (Figure 2.2(e)) and PS-FBG2 (Figure 2.2(f)) to longitudinal ultrasonic waves.

2.3 Simulation of PS-FBG's Response to Ultrasonic Wave

2.3.1 *Index modulation changed by ultrasonic wave*

In the ultrasonic SHM, the ultrasonic wave propagates in a plate is Lamb wave with dispersion characteristics, leading to the difficulty of simulation. Therefore, for simplifying the analysis of the responses of the FBGs to ultrasonic wave, herein, we

assume the strain caused by longitudinal ultrasonic wave has a sinusoidal form, expressed by Eq. 2.11:

$$\varepsilon(t) = \varepsilon_m \cos\left(\frac{2\pi}{\lambda_S} z - \omega_S t\right) \tag{2.11}$$

where ε_m is the ultrasonic displacement amplitude, λ_S is the wavelength of the ultrasonic wave, and ω_S is its angular frequency.

Under the influence of the ultrasonic wave, the FBG will be impacted from two aspects [58]. First, because of the Geometric effect, the mechanical contribution induces a deformation along the z axis of the grating. Thus, the position z is translated into the point z', expressed as Eq. 2.12 [58].

$$z' = f(z,t) = z + \varepsilon_m \frac{\lambda_S}{2\pi} \sin\left(\frac{2\pi}{\lambda_S} z - \omega_S t\right)$$
$$+ \varepsilon_m \frac{\lambda_S}{2\pi} \sin(\omega_S t), z \in [0,L] \tag{2.12}$$

The second influence is the elasto-optic effect, which changes the index. This phenomenon, making the FBG not uniform any more, can be expressed as Eq. 2.13:

$$\Delta n'(z',t) = -\left(\frac{n_{eff0}^3}{2}\right) \cdot \left[P_{12} - \upsilon(P_{11} + P_{12})\right]$$
$$\cdot \varepsilon_m \cos\left(\frac{2\pi}{\lambda_S} z' - \omega_S t\right) \tag{2.13}$$

where P_{ij} are the stress-optic coefficients and υ is the Poisson's ratio. Therefore, the Bragg effective refractive index modulation under the ultrasonic wave action can be rewritten as Eq. 2.14:

$$n'_{eff}(z',t) = n_{eff0} - \Delta n\left(1 + \upsilon \cos\left(\frac{2\pi}{\Lambda_0} f^{-1}(z',t)\right)\right)$$
$$- \left(\frac{n_{eff0}^3}{2}\right)\left[P_{12} - \upsilon(P_{11} + P_{12})\right] \cdot \varepsilon_m \cos\left(\frac{2\pi}{\lambda_S} z' - \omega_S t\right) \tag{2.14}$$

Eq. 2.14 is hard to deal with because z is not uniform any more caused by geometric effect. However, from other aspect, the geometric effect makes the grating period extending or compressing, while the length in every section keeps uniform. Based on this idea, the function can be rewritten as Eq. 2.15 and 2.16:

$$n'_{eff}(z',t) = n_{eff0} - \Delta n\left(1 + \upsilon \cos\left(\frac{2\pi}{\Lambda'_0} z'\right)\right)$$
$$- \left(\frac{n_{eff0}^3}{2}\right)\left[P_{12} - \upsilon(P_{11} + P_{12})\right] \cdot \varepsilon_m \cos\left(\frac{2\pi}{\lambda_S} z' - \omega_S t\right) \tag{2.15}$$

$$\frac{\Lambda_0}{\Lambda_0^{'}} = \frac{z}{z^{'}} \qquad (2.16)$$

According to Eq. 2.15 and Eq. 2.16, and related to transfer matrix method, the spectra of FBGs under the influence of longitudinal ultrasonic wave can be solved. Herein, we further consider one condition when the wavelength of ultrasonic wave is much longer than the grating length, i.e., $\lambda_S \gg L$. This condition is approximate to the static condition, because the grating suffer almost the same index modulation when $\lambda_S \gg L$. In this case, the Eq. 2.15 can be rewritten as Eq. 2.17.

$$
\begin{aligned}
n_{eff}^{'}\left(z^{'},t\right) = n_{eff\,0} &- \Delta n \sin^2\left(\frac{\pi}{\Lambda_0\left[1+\varepsilon_m \cos\left(\omega_S t\right)\right]}z^{'}\right) \\
&- \left(\frac{n_{eff\,0}^3}{2}\right)\cdot\left[P_{12}-\upsilon\left(P_{11}+P_{12}\right)\right]\cdot\varepsilon_m \cos\left(\omega_S t\right)
\end{aligned}
\qquad (2.17)
$$

By solving Eq. 2.17, the expression of the Bragg wavelength shift of the FBGs under the influence of ultrasonic wave when $\lambda_S \gg L$ is shown in Eq. 2.18, which is the same as the Bragg wavelength shift of FBGs in static conditions [38].

$$\Delta\lambda_0 = \lambda_B \varepsilon_m\left(1-\left(\frac{n_{eff\,0}^3}{2}\right)\left[P_{12}-\upsilon\left(P_{11}+P_{12}\right)\right]\right) \qquad (2.18)$$

For convenient discussion later, we define the parameter of effective Bragg wavelength, as the ratio of the maximum Bragg wavelength when it is in dynamic ultrasonic strain and in static strain, as shown in Eq. 2.19. Furthermore, we define the ratio of the grating length and the wavelength of the longitudinal ultrasonic wave in Eq. 2.20.

$$\Delta\lambda_{eff} = \frac{\max\left(\Delta\lambda\right)\big|_{dynamic}}{\max\left(\Delta\lambda\right)\big|_{static}} \qquad (2.19)$$

$$\text{ratio} = \frac{\lambda_S}{L} \qquad (2.20)$$

In order to analysis the response of FBG, PS-FBG1 and PS-FBG2 to longitudinal ultrasonic wave with different ultrasonic wavelength in different strains. Table 2 illustrates the parameters used in this simulation.

16

Table 2. Parameters used in this simulation.

$n_{eff\,0}$	1.45
λ_B	1550 nm
P_{11}	0.12
P_{12}	0.275
υ	0.17

2.3.2   *Bragg wavelength shifts by ultrasonic wave*

Figure 2.3, Figure 2.4 and Figure 2.5 show the Bragg wavelength shift of different FBGs under the influence of ultrasonic wave with different ratio of the grating length and ultrasonic wavelength when the strain is 10 με. All the sensors have responses to ultrasonic waves, shown sinusoidal format as the simulated longitudinal ultrasonic wave. When the ultrasonic wavelength is 10 times longer than the grating length (red lines), the Bragg wavelength shifts of all the FBGs are very close. After we calculated, those Bragg wavelength shifts in this case are close to those when the FBGs are in static strain. However, the phenomenon changes when the ultrasonic wavelength is equivalent to the grating length (blue lines). In this case, although there are Bragg wavelength shift to all the FBGs, the values of Bragg wavelength shift are different to each. The normal FBG has the minimum Bragg wavelength shift, while the PS-FBG2 has the maximum Bragg wavelength shift. It simply demonstrates the different responses of different FBGs to ultrasonic wave.
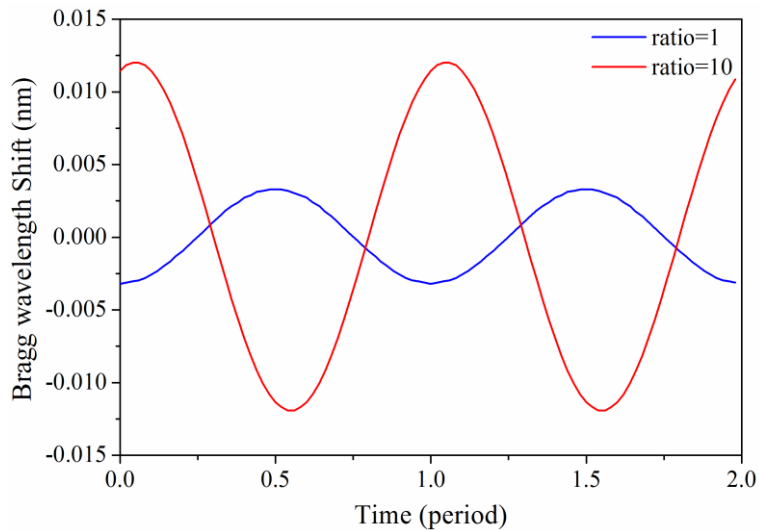
Figure 2.3. Bragg wavelength shift of normal FBG under the influence of ultrasonic wave with different ratio of grating length and ultrasonic wavelength.
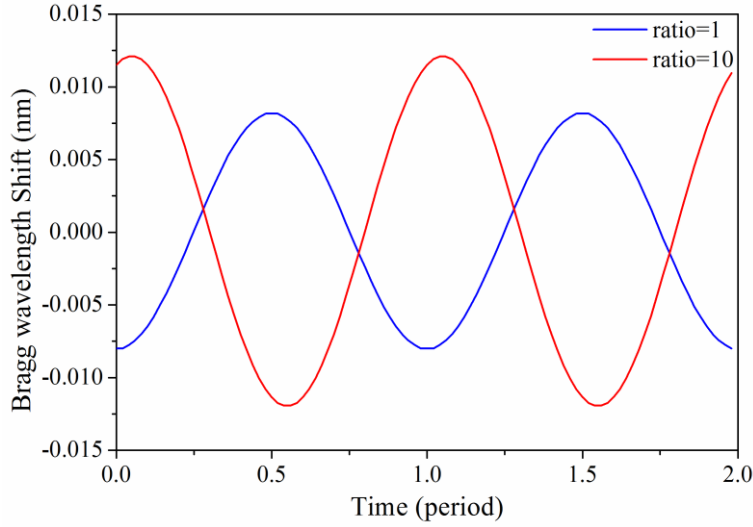
Figure 2.4. Bragg wavelength shift of PS-FBG1 under the influence of ultrasonic
wave with different ratio of grating length and ultrasonic wavelength.
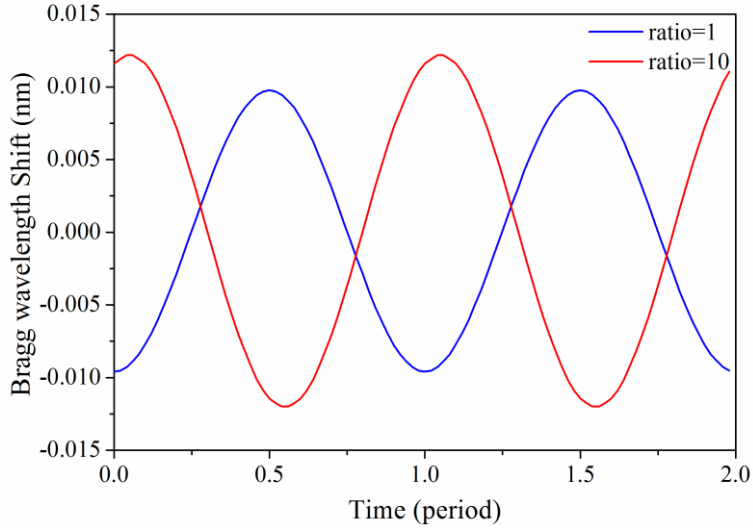
Figure 2.5. Bragg wavelength shift of PS-FBG2 under the influence of ultrasonic
wave with different ratio of grating length and ultrasonic wavelength.

2.3.3 *Effective Bragg wavelength shift*

Based on the same method, we describe the effective Bragg wavelength shift $\Delta\lambda_{eff}$ of FBGs to the different ratio with different applied strains, as shown in Figure 2.6. Firstly, the different applied strains do not have effects to the effective Bragg wavelength shifts because the solid marks (10 με) almost match the corresponding open marks (100 με). Then, the curves can be divided into two parts. The first part is when the ratio of grating length and ultrasonic wavelength is larger than 10, i.e., the ultrasonic wavelength is longer than 50 mm when the grating length is 5 mm. In this part, all the FBGs have almost the same effective Bragg wavelength shift of 1. It means the strain from ultrasonic wave affects the FBG and PS-FBG as the same behavior as static strain.

However, when the ratio decreases (ultrasonic wavelength decreases) from 10, all the effective Bragg wavelength shifts of FBGs decrease. The curves in normal FBG decrease most rapidly, while the curves in PS-FBG2 decrease relative gentle. For example, when the ratio of grating and ultrasonic wavelength is 1, the effective Bragg wavelength shifts to FBG, PS-FBG1 and PS-FBG2 are 0.27, 0.66 and 0.79, respectively. In general, this phenomenon shows the PS-FBG has better response characteristics than FBG. It can be explained as the effective grating length. Because the structure of PS-FBG is resemble to the structure of Fabry-Perot structure, light is concentrated in the phase shifted area rather than uniformly distributed along the grating as the normal FBG. When the ultrasonic wave impacts on the FBG, the phase-shifted area gets more severe influence, i.e., the PS-FBG obtains all the influence from ultrasonic wave in relative short length. In other words, the effective grating length of PS-FBG is shorter than that of normal FBG. Furthermore, the index modulation helps to enhance this phenomenon. For example, the PS-FBG2 with higher index modulation has larger effective Bragg wavelength shift compared to the case of PS-FBG1. This can also be explained by the resemble structure of Fabry-Perot. When PS-FBG has higher index modulation, the two parts of normal FBG beside the phase shift area has higher reflectivity, leading to more parts of light concentrated in the phase shift area. Therefore, the higher index modulation in the PS-FBG reduces the effective length of PS-FBG. We also simulated the FBG with higher index modulation, as the FBG shown in Figure 2.2(c). However, according to our results, the index modulation in normal FBG does not help to increase the performance of effective Bragg wavelength shift.

The speed of ultrasonic wave is assumed to be 5 km/s, which is reasonable because it is approximate to the value in metal. Due to the inverse relation between frequency and wavelength, Figure 2.6 also can be seen from the frequency aspect, e.g., 5-mm ultrasonic wavelength corresponds to 1 MHz. If the bandwidth of the FBGs to ultrasonic wave defines as the effective Bragg wavelength shift decreases to 50% (3-dB) compared to the maximum value, the bandwidth of FBG, PS-FBG1 and PS-FBG2 are 0.71 MHz, 1.35 MHz and 1.92 MHz, respectively. According to this proximate evaluation, the bandwidth of PS-FBG1 is about 1.9 times broader than that of normal FBG, and the bandwidth of PS-FBG2 is about 2.7 times broader than that of normal FBG. Until now, we have demonstrated the broad bandwidth property of PS-FBG.
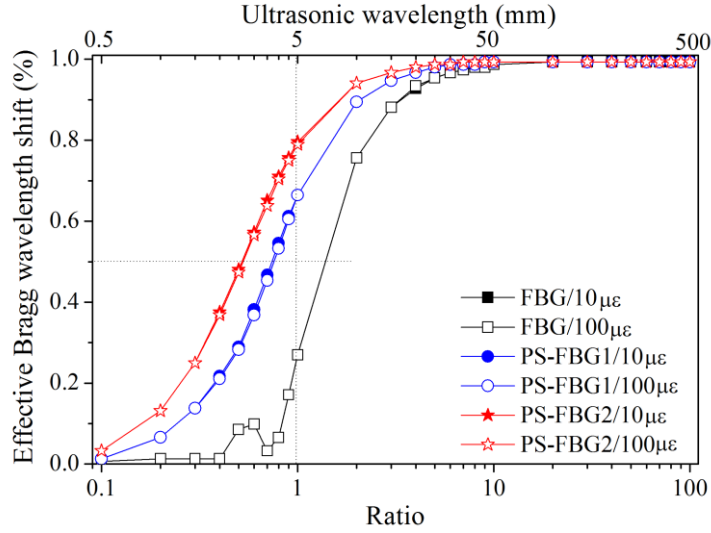
Figure 2.6. Effective Bragg wavelength shift of FBGs (FBG, PS-FBG1, PS-FBG2) to the different ratio of grating length and ultrasonic wavelength with different applied strains.

2.3.4 *Spectrum deformations*

In order to analysis the performance of PS-FBG deeper, further simulations are conducted. Figure 2.7, Figure 2.8 and Figure 2.9 show the spectra change of FBGs with different ratio of grating length and ultrasonic wavelength when the applied strain is 100 με. When the ratio is 10 in the case of FBG, the spectrum shifts but maintains almost the initial shape. This can be explained by the long ultrasonic wavelength as a quasi-static strain. When the ratio is 0.1, the spectrum shape is also similar as the initial one, but the Bragg wavelength shift is very small. Because when the ultrasonic wavelength is very small, the effects from the ultrasonic strain are evened along the FBG, leading to alleviation of the ultrasonic effect. However, when the ratio is 1, although the Bragg wavelength shifts, the value is small, as explained previously. Furthermore, the spectrum changes largely, e.g., the right sidelobes increase. However, the phenomena are different in the case of PS-FBG according to Figure 2.8 and Figure 2.9. The Bragg wavelength shift is discussed before. The peak area caused by the phase shift almost maintains its initial shape. This is another advantage in PS-FBG, because it decreases the errors in demodulation systems. Especially to the power detection demodulation method, absence of the sidelobes and the maintaining of the peak area shape make the waveforms analysis easier and more accurate. Furthermore, through comparison between Figure 2.8 and Figure 2.9, the larger index modulation also helps to enhance the performance of shape maintaining in the peak area.
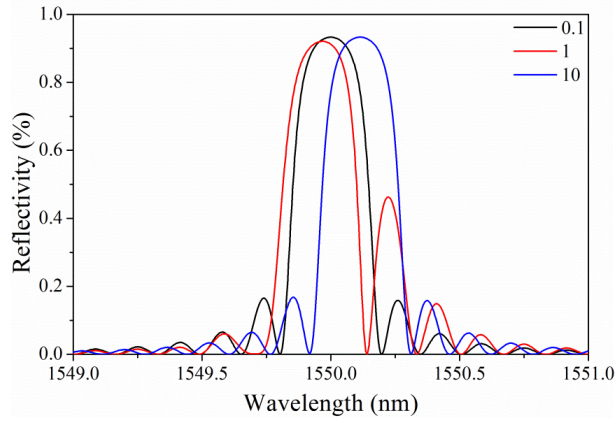
Figure 2.7. Spectrum change of FBG with different ratio of grating length and ultrasonic wavelength when the applied strain is 100 με.
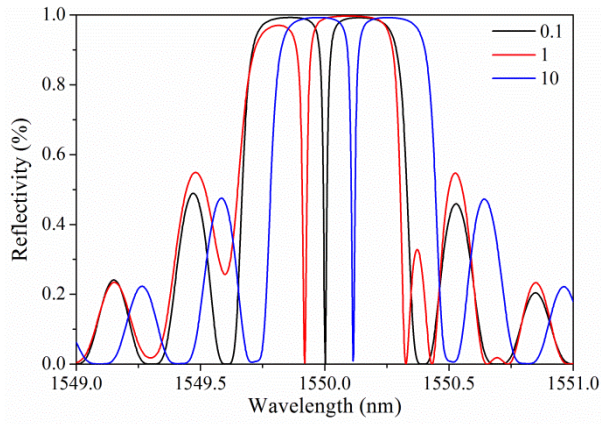
Figure 2.8. Spectrum change of PS-FBG1 with different ratio of grating length and ultrasonic wavelength when the applied strain is 100 με.
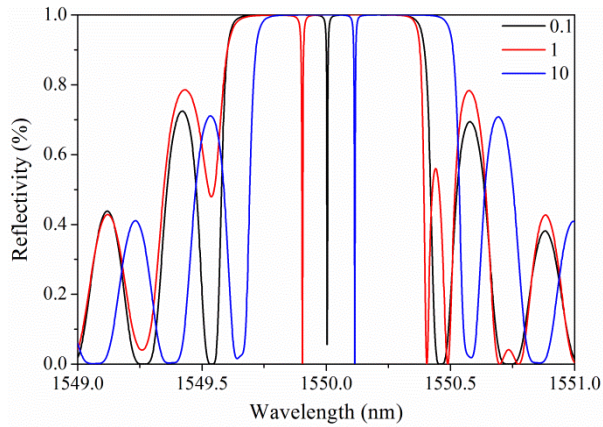
Figure 2.9. Spectrum change of PS-FBG2 with different ratio of grating length and ultrasonic wavelength when the applied strain is 100 με.
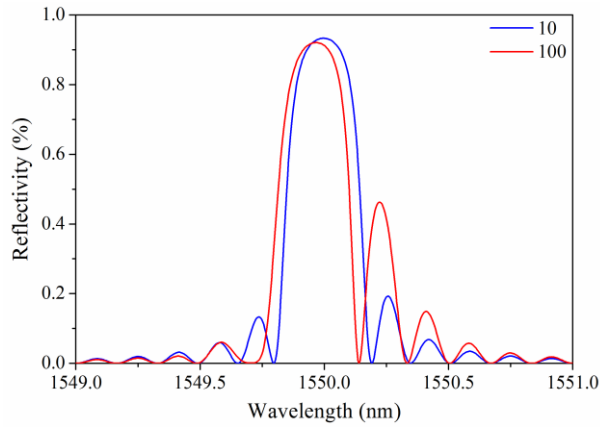
Figure 2.10. Spectrum change of FBG under different applied strains when the ratio of grating length and ultrasonic wavelength is 1.
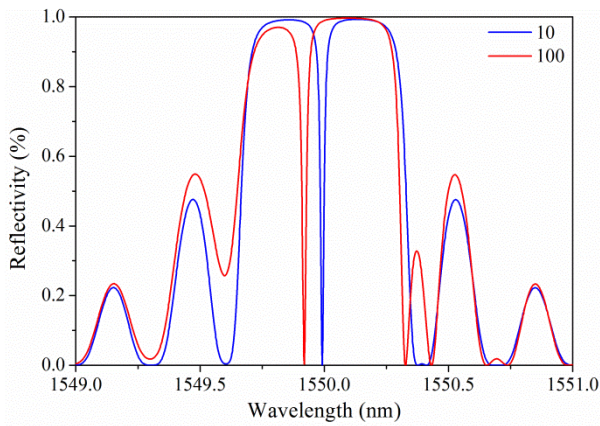
Figure 2.11. Spectrum change of PS-FBG1 under different applied strains when the ratio of grating length and ultrasonic wavelength is 1.
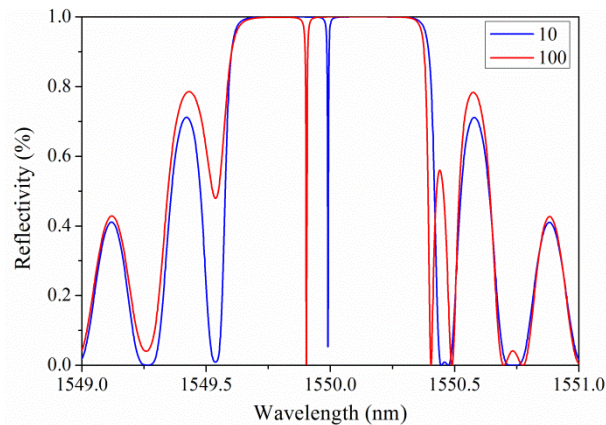
Figure 2.12. Spectrum change of PS-FBG2 under different applied strains when the ratio of grating length and ultrasonic wavelength is 1.

Furthermore, we analysis the spectrum change of FBGs under different applied strains, when the ratio of grating length and ultrasonic wavelength is 1. It can be seen that the larger strain changes the spectrum of FBG larger besides the Bragg

wavelength shift. However, the larger strain only shifts the Bragg wavelength, but without or with very small influence on the shape of the peak area.

2.3.5 *Output voltage vibration by ultrasonic wave*

The above discussions are based on the analysis of Bragg wavelength shift. However, in actually practical cases, the influence from demodulation system should be considered. We assume the edge filter demodulation is used. Thus, the reflectivity in the 3-dB position of the certain spectrum changes under the influence of ultrasonic wave, leading to the output voltage vibration. Because the strain caused by the ultrasonic wave is usually small, here we consider the case when the strain is 10 με. Figure 2.13 shows the simulation results. The voltage change in the FBG is very small, while the voltage change in the PS-FBG2 is large. The different effective Bragg wavelength shifts and different slopes in the FBG and PS-FBG caused this large difference together. However, in the curve of PS-FBG2, deformation is observed, marked by black dot circles. Because the FWHM of the PS-FBG2 is very small, even the Bragg wavelength shift caused by 1-με strain still will be out its dynamic range. Thus, when PS-FBG is used to detect large signals, such as impact, additional attention should be paid. However, the applied strain generated by PZT or other actuator is very small in some cases of ultrasonic detections, the deformation will be not a problem, as shown in the dot blue curve in Figure 2.13 obtained when the strain is 1 με. According to Figure 2.13, we can evaluate the signal amplitude of different FBGs. The signal amplitude in the FBG, PS-FBG1 and PS-FBG2 are 0.005, 0.053 and 0.327. Thus, when edge filter demodulation technique is used, the approximate evaluated sensitivity of PS-FBG2 is 6-time higher than that of PS-FBG1 and 60-times higher than that of FBG. These differences are contributed from two aspects: one is the broader ultrasonic bandwidth of PS-FBG, the other is the steeper slope in the PS-FBG.
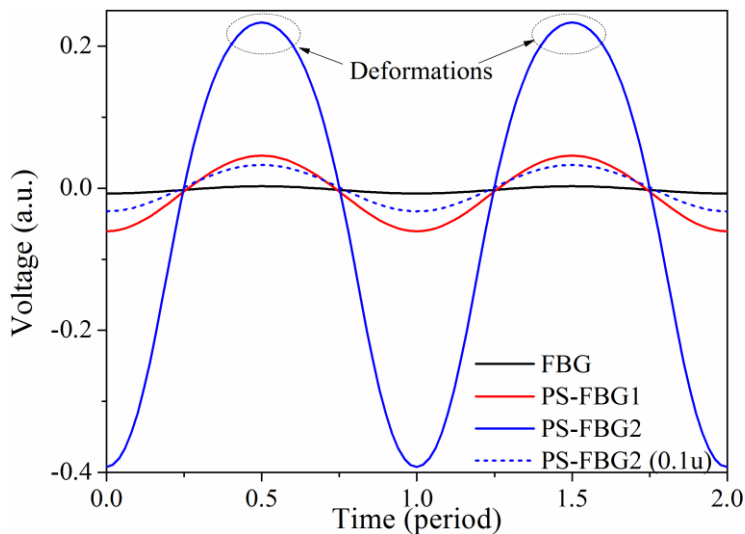
Figure 2.13. Output voltage vibrations of different FBGs under the influence of ultrasonic wave when the ratio is 1.

According to the simulation results, we demonstrated the broad bandwidth and high sensitivity properties of PS-FBG. These simulation results show that the PS-FBG enhances the performance of OFS in ultrasonic detection.

2.4 Sensitivity Distribution Properties of PS-FBG

According to above simulation and analysis, the PS-FBG has many advantages compared to normal FBG in the application of ultrasonic SHM. Before application of PS-FBG to ultrasonic detection, several properties of PS-FBG should be clarified, for example the sensitivity distribution properties.

The sensitivity distribution properties of FBG to ultrasonic wave have been studied by Rosenthal *et al*., when it is used as hydrophone [64]. However, when it is used in the field of ultrasonic SHM, the sensitivity distribution properties have not been studied deeply before.

In many our following experiments (such as the experiments in Chapter 3-5), the PS-FBG sensor was glued in line to the ultrasonic source. This configuration is similar to other experimental configurations where normal FBGs were used [21, 44, 65]. However, a network with many FBG or PS-FBG sensors is necessary in both the acousto-ultrasonic detection and the AE detection. Thus, to understand the sensitivity distribution properties of FBG or PS-FBG, it is important to optimize the sensor network for SHM and NDT. Furthermore, signal analysis to determine the damage types or identify the impact position or AE positions also demands systematic study in this field. Thus, studying the sensitivity distribution properties of PS-FBG is very important.

Although, compared to normal FBG, PS-FBG has broader bandwidth and higher sensitivity to an ultrasonic wave, the theory of ultrasonic detection for PS-FBG is identical because, under the influence of an ultrasonic wave, PS-FBG undergoes the same physical changes as optical fiber. Once we obtained the sensitivity distribution properties of PS-FBG, we could also deduce these results for normal fiber sensors in more common cases. The sensitivity distribution properties of an optical fiber sensor are mainly determined by the distance from and the angle to the ultrasonic source, but the distribution is also influenced by many other factors, such as effective sensing length and cladding property. Furthermore, when the fiber is attached to the surface of a material, additional factors should be considered, including coupling performance, the ultrasonic wave's properties, and the material's geometric structure. Thus, in this part, we comprehensively researched the sensitivity distribution properties of PS-FBG when the sensor was attached to the surface of an aluminum plate [66].

2.4.1 *Experimental setup*

Figure 2.14 is a schematic diagram of the experimental setup based on the acousto-ultrasonic detection. A PS-FBG was used as an ultrasonic sensor. Using cyanoacrylate adhesive, the PS-FBG was glued to an aluminum plate with dimensions of 50×50×0.3

(L×W×H) cm^3. The size of the plate was large enough that the waveform had only one envelop in the detection time interval of 80 µs because reflected waves do not exist in this time interval.

The Bragg wavelength shift caused by the strain from the ultrasonic wave was demodulated by the balanced sensing technique, which will be described in chapter 4. This technique has a very low noise level, and the output electrical voltage is linearly proportional to the Bragg wavelength shift. Therefore, this technique can describe the Bragg wavelength shift correctly and precisely.
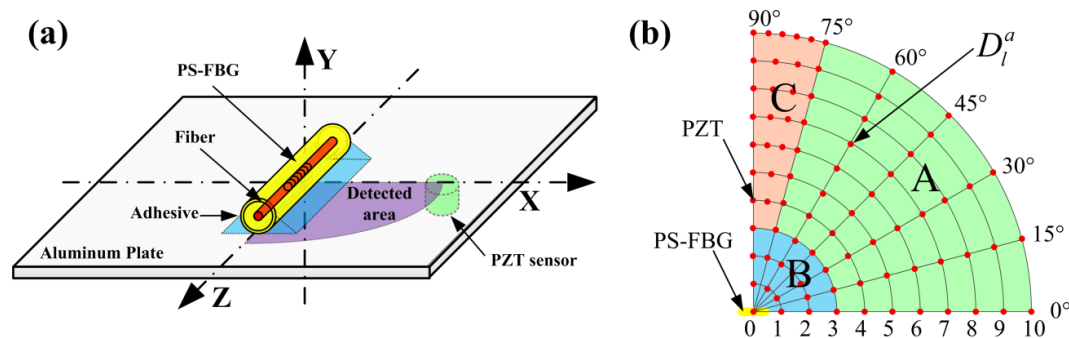
Figure 2.14. Schematic diagram of experimental setup. (a) Acousto-ultrasonic detection was used to research the sensitivity distribution properties of a PS-FBG sensor on an aluminum plate. (b) Data were measured on 82 different dots distributed in a quarter-circle range.

Serving as a point-like ultrasonic source, the N-PZT ultrasonic actuator with a diameter of 3 mm was driven by an electrical pulse with a peak-to-peak voltage of 75 V. The input signal was a one-cycle sinusoidal wave at 400 kHz with a Hamming window, and thus the corresponding frequency range reached approximately 1 MHz to simulate AE signals with broad bandwidth.

Using a high-acoustic-impedance ultrasonic couplant, the PZT actuator was glued to 82 different excitation dots on the aluminum plate's bottom surface. These dots were distributed from 0 to 10 cm and from 0 to 90 degrees in a quarter-circle range, as shown in Figure 2.14(b). To ensure careful observation of the waveform's change, the distribution of the dots from 75 to 90 degrees was denser than the distribution in other areas. Because the amplitudes of detected waveforms were greatly affected by the attachment condition, data were collected by repeating the measurement three times to guarantee the reliability of the experimental results.

For convenient discussion, three naming rules were introduced. Firstly, a Cartesian coordinate system was established on the plate in which the phase-shifted area of the PS-FBG was set as the origin and the axial direction of the fiber was set as the Z-axis, as shown in Figure 2.14(a). Then, the excitation dots were designated D_l^a. The superscript a and the subscript l denote the angle and length between the actuator and the sensor, respectively. Finally, because of different observational phenomena present in this experiment, the excitation area can be roughly divided into three parts, marked as A, B, and C, as shown in Figure 2.14(b).

2.4.2 *Theoretical analysis*

Bragg wavelength shift by strains in three orthogonal axes

Firstly, we consider an ideal case; i.e., the fiber is in a free space. When the optical fiber with the grating area is affected by strain generated by an ultrasonic wave, the n (the average refractive index) and Λ (the average grating period) change according to Eq. 2.17 and 2.18, respectively [67],

$$n = n_0 - \frac{n_0^3}{2}\left[P_{12}\varepsilon_z + \left(P_{11} + P_{12}\right)\frac{\varepsilon_x + \varepsilon_y}{2} \right] \tag{2.17}$$

$$\Lambda = \left(1 + \varepsilon_z\right)\Lambda_0 \tag{2.18}$$

where n_0 is the initial average refractive index, Λ_0 is the initial average grating period, P_{11} and P_{12} are Pockel's strain-optic coefficients, and ε_x, ε_y, and ε_z are the strains along the three orthogonal axes X, Y, and Z, respectively.
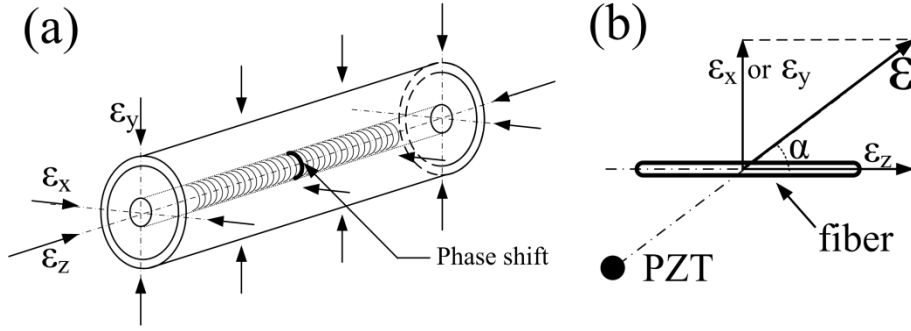
Figure 2.15. Theoretical principle. (a) PS-FBG subjected to strains in three orthogonal axes. (b) Directional strain impacts on an optical fiber.

Herein, we consider two different conditions. In the first case, the ultrasonic wave only propagates along the Z-axis. Because the fiber approximates isotropic material, the lateral strains are related to the axial strain by a standard Poisson ratio ν. Thus, in this case, the strains in the three axes have the relations expressed in Eq. 2.19.

$$\varepsilon_x = \varepsilon_y = -\nu\varepsilon_z \tag{2.19}$$

By substituting Eq. 2.19 into Eq. 2.10, 2.17, and 2.18, the Bragg wavelength shift $\Delta\lambda_B$ is expressed in Eq. 2.20.

$$\Delta\lambda_B = C_z\lambda_B\varepsilon_z$$
$$C_z = 1 - \frac{n_0^2}{2}\left[P_{12} - \nu\left(P_{11} + P_{12}\right) \right] \tag{2.20}$$

Alternately, when the fiber only experiences lateral strain along the X-axis or Y-axis, the stains in the three orthogonal axes have the relations shown in Eq. 2.21.

These relations are because the cylindrical fiber is rotationally symmetric in the X- and Y-axes, and the fiber material is isotropic.

$$-v\varepsilon_x = \varepsilon_y = \varepsilon_z \text{ or } \varepsilon_x = -v\varepsilon_y = \varepsilon_z \quad (2.21)$$

By substituting Eq. 2.21 into Eq. 2.10, 2.17, and 2.18, the Bragg wavelength shift $\Delta\lambda_B$ is expressed in Eq. 2.22,

$$\Delta\lambda_B = C_i \lambda_B \varepsilon_i$$
$$C_i = -v - \frac{n_0^2}{2}\left[-vP_{12} + \frac{1-v}{2}(P_{11} + P_{12})\right] \quad (2.22)$$

where $i = x$ or y. In a standard single-mode fiber, n_0, v, P_{11}, and P_{12} have values of about 1.4453, 0.17, 0.121, and 0.27, respectively. Thus, $C_x = C_y = $-0.29150, and $C_z = 0.7874$.

In the first case, the Bragg wavelength shift is proportional to the stain in the Z-axis, according to Eq. 2.20, and in the second case, the shift is proportional to the strain in the X- or Y-axis, according to Eq. 2.22. The absolute value of C_z is larger than the absolute value of C_x or C_y. However, the negative sign in C_x and C_y means that the same strain will cause the Bragg wavelength to shift in the opposite direction, reflected as an opposite initial phase in detected waveforms.

Influence from surface attachment method

The above analysis is based on the assumption that the ultrasonic wave perfectively couples to the optical fiber. However, in both our experimental condition and other practical conditions where the fiber is attached to the surface of a plate, the effective ultrasonic coupling performance between fiber and plate should be considered. The strain from the Z-axis has the best coupling performance, while the strain from the X-axis is difficult to couple to the fiber due to the limited effective contact area. Although no strain exists from the Y-axis because of the fiber's surface attachment method, acceleration in the Y-axis will cause dynamic strain to influence the fiber. Thus, in the actual case, the parameters C_x, C_y, and C_z will deteriorate to c_x, c_y, and c_z, the absolute values of which have relations $|c_z| > |c_x|$ and $|c_z| > |c_y|$. The exact actual values differ depending largely on coupling performance; however, the negative sign in c_x and c_y will always exist.

Bragg wavelength shift by directional strain

A more common case in which the ultrasonic wave propagates from a direction other than the three orthogonal axes is considered. When the PZT actuator and the PS-FBG sensor have an angle of α, as shown in Figure 2.15(b), the actual strain applied to the fiber can be written as the composite of the strains from the Z-axis and the strain from

the X- or Y-axis. For example, when the stain is in the X-Z plane, the Bragg wavelength shift under strain ε can be written as:

$$\Delta\lambda_B = c_x\lambda_B\varepsilon_x + c_z\lambda_B\varepsilon_z = (c_x\sin\alpha + c_z\cos\alpha)\lambda_B\varepsilon \qquad (2.23)$$

Due to the negative sign in c_x, there should exist an angle α_{min} where the Bragg wavelength shift is minimal. Because the Bragg wavelength shift is proportional to the output voltage, α_{min} can be predicted according to Eq. 2.24, where $V|\varepsilon_z$ and $V|\varepsilon_x$ are the amplitudes of the detected waveforms measured when the stain exists only in the Z-axis and the X-axis, respectively.

$$\alpha_{min} = \tan^{-1}\left(-\frac{c_z}{c_x}\right) = \tan^{-1}\left(-\frac{\Delta\lambda_B|_{\varepsilon_x=0}}{\Delta\lambda_B|_{\varepsilon_z=0}}\right) = \tan^{-1}\left(-\frac{V|\varepsilon_z}{V|\varepsilon_x}\right) \quad (2.24)$$

Frequency responses to different angles

As demonstrated in our previous research, the fiber's frequency response to ultrasonic waves depends on the effective sensing length. In general, as the effective sensing length lengthens, the high-frequency response worsens. When an ultrasonic wave propagates along the Z-axis, the effective sensing length of PS-FBG is the effective grating length with about a few hundred micrometers [61]. When an ultrasonic wave propagates along the X- or Y-axis, the effective sensing length is the fiber's 150-micrometer diameter, which is shorter than the effective grating length. Thus, without considering the influence from distance or the surface attachment method, the PS-FBG sensor will have a higher response to the ultrasonic wave that propagates in the X- or Y-axis. Furthermore, considering the actual case, the sensitivity decrement of PS-FBG to high frequencies is slower than the decrement to low frequencies when the angle between sensor and actuator changes from 0 degrees to 90 degrees. Paralleling this effect, the detected signal cannot be completely removed at α_{min} because the exact α_{min} differs depending on frequency.

2.4.3   *Sensitivity distribution on an aluminum plate*

Because the noise level, determined by the demodulation system, was constant in this experiment, the amplitudes of the detected waveforms can be used to directly evaluate the sensitivity of PS-FBG. A Hilbert transform was used to obtain the envelopes of the detected waveforms [68], and the amplitudes were then obtained by averaging the thrice-measured data. Figure 2.16 shows the sensitivity distribution properties of the PS-FBG on an aluminum plate in logarithmic scale. According to Figure 2.16, the detected waves' amplitudes decrease with the increase in distance between the PS-FBG sensor and the ultrasonic source. However, when the distance is smaller than 4 cm, the amplitudes are relatively large. Figure 2.17 was obtained by normalizing the amplitudes at 4 cm for different angles. In Figure 2.17, there is a clear corner at 4 cm. After 4 cm, the slopes of all curves are similar, due to attenuation of the ultrasonic

wave. However, before 4 cm, the curves' slopes change greatly, especially in data from large angles, such as 75 and 90 degrees. When the distance between sensor and actuator is small (corresponding to area B), the dynamic strain from the Y-axis caused by acceleration is relatively large and effectively shifts the Bragg wavelength, which leads to relatively large amplitudes.
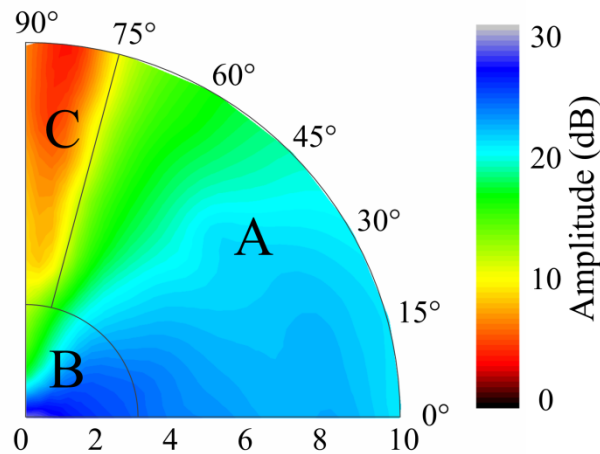
Figure 2.16. Sensitivity distribution properties of PS-FBG on an aluminum plate shown in logarithmic scale.
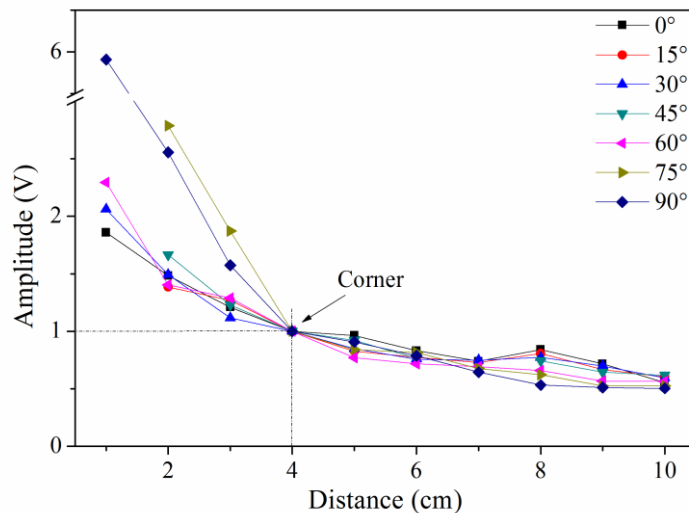
Figure 2.17. Amplitudes of detected waveforms at different distances for different angles after normalizing the detected waveforms' amplitudes to 4 cm.

According to Figure 2.16, unlike a traditional PZT sensor (which is omnidirectionally sensitive), the sensitivity of the PS-FBG has an obvious directional dependence. Extracting the amplitudes at every distance in Figure 2.16, the sensitivity distribution at different angles is shown in Figure 2.18. As this figure depicts, the amplitudes generally decrease with the angle's increment. However, odd phenomena are observed from 75 to 90 degrees after 4 cm, as amplified in the inset of Figure

2.18. These phenomena result because the smallest amplitude is located around 84 degrees rather than 90 degrees, corresponding to area C in Figure 2.14(b).
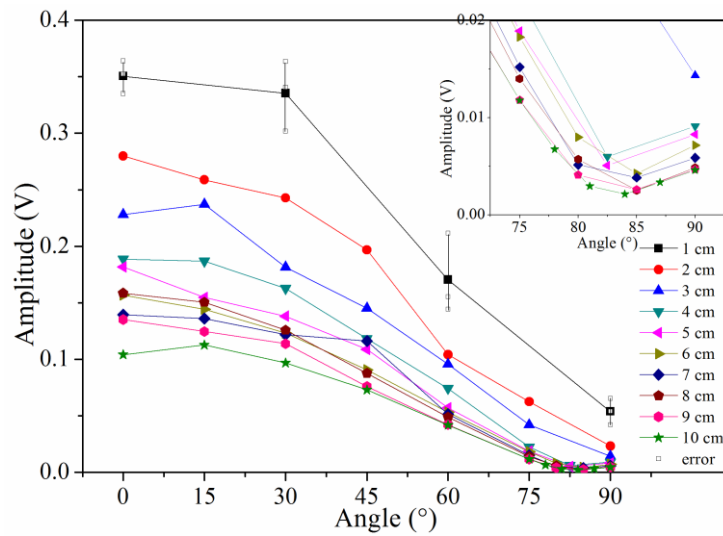
Figure 2.18. Amplitudes of detected waveforms to the angle change for different distances.

Phenomena in area A

The sensitivity distribution in area A is simple because the effect from X-axis strain can be omitted due to the small value of c_x, while the effect from Y-axis dynamic strain can also be omitted due to the plate's geometric dimensions. The open marks in Figure 2.19 are the data from area A. The black curve in Figure 2.19 is obtained by normalizing the data to the value in 0 degrees according to different distances, and this figure shows the cosin function relation between sensitivity and angle. Furthermore, in area A, the detected waveforms and the wave's initial phases are always constant for different distances.
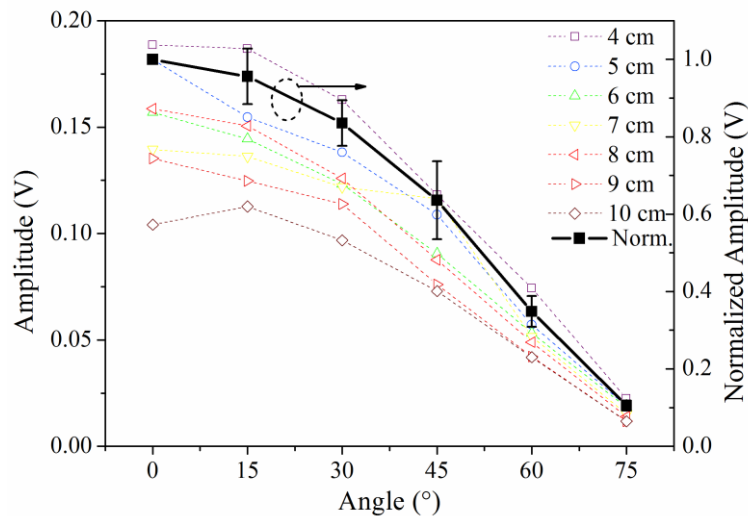
Figure 2.19. After normalization, the sensitivity and the angle show cosine function relation in area A.

Phenomena in area B

Figure 2.20(a) shows the detected waveforms at dots D_2^0, D_2^{75}, and D_2^{90}. The figure indicates that the amplitude of the wave at D_2^{90} further decreases from D_2^{75} and D_2^0. Additionally, the initial phase of the waveform from D_2^{90} is opposite to the initial phase of D_2^0 or D_2^{75}, as shown in the inset in Figure 2.20(a). This phenomenon matches the description in section 3.1, in which lateral strain is dominant for D_2^{90}. Furthermore, the waveforms for D_2^{90} and D_2^{75} differ, and this effect results from different responses to certain frequencies when the ultrasonic wave couples to the fiber from different angles, as explained in section 3.4. Figure 2.20(b) was obtained by doing a Fast Fourier Transform to corresponding waveforms, which is the method applied in all of the following spectral figures of this dissertation. Although the corresponding spectra of D_2^0, D_2^{75}, and D_2^{90} have a similar frequency range and shape, the responses to different frequencies are dissimilar. For example, the difference in amplitudes at frequency 0.32 MHz and 0.71 MHz is 4.1617 dB at D_2^0. However, the amplitude difference decreases to 3.4415 dB at D_2^{75}, while this difference further decreases to 2.1573 dB at D_2^{90}. This decrease is a common phenomenon, which we can observe in almost all cases when the angle changes from 90 degrees to 0 degrees.

Moreover, no α_{min} is observed. The absence of α_{min} occurs because, in area B, the strains from all three axes are present, and the distance between PS-FBG and the ultrasonic source is very short; therefore, in this range, relatively large waveforms can always be detected.
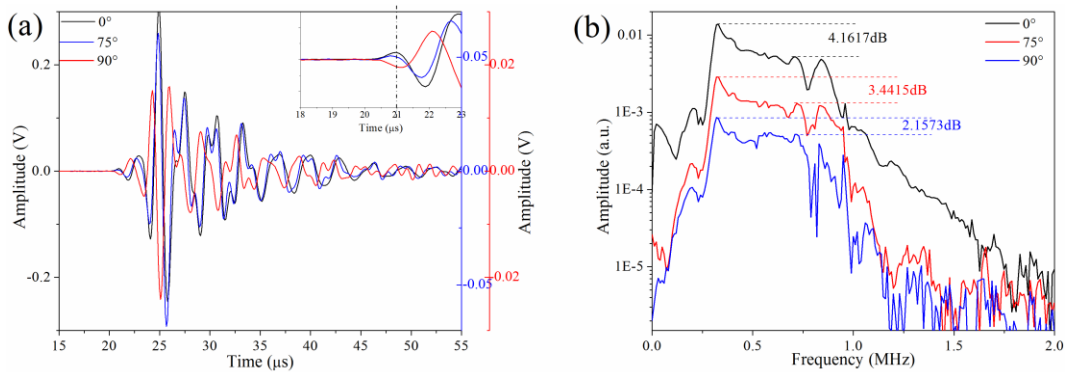
Figure 2.20. (a) Waveforms and (b) corresponding spectra of D_2^0, D_2^{75}, and D_2^{90}

.

Phenomena in area C

Figure 2.21 shows the input waveform and the detected waveforms for D_{10}^{0}, D_{10}^{81}, and D_{10}^{90}, respectively. The α_{min} is around 84 degrees, as shown in the inset of Figure 5, and this value can be explained by the formula for angle α_{min}, as discussed in section 3.3. After undergoing a Hilbert transform, the amplitudes of D_{10}^{0} and D_{10}^{90} are 0.0978 V and 0.0045 V, respectively, as shown in Figure 2.21. Substituting these values into Eq. 2.24, the predicted angle where the minimal amplitude occurs is 87 degrees, which is very close to the observed result.
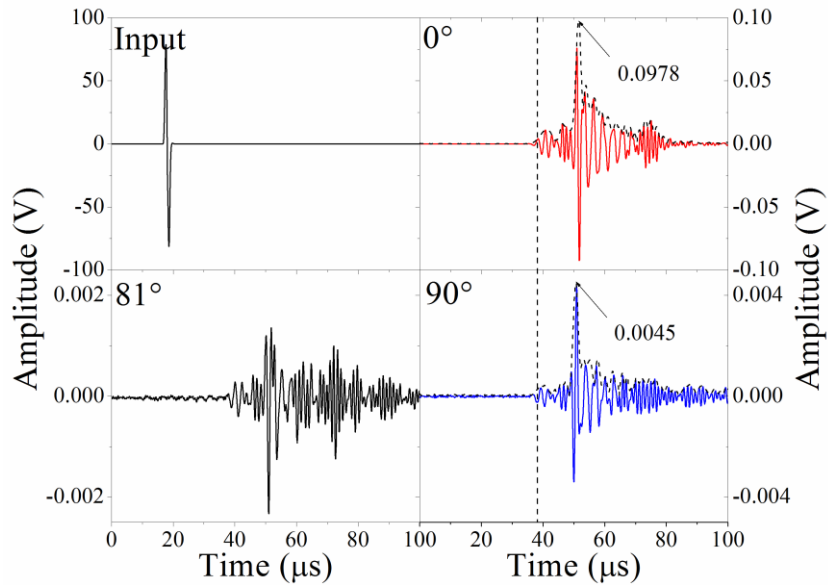
Figure 2.21. Waveforms of input signal, D_{10}^{0}, D_{10}^{81}, and D_{10}^{90}.
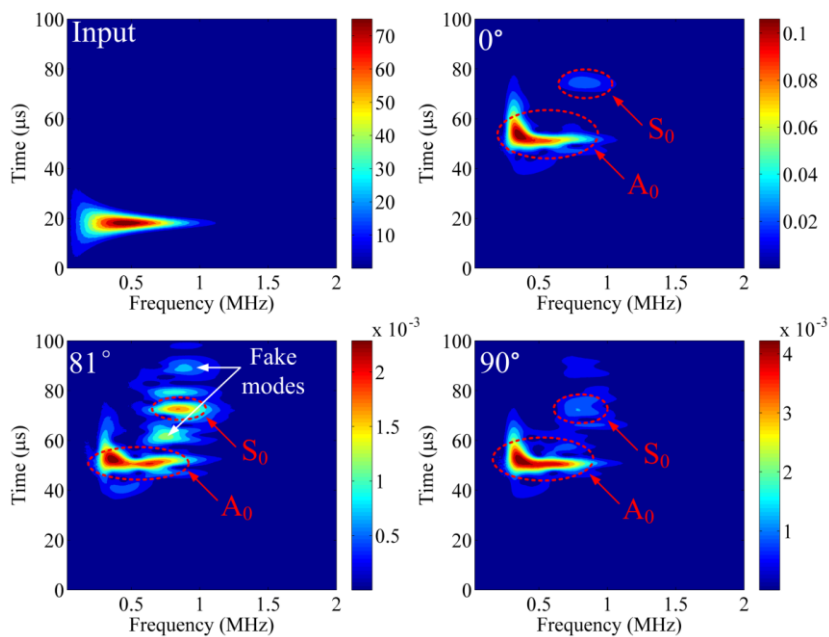
Figure 2.22. CWT results for input signal, D_{10}^{0}, D_{10}^{81}, and D_{10}^{90}.

Furthermore, in Figure 2.21, the waveform at D_{10}^{90} is similar to the waveform at D_{10}^{0} but has opposite phase, the reason for which is explained in section 3.1. However, at the other observational dots between 75 degrees and 90 degrees, the waveforms are not constant and instead show complex waveform changes, such as the waveform for D_{10}^{81}. Continuous wavelet transforms (CWT) are used to further analyze the detected waveforms [19, 21, 69], as shown in Figure 2.22. In the CWT result for the input waveform, the frequency range approaches 1 MHz, and the input time is about 20 μs. The CWT results at D_{10}^{0} and D_{10}^{90} are very similar, and these results present a clear S_0 mode and A_0 mode. The S_0 mode and A_0 mode were determined by subtracting the input signal's arrival time and comparing with the theoretical dispersion curve for this aluminum plate. However, the A_0 mode detected at D_{10}^{90} contains slightly more relative energy in the high-frequency range. Also, the S_0 mode for D_{10}^{90} is more apparent than the S_0 mode at D_{10}^{0}. These phenomena also can be explained as different responses to different frequencies, as discussed in section 3.4. Alternately, although the complex CWT result for D_{10}^{81} contains a major A_0 mode and S_0 mode, there also exist several vague areas. These vague areas will confuse researchers and lead to analysis mistakes. Thus, we call these areas "fake modes" in Figure 2.22. The fake modes occur when the strain from Z axis and X/Y axis are approximately equivalent.

Discussions

For convenience, the sensitivity distribution properties of PS-FBG are divided into areas A, B, and C. However, the stain caused by an ultrasonic wave in the plate is complex and defies simplistic divisions. For example, in area A, although the dominant strain is in the direction of the Z-axis, strains along the X- and Y-axes are also present. Similarly, in area B and area C, strains from all three orthogonal axes also exist. Thus, the above analysis does not fully encompass actual conditions. However, the analyses for results are sufficient to estimate the phenomena in each area.

Although the above discussion is based on results obtained from a PS-FBG sensor, the theory and phenomena can be extended to other FBG sensors or even optical fiber sensors because the PS-FBG or normal FBG is manufactured based on normal single-mode fiber, which has identical physical properties and responds similarly to ultrasonic waves. However, at high frequencies, the response of normal FBG should undergo additional consideration due to the relatively long effective grating length of about 2-3 cm when the ultrasonic wave propagates in the Z-axis. Furthermore, because of the high sensitivity achieved by PS-FBG and the balanced demodulation technique employed, we can observe small changes from 75 degrees to 90 degrees in area C; nevertheless, observation of these phenomena, such as $\alpha_{\min}$, by normal FBG sensors may be difficult.

In this experiment, the fiber was glued to the surface of a plate. The other common attachment method is to embed the fiber into materials, such as carbon-fiber-reinforced plastic laminate. In this case, the coupling performance in the X-axis can be greatly enhanced. Thus, there is a possibility that the ultrasonic wave in the X-axis can also be clearly detected, which leads to a larger $\alpha_{\min}$.

Based on experimental results obtained from 82 excitation dots, the sensitivity distribution properties of the PS-FBG sensor to an ultrasonic wave (employing the surface attachment method) were identified and discussed. Although the strain from both the axial direction and the lateral direction can shift the Bragg wavelength of the PS-FBG, the amount and direction of this shift differ, which leads to the distance dependence and directional dependence of the sensitivity. Furthermore, the location of the ultrasonic source also influences the signals' initial phases, spectra, and CWT results. Moreover, other factors, including coupling performance, the attachment method, and the material's geometric dimensions, also influence the results. These results closely matched the proposed theory. Because of identical physical properties for a single-mode fiber, the grating's sensitivity distribution properties can extend to a normal FBG or even an optical fiber sensor. These results can help optimize sensor networks and signal analyses in the fields of NDT and SHM.

2.5   Attachment Method of Optical Fiber

In ultrasonic SHM, ultrasonic wave is generated artificially or spontaneously, propagating in an objective media, and received by a sensor. For receiving of the wave, the attachment method of the FBG sensor on the surface of the propagation media, which is a CFRP laminate in our research, is important, because the attachment method influences many properties of the sensing system, including sensitivity, strain-free ability, birefringence, *etc*.
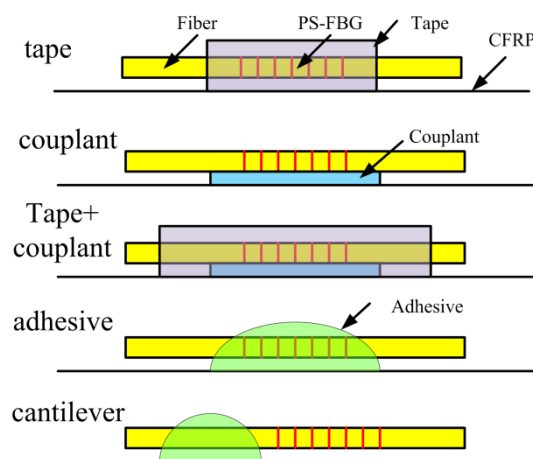
Figure 2.23. Attachment methods of an optical fiber

In this section's research, we evaluated five different attachment methods: 1) using tape to fix the position of PS-FBG; 2) using high-acoustic-impedance ultrasonic

couplant to glue the PS-FBG sensor on CFRP laminate; 3) combining methods 1 and 2 by using both the high-acoustic-impedance ultrasonic couplant and the tape; 4) using cyanoacrylate adhesive to glue the PS-FBG sensor directly; 5) using the cyanoacrylate adhesive to glue the point that is beside the grating area, which constructs a cantilever structure of optical fiber. The structures are illustrated in Figure 2.23. This cantilever fiber attachment method was first proposed by Lee and Tsuda [51, 70]. However, the detected signals by their sensors did not contain information in all frequencies, i.e., their sensor only sensitive to several frequencies due to the resonant property of their cantilever structure. In contrast, the motivation behind our use of the cantilever structure was only to achieve immunity to quasi-static strain because the spectrum of PS-FBG was so narrow that the Bragg wavelength shift caused by quasi-static strain in tensile test easily exceeded the maximal dynamic range of PS-FBG if the grating area was not suspended in midair.

In order to research the different performance, the PS-FBG balanced sensing system with different attachment methods was used in acouto-ultrasonic technique to detect broadband ultrasonic wave. An FG was used to generate an ultrasonic wave: three cycle sinusoidal wave with a hamming window. An E-Amp was used to amplifier the signal to 150 V to drive an MFC actuator. An MFC with 6-mm length was glued on a CFRP laminate with a thickness of 3.4 mm ($[45/0/-45/0]_{3s}$). The N-PZT was also used for a reference measurement in this experiment. The PZT sensor and the PS-FBG sensor are glued 10 cm far from the MFC actuator. However, in cantilever structure, the sensor was glued at two different positions as shown in Figure 2.23. In cantilever 1, the center of the grating is located at 10 cm from the actuator, and in cantilever 2, the adhesive point is at 10 cm from actuator. The geometric dimension and photograph of the experimental configuration are shown in Figure 2.24.
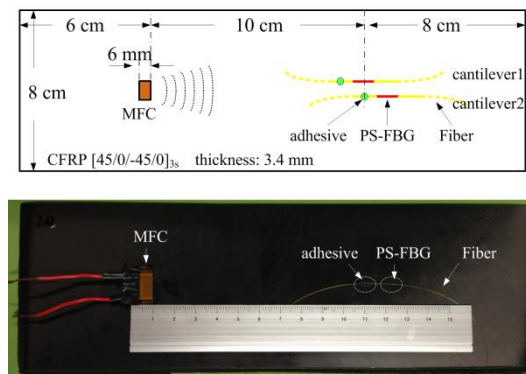
Figure 2.24. Acousto-ultrasonic measurement for a CFRP laminate with the MFC
and the PS-FBG balanced sensing system

Figure 2.25 shows the detected waveforms using the PZT sensor or the PS-FBG balanced sensing system with different attachment methods. All the results of PS-FBG sensor indicate that all the methods can detect the ultrasonic wave precisely without data averaging owing to the high sensitivity of the system. The arrival times

of all the waveforms except the cantilever 2 are the same. The delayed arrival time of the wave measured by the cantilever 2 is caused by the longer distance between the MFC and the PS-FBG. Furthermore, the amplitudes and noise levels of the waves received in the PS-FBG sensing system with different attachment methods are almost the same.
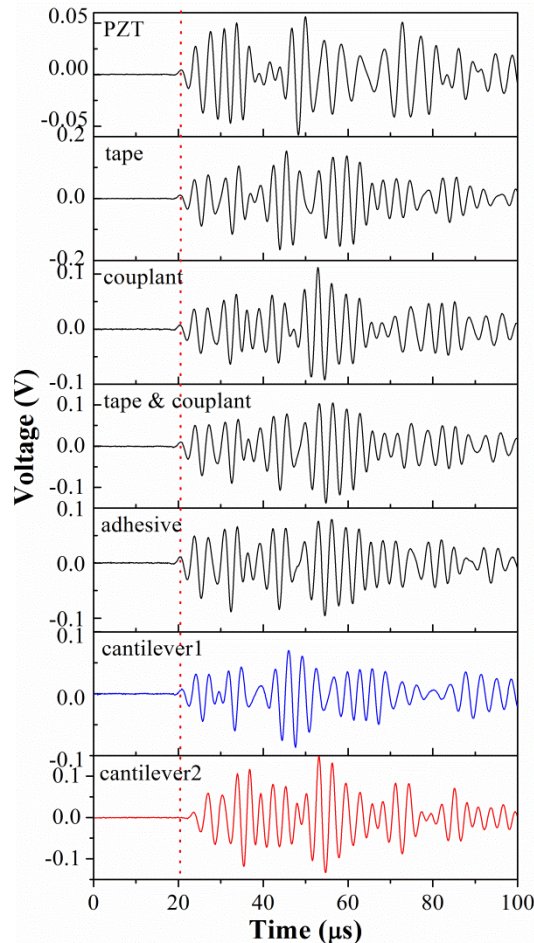
Figure 2.25. Detected waveforms using the PZT sensor and the PS-FBG balanced sensing system with different attachment methods

Figure 2.26 shows the signal-to-noise ratio (SNR) of the PZT sensor and the PS-FBG balanced sensing system using couplant or cantilever structure. The detected signals have the same spectral range from 100 kHz to 500 kHz. The complete and broad spectrum indicates our sensing system can detect high frequency signals without resonance of the cantilever. This maintaining of all the information in the signals is a very useful property of the system for further data processing and analysis. Though the noise level in the PZT sensor is 5 dB smaller than the PS-FBG balanced sensing system, we believe the sensitivity of our system is enough high to be used in practice.
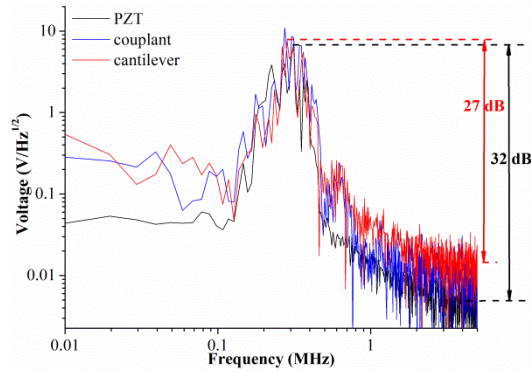
Figure 2.26. SNR comparison between the PZT sensor and the PS-FBG balanced
sensing system using couplant or cantilever structure.

In Figure 2.25, except cantilever 1, the detected waveforms by different attachment methods are almost the same, especially from 20 μs to 70 μs. Then, in order to analyze the detected waveforms in more detail, CWT is applied. Figure 2.27 shows the CWT results of the waveforms detected by PS-FBG balanced sensing system using (a) couplant, (b) cantilever 1 and (c) cantilever 2. The area marked by red circles in Figure 2.27 (a) and (c) are very similar, while it is different in Figure 2.27 (b). The different waveforms and different CWT results of cantilever 1 can be explained as the propagation process of the Lamb wave in the CFRP laminate and the optical fiber. Firstly, the ultrasonic wave propagates in the CFRP laminate as a form of Lamb wave. When wave arrives in the adhesive point, part of ultrasonic wave couples into the fiber and propagates in it, maintaining the waveform. Finally, the wave is detected by PS-FBG sensor with the same waveform as that at the adhesive point. This result indicates that cantilever structure can detect correct waveform at the adhesive point.
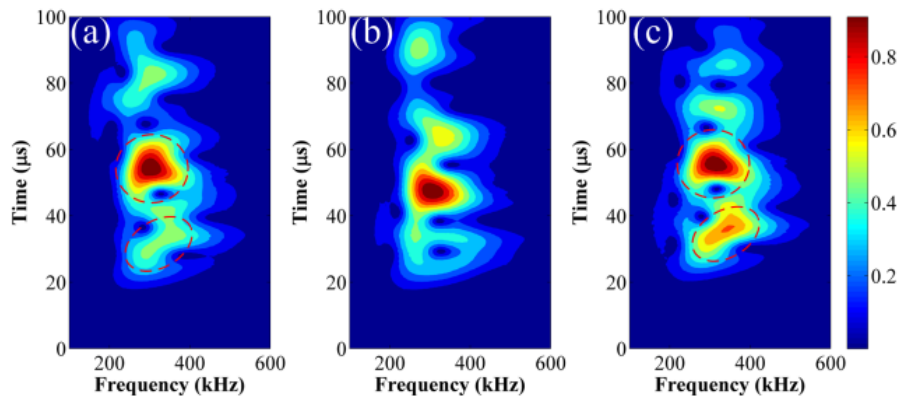
Figure 2.27. Wavelet transform results of the waveforms detected by the PS-FBG
balanced sensing system using (a) couplant, (b) cantilever 1 and (c) cantilever 2

AE signal appears accompanying with defect occurrence, which means that AE signal and quasi-static strain of the laminate are measured together. However, when the static strain is large, the Bragg wavelength of PS-FBG sensor shifts out of the

measurable range of the spectrum because the peak is ultra-narrow. For example, to PS-FBG2, which was used in our practical AE detection experimental discussed in section 4.3 and 4.5, the effective dynamic range is very small. However, in tensile test, much larger strain will be generated. Thus, a strain-free FBG sensor is very important in AE detection application.
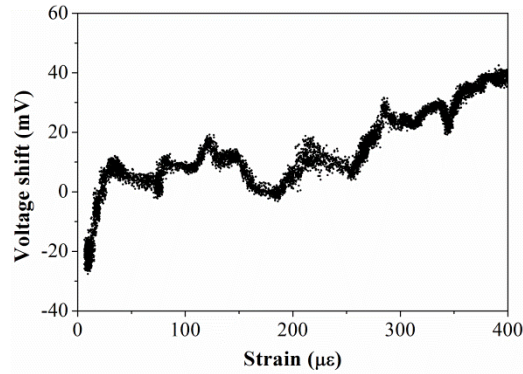
Figure 2.28. PS-FBG balanced sensing system using cantilever structure is insensitive to the strain applied to the laminate by material testing machine. The fluctuation of voltage is derived from the temperature instability.

We conducted experiments to confirm the response of PS-FBG with different attachment methods to quasi-static strain. The PS-FBG was attached on an acrylic plate using different attachment methods. A strain gauge is also glued on the surface to detect the actual quasi-static strain. A material testing machine is used to apply the strain to the plate. As the load increases, the strain detected by strain gauge increases. However, the Bragg wavelength of the PS-FBG sensor is relatively stable in the cases of the couplant and the cantilever, leading to the small output voltage change of the BPD. Figure 2.28 shows the relationship between the strain and the output voltage shift in the case of the cantilever strucure. The variation of the curve is caused by the instable of the temperature. This result indicates cantilever structure is insensitive to quasi-static strain, which is suitable to detect AE signals.

According to the above experimental results and other research results including birefringence and removable property, we evaluate the performance of PS-FBG balanced sensing system and the attachment methods. All the attachment methods of the novel sensing system have almost the same sensitivity, which is only 5 dB less than traditional PZT sensor. Among these methods, the couplant and the cantilever structure is insensitive to quasi-static strain, which is suitable to AE detection of composite materials. Other methods are suitable to be used in acousto-ultrasonic technique. Especially, tape method is easy to remove the sensor and prevents the occurrence of birefringence. All the property of the attachment methods are listed in Table 3.

Table 3. Performance of different attachment methods.

Attachment Methods	SNR	Sensitive to Strain	Birefringence	Removable
Tape		Yes	No	Easy
Couplant		No	No	Easy
Couplant+tape	Similar	Yes	No	Easy
Adhesive		Yes	Yes	Hard
Cantilever		No	No	Hard

In this part of study, we conducted experiments with five different attachment methods under two different experimental conditions, which are ultrasonic detection and tensile test. As a result, it was found that the tape and adhesive method can be used in acousto-ultasonic methods without averaging requirement. On the other hand, in order to detect AE signals with immunity to large quasi-static strain, the cantilever structure is most suitable. We believe that the study on sensor attachment methods have certain function to direct the following researches.

3 CASCADED PS-FBGS SENSING SYSTEM

According to the simulation and analysis in Chapter 2, we have demonstrated that PS-FBG has many advantages compared to normal FBG in the case of ultrasonic detection. We also experimented and researched about the sensitivity distribution properties of PS-FBG and relative attachment method in the ultrasonic SHM for providing enough theoretical direction in the following researches. However, no demodulation systems have been introduced and discussed until now. As discussed in Chapter 1, sensing system with fast response and low noise level is necessary for demodulation the Bragg wavelength shift caused by ultrasonic wave. In this Chapter, we focused on discussion about the demodulation technique based on power detection.

Perez *et al.* accomplished detection of ultrasonic signals using a broadband ASE light source and matched FBGs albeit with very low sensitivity [71, 72]. It may be the first attempt of ultrasonic detection based on the power detection method. Okabe *et al.* used an FBG and an AWG, connected after an ASE light source to detect ultrasonic waves [21, 44, 65]. The FBG used in this system has length of 1.5 mm and very low reflectivity for guaranteeing the detectable bandwidth to ultrasonic signals. Multiplexable configuration is its most advantage; however, this system's sensitivity is still low, leading to averaging of amount of data for noise reduction, which needs much time to finish. Azmi *et al.* used multiple PS-FBGs, one kind of SFBG, to enhance the sensitivity [73]. However, multiple PS-FBGs have a possibility of detection only for low frequency waves. In summary, to the authors' knowledge, there exists no multiplexable sensing system that provides a highly sensitive broadband response.

However, multiplexable sensing system is truly the requirement for acousto-ultrasonic detection or impact damage, where many sensors should collect the data simultaneously. It can be succeeded by using many sensing systems; however, the total cost may be intolerable to commercial applications. Besides that, another method is to connect these sensors to a single demodulation system with multiplexable ability. It will be the best and the most practical choice.

In this chapter, we propose a novel sensing system, called cascaded PS-FBGs sensing system [74]. We demonstrate that this system has relative high sensitivity (highest among FBG sensing system based on power detection), broad bandwidth and multiplexing ability. Then, we further try to detect ultrasonic wave via acousto-ultrasonic detection in CFRP laminates, as well as try to detect impacts in composites [75]. All the results show that this system has large potential applications, especially the acouto-ultrasonic detection.

3.1 System Setup and Detection Principle

Figure 3.1 is a schematic diagram of the cascaded PS-FBGs sensing system. A 22.1 dBm C-band ASE source with a flat spectrum around 1550 nm was used as the light

source. To prevent damage to the fiber end because of the high power, a 5 dB attenuator was attached to the ASE. A circulator and an AFBG were used to create a narrowband light source to illuminate the sensor. This can also be achieved by a 50-GHz AWG, as indicated by the dashed lines in Figure 3.1, because of the similarity of the AFBG and AWG spectra [43, 76]. In this research, we performed experiments based on the AFBG. Two identical PS-FBGs (having spectra of the same shape but marginally different Bragg wavelengths) were used as a sensor and a filter, respectively. The PS-FBG sensor was glued to the middle of a 200×200×1.5 mm^3 (L×W×H) aluminum plate. When the Bragg wavelength of the PS-FBG sensor is shifted by an ultrasonic wave, the final output power of the system fluctuates due to the change of the overlap area of the PS-FBG sensor and the PS-FBG filter. The PD converted the output power fluctuation to voltage signals, which were recorded by the Oscilloscope. Two R-PZTs were used as an actuator and a sensor, respectively. The actuator R-PZT1 was glued 7.5 cm away from the PS-FBG sensor, and the sensor R-PZT2 was glued near the PS-FBG sensor as a reference. An ultrasonic signal was generated by a FG and amplified by an E-amp to drive the PZT1.
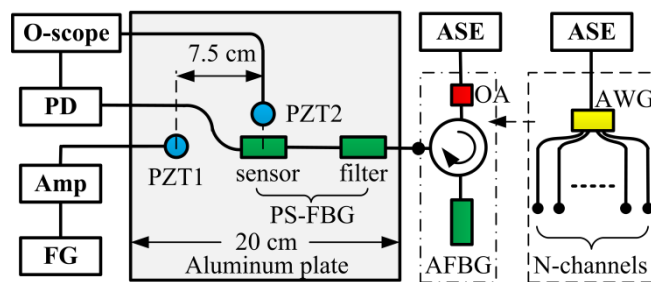
Figure 3.1. Schematic diagram of the sensing system.

In the experiment, two pairs of PS-FBGs were compared, which are PS-FBG1 and PS-FBG2. The length of the PS-FBG2 is 5 mm, and the length of the PS-FBG1 is 10 mm. Figure 3.2(a) shows the transmittances of the pair of PS-FBG2s, the FWHMs of which are 0.018 nm. The Bragg wavelength of the PS-FBG filter is about 1550.08 nm while the Bragg wavelength of the PS-FBG sensor is about 1550.1 nm. Figure 3.2(b) shows the transmittances of the pair of PS-FBG1s, the FWHMs of which are 0.026 nm and the Bragg wavelengths are about 1549.85 nm. The AFBG is designed with a FWHM of about 0.2 nm, similar to a 50-GHz AWG, to filter out the peaks in the spectrum of the PS-FBGs generating an ultra-narrow peak as shown in the insets. The Bragg wavelengths of the AFBG and the PS-FBG filter were adjusted by a small material testing machine used to apply tensile strain such that they were close to the Bragg wavelength of the PS-FBG sensor.
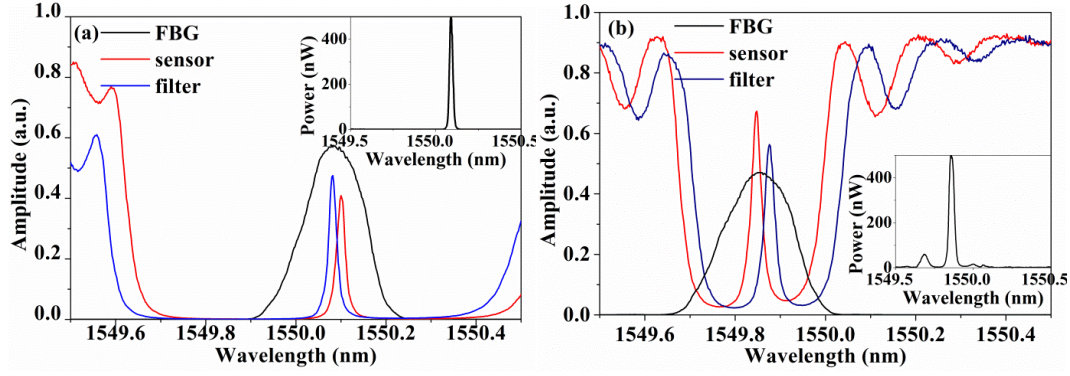
Figure 3.2. The reflectivity of the AFBG and the transmittance of the two pairs of the PS-FBG filter and sensor are obtained using a spectrometer, (a) the pair of PS-FBG2s, and (b) the pair of PS-FBG1s. The insets show the output spectrum of the sensing system with an ultra-narrow peak under different conditions.
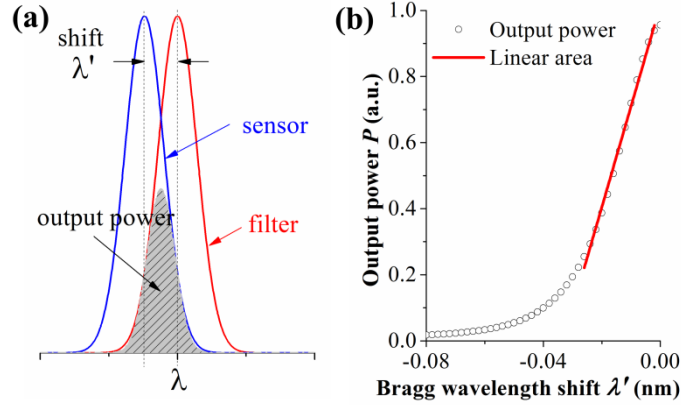
Figure 3.3. Principle of the system: (a) two cascaded PS-FBGs filtering out narrow band light and (b) final output power of the system as a function of the Bragg wavelength shift of the PS-FBG sensor. Linear areas exist in a small range, demonstrating the linear response of the system to ultrasonic wave.

When the Bragg wavelength of the PS-FBG sensor is shifted by an ultrasonic wave, the PS-FBG filter demodulates the Bragg wavelength shift to an optical power change [46]. It was therefore necessary to investigate the relationship between the strain and the output power of the system. Figure 3.3 (a) shows the principle of the system operation. The final transmission property of the system can be calculated by multiplying the transmission properties of the PS-FBG sensor $F_{sensor}(\lambda)$ and the PS-FBG filter $F_{filter}(\lambda)$ with the reflectance property of the AFBG $F_{AFBG}(\lambda)$. The power detected by the PD is the whole power at every wavelength. We can therefore multiply the transmission/reflectance functions with the energy of the ASE light source $I(\lambda)$ and then integrate over the range of the PD. If the PS-FBG sensor is shifted in wavelength λ' the output power of the system P will also change as a function of λ'. The output power of the system is therefore given by:

$$P(\lambda') = \int I(\lambda) F_{AFBG}(\lambda) F_{filter}(\lambda) F_{sensor}(\lambda - \lambda') d\lambda \qquad (3.1)$$

Since the output light power from the ASE light source is flat at around 1550 nm, the optical power is normalized to be equal to 1 at each wavelength. The relationship between the final output power and the Bragg wavelength shift of the PS-FBG sensor was simulated using Eq. 3.1. For a linearly increasing strain, i.e. the spectra of the two PS-FBGs go from being separated to overlapping, an increase in the output power is observed. Although the curve of P is not linear, a quasi-linear area is found over a small λ' range. This is indicated by the red line in Figure 3.3(b). Since the strain resulting from an ultrasonic wave is usually small, we believe this system will have a linear response to the ultrasonic wave and is therefore suitable for acousto-ultrasonic detection.

3.2   System Evaluation

In this section, we evaluated the system's performance via acousto-ultrasonic detection in an isotropic aluminum plate. Firstly, the broadband property of this system was verified. A continuous sinusoidal wave of 0.8 MHz was input into the actuator as an ultrasonic wave source. Figure 3.4 shows the temporal and spectral responses of the PZT sensor and the PS-FBG2 sensor, respectively. The spectral responses are calculated after normalization of the temporal signals, which is the method applied in all the following spectral response figures in this section 3.2. Both sensors can clearly detect the ultrasonic wave at 0.8 MHz. Furthermore, at 1.6 MHz and 2.4 MHz, small resonant signals, maybe caused by harmonic of the input signals, were also observed in both sensors. It indicates that this PS-FBG2 is able to detect signals with frequency at least 2.4 MHz. However, the PS-FBG sensor exhibits more noise than the PZT sensor.
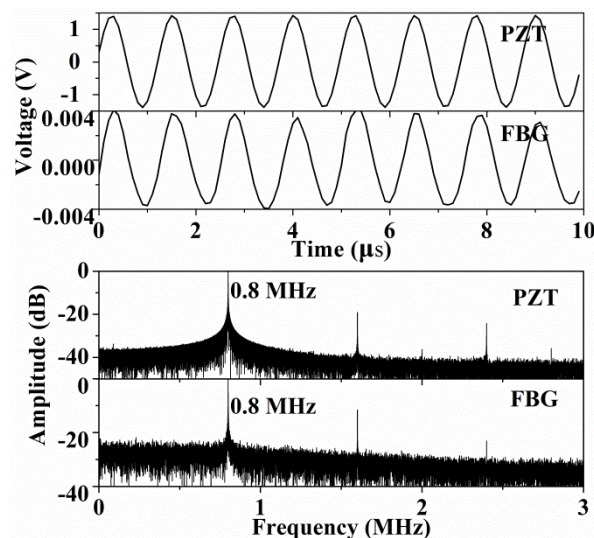
Figure 3.4. Temporal and spectral responses obtained from the PZT and PS-FBG2 sensor, respectively while injecting a 0.8 MHz continuous sinusoidal ultrasonic wave. Both signals showed sensitivity of the PS-FBG sensor to high frequencies.
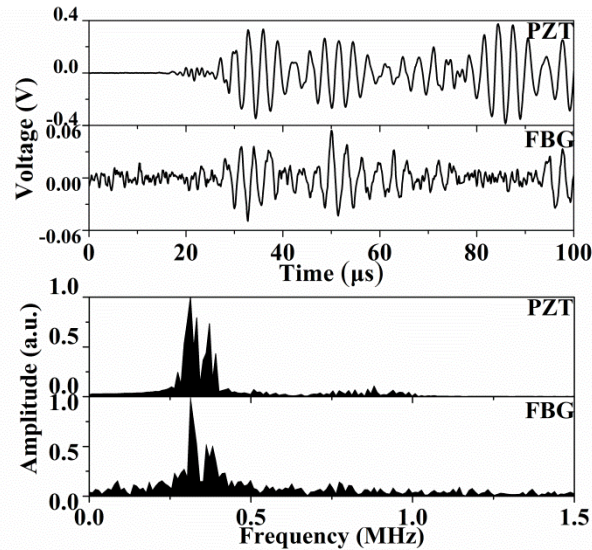
Figure 3.5. Temporal and spectral responses obtained from PZT and PS-FBG2 sensor respectively while injecting 0.3 MHz burst broadband ultrasonic wave. Both PZT sensor and PS-FBGs sensor detected the burst broadband ultrasonic wave simultaneously, while with similar spectral responses from 0.3 MHz to 0.4 MHz.

Secondly, a burst signal was used to generate a broadband ultrasonic wave. The burst voltage signal input to the PZT actuator was a three-cycle sinusoidal wave at 0.3 MHz with a Hamming window. Figure 3.5 shows the temporal and spectral responses of the PZT and PS-FBG2 sensors to this signal. Because of the resonance characteristics of the PZT sensor its signal has larger amplitude than that of the PS-FBG. Both sensors detected the signal at the same time of about 28 μs. Both signals have similar spectra from 0.3 MHz to 0.4 MHz, which are in accordance with the spectrum of the broadband input signal generated by the PZT actuator. The signal can also be obtained using our previous ultrasonic sensor system based on AWG filter; however, a very large amount of measurement data is required for averaging to reduce the noise. The results show that our system is much more sensitive than the previous system, though the achievable range is smaller because of the narrow peak of the PS-FBG. However, for the application of ultrasonic detection, this is not a problem since the strain is always small; it will be an issue for application of impact detection, which will be discussed in section 3.4.

The pair of PS-FBG1s with an FWHM of 0.026 nm and a shorter Bragg wavelength was used to prove the multiplexing potential of this system. Because of the larger FWHM in these PS-FBG1s, which results in a relatively slow slope, the sensitivity is reduced compared to the pair of PS-FBG2s and the signals are buried in the increased noise. Hence, time averaging over 256 readings was performed to decrease the noise, as shown in Figure 3.6. However, the signal received in the 0.026 nm PS-FBGs is still much noisier than that of the 0.018 nm PS-FBGs. The different SNR of the two pairs of PS-FBGs show that the sensitivity of the system can be improved by using PS-FBGs with sharper slopes.
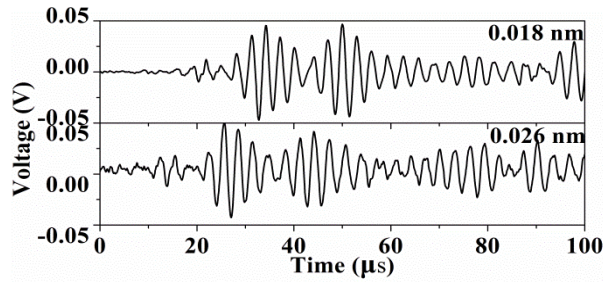
Figure 3.6. 256 time-averaged temporal responses obtained from two pairs of PS-FBGs with different Bragg wavelengths. Using this design, the broadband ASE light source can support multiple channels to establish a practical AE sensor network. Comparing these two curves, the 0.018 nm PS-FBG2 has lower noise and higher sensitivity to ultrasonic waves.

During the experiment, we found that the sensitivity of this cascaded PS-FBG sensing system is related to not only the slope of the PS-FBG, but also to the overlapping position of the PS-FBG sensor and PS-FBG filter. In other words, there exists the best overlapping position to achieve the best sensitivity. However, due the accuracy of the material testing machine and the influence of environmental temperature change, we cannot precisely control the overlapping position. Therefore, in this experiment, we cannot exact demonstrate the relation between the overlapping position and sensitivity. In addition, because the PS-FBG3 with ultra-narrow FWHM is very difficult to be controlled; thus, this type of PS-FBG is not used in this experiment.

Since the ASE light source has about 30 nm of spectral width (from 1530 nm to 1560 nm) and the AFBG or one port of 50 GHz AWG has about 0.2 nm of FWHM, theoretically more than one hundred channels can be achieved by one ASE light source. Normally, a commercial AWG can support more than 40 channels, meeting the needs of practical applications. According to the above analysis, the system described here can greatly increase the number of channels, Therefore this system has multiplexing potential that can decrease the cost of the whole system compared to normal techniques.

Finally, a pencil lead break test was performed to examine the response of this system to the simulated AE signals. In this experiment, the PZT actuator was replaced by a pencil lead break at the same point. In Figure 3.7 broadband AE signal is detected by both sensors and has the same arrival time. The major frequency components of the signal are from 12 kHz to 40 kHz. The spectral response of the PS-FBG contains more energy in the low frequency range, which can be explained as the PS-FBG sensor having a flat response to all the frequency components of the broadband signal while the PZT sensor has a very low sensitivity to low frequency vibrations.

45
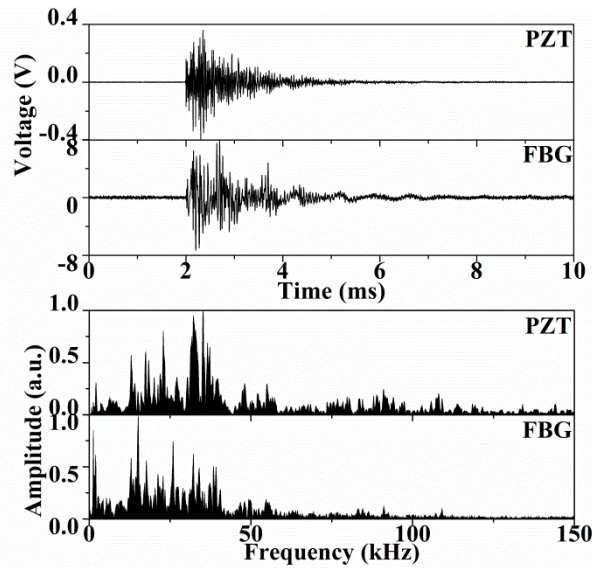
Figure 3.7. PZT sensor and PS-FBG sensor responses to AE signals simulated by a pencil lead break test. Although the temporal and spectral responses have almost the same shape, the PS-FBG is more sensitive to low frequency vibration.

In conclusion, the novel cascaded PS-FBGs sensing system has high sensitivity and broad bandwidth, which can be used to detect weak high frequency ultrasonic waves and AE signals. Because of the narrow FWHM of every channel and the flat broadband characteristics of the ASE light source, it is believed that this system has the potential to multiplex dozens of channels, which is an advantage in practical applications.

3.3   Application to Acousto-ultrasonic Detection in Composites

Although we have demonstrated the relative high sensitivity of the cascaded PS-FBGs sensing system. However, we still wonder whether it can be used in CFRP laminates because the ultrasonic attenuation in CFRP laminates are higher than that in aluminum plate. Furthermore, we also would like to find out whether real time (no-averaging) detection can be achieved in CFRP laminate or not. Thus, we practically conducted an experiment of acousto-ultrasonic detection by this novel system on a CFRP laminate in this section.

An ultrasonic signal with a peak-to-peak voltage of 1.5 V was generated using the FG. The signal was amplified 100 times by E-Amp for feeding enough energy to a MFC actuator of 6 mm in length. PS-FBG2s are used in this experiment for higher sensitivity. A normal 1.5-mm FBG sensor was glued in parallel to the PS-FBG sensor on the CFRP plate ($[45/0/{-}45/90]_{3s}$) with $220{\times}220{\times}3.4$ mm^3 (L$\times$W$\times$H) in dimensions to provide a reference measurement. The MFC actuator was glued 70 mm from the FBG sensors. Epoxy adhesive and cyanoacrylate adhesive were used to glue the MFC actuator and FBG sensors to the laminate, respectively. Figure 3.8 shows the photo of the experimental setup.

46
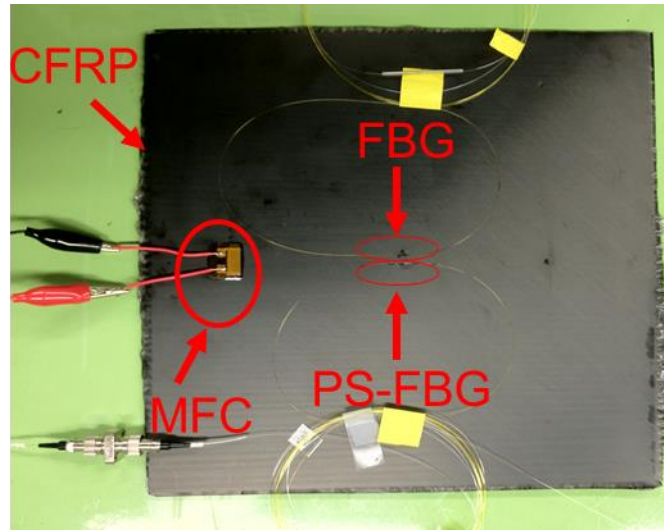
Figure 3.8. Photo of the experimental setup.

The voltage signal input to the MFC actuator was a three-cycle sinusoidal wave with a Hamming window. The waveform and CWT result of the input wave are shown in Figure 3.9(a) and (b) respectively. The major frequency components of the signal are located between 200 kHz and 450 kHz. Figure 3.9(c) and (d) show the waveform and the CWT result of the real-time signal received by our novel system. Despite some background noise, the CWT (Figure 3.9(d)) clearly shows the detected signal.
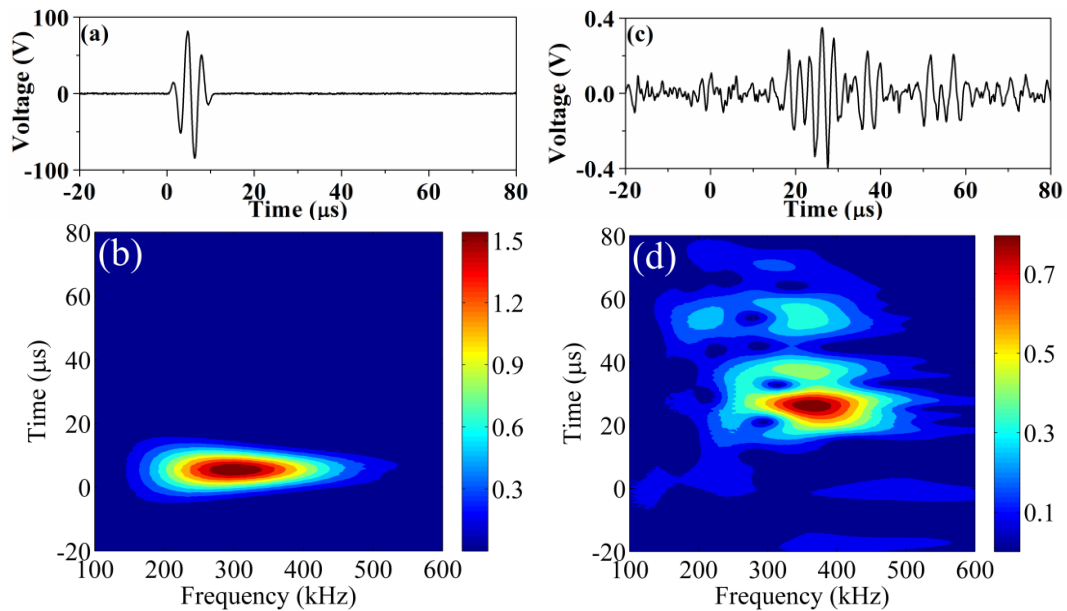
Figure 3.9. Input and received signals: (a) voltage signal input to MFC, (b) CWT result of the input wave, (c) received signal by PS-FBG system without averaging, and (d) CWT result of the received wave.

47
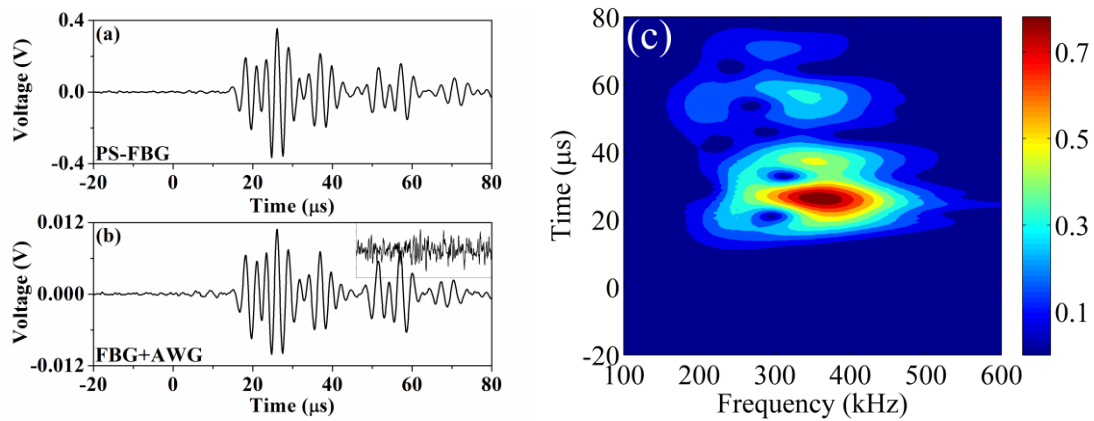
Figure 3.10. Comparison between the received signals in PS-FBG and normal FBG: (a) received signal by PS-FBG averaged 256 times, (b) received signal by normal FBG averaged 4096 times; the inset shows the received signal without averaging, and (c) CWT result of the received signal by PS-FBG.

In order to confirm the high resolution of our novel PS-FBG system, the results were compared with that of previous FBG and AWG system. Figure 3.10(a) and (b) show the waveforms of the received signal from the PS-FBG and FBG sensors. The waveforms are an average of 256 and 4096 measurements respectively. The inset in Figure 3.10(b) shows the real-time signal detected using the FBG sensor without averaging. The unaveraged signal is completely hidden by noise. Comparison of the data in Figure 3.10(a) and (b) shows that the waveforms are the same for both systems. However, the detected signal for the normal FBG has a much lower SNR than the signal detected using the PS-FBG. This higher SNR in the PS-FBG is a result of the high sensitivity of the system caused by the steep slope of the peak in the middle of the spectrum of the PS-FBG. Figure 3.10(c) shows the CWT result of the signal detected by the PS-FBG. The signals in Figure 3.9(d) and Figure 3.10(c), for frequencies between 250 kHz and 450 kHz and times between 20 μs and 60 μs, are almost identical. This means that the novel PS-FBG sensor can precisely obtain the propagated wave in both the time and frequency domains without the need for averaging.

In Figure 3.11(a), the time of the maximum peak is extracted by scanning of maximum CWT coefficients automatically at each frequency from Figure 3.9(d) and Figure 3.10(c). The blue dots indicate the real time signal and the red dots show the averaged signal. The two curves almost overlap each other, particularly for frequencies ranging from 200 KHz to 450 kHz (the frequency range of the input signal). Furthermore, the maximum point occurs at 365 kHz and 26.3 μs in both curves.
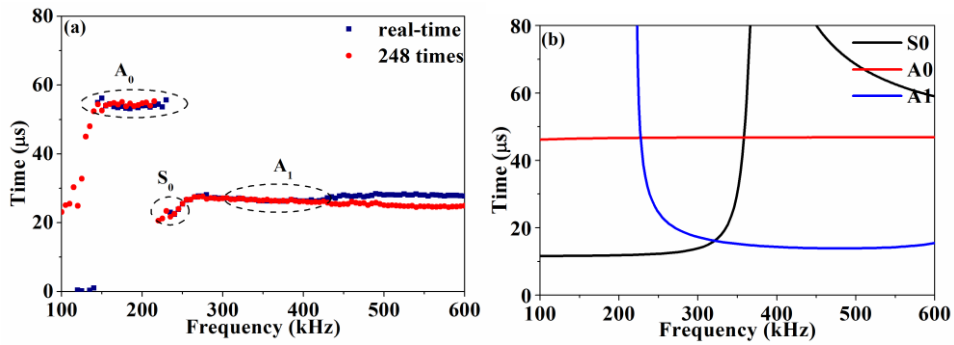
Figure 3.11. Sensitivity of the PS-FBG system: (a) maximum peak points extracted from the CWT results in both real time and averaged 248 times and (b) theoretical dispersion curves of arrival time for a distance of 70 mm against frequency for all modes of Lamb waves in a 3.4-mm-thick CFRP.

The group velocities of the A_0, A_1 and S_0 modes of the lamb wave propagating in the CFRP quasi-isotropic laminate, with a thickness of 3.4 mm, were obtained at each frequency using the DISPERSE software. The propagation times at a distance of 70 mm were determined from the velocities and are shown in Figure 3.11(b). The A_0, A_1 and S_0 modes of the Lamb wave can be determined from the experimental results by comparison with the theoretical dispersion curve, as shown in Figure 3.11(a). According to these results, we demonstrated that this design results in a greatly improved sensitivity allowing the detection of ultrasonic waves in real time. The sensitivity of this cascaded PS-FBGs sensing system is high enough that the A_0, A_1, and S_0 modes of Lamb waves can be identified.

3.4   Application to Impact Detection
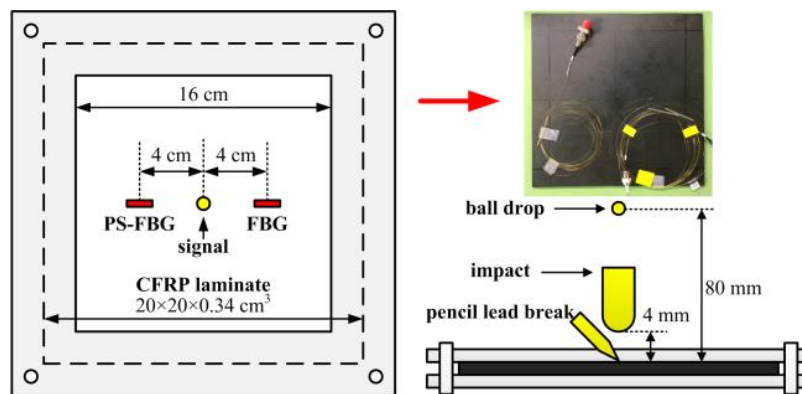
Figure 3.12. Experimental setup: three different signals are detected by out novel system.

Figure 3.12 is the experimental setup. All the AE and impact tests were performed on the CFRP laminate which is the same as that used in the experiment described in section 3.3. This laminate was constrained with two metal frames. Both PS-FBG sensor and normal FBG sensor with 1.5-mm grating length were glued on the CFRP

49

laminate in order to compare the different performances of this novel system and previous system. Both sensors were located 4 cm away from center point of the CFRP laminate, where both simulated AE signals and impacts were generated. First, a steel ball with 5.56 mm diameter and 0.7 g weight was dropped 80 mm above the CFRP laminate as a small impact energy of $E_p = mgh \approx 0.55(mJ)$. A larger impact was also applied by using a drop-weight impact tester with 1 kg weight. The diameter of the head of impactor is 12.7 mm and height to the CFRP laminate is 4 mm distance. Therefore the calculated energy is $E_p = mgh \approx 39(mJ)$. Then, pencil lead break test was conducted to generate a simulated AE signal. However, because the result of the pencil lead break test is very similar to that show in section 3.2, we omit it here.

Figure 3.13 is the waveforms in the small impact test by ball drop. Compared with the detected signal by normal FBG, the detected signal by PS-FBG has higher voltage and better SNR due to the steep slope in the peak. We also performed this small impact test three times to verify the repeatability of this novel system. The results are shown in Figure 3.14. These three waveforms are almost the same. Therefore, we believe the detected wave is reliable.
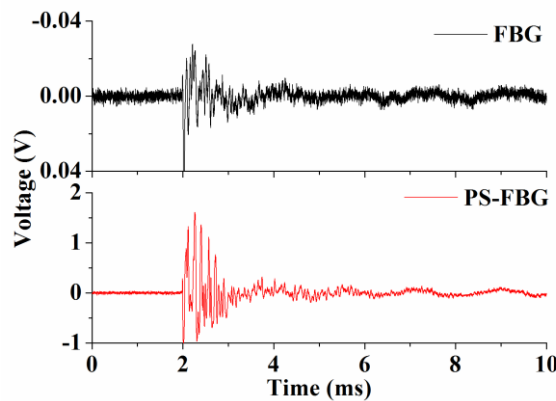
Figure 3.13. Both systems can detect small impact generated by ball drop. However, the detected signal of PS-FBG system has higher voltage and better SNR compared to that of normal FBG system.
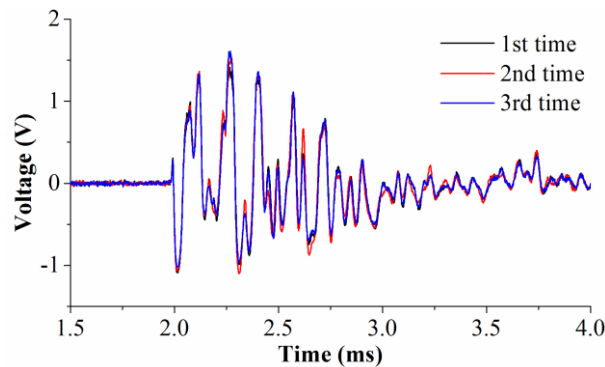
Figure 3.14. The waveforms measured in repeated small impact tests three times.

50
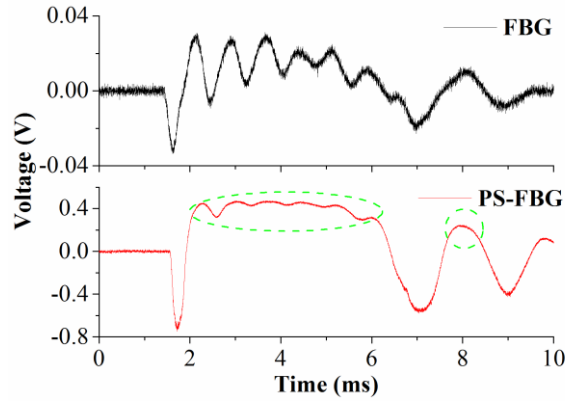
Figure 3.15. Large impact signals were detected by both systems. However, the waveform detected by PS-FBG sensor deformed because of the limited detectable dynamic range due to the narrow peak in the spectrum.

Figure 3.15 shows the waveforms in large impact test detected by normal FBG and PS-FBG. From Figure 3.15, the output voltage of FBG is much lower than the detected signal by PS-FBG sensor, which is similar to the experiment of ball drop impact. However, some areas in the waveform measured by PS-FBG deformed, as shown in the green circles. This is because PS-FBG sensor is shifted out of the dynamic range of PS-FBG filter due to the narrow peak in the spectrum. In other words, the amplitude of fluctuation in these particular areas decreases because the sensor spectrum does not overlap the filter one anymore, which corresponds to the nonlinear area in Figure 3.3 . Therefore the output voltage is no longer a monotonic function to strain caused by impact when the impact energy is large. This problem maybe can be solved or alleviated by certain mathematical method, such as reverse-calculation.

According to the results of impact detection, this cascaded PS-FBGs sensing system is suitable for detection of impact with small energy or from long-distance. Due to the multiplexing ability, many sensors can be attached on an object, and connected to the demodulation system. When impact occurs, these sensors can work simultaneous. The position identification ability can be easily achieved by precisely judging the arrival time of the wave, because of the high sensitivity of the system. However, when performing waveform analysis, the deformation should be paid attention to.

51

4 PS-FBG BALANCED SENSING SYSTEM

In the Chapter 3, we proposed and demonstrated a PS-FBGs cascaded sensing system. The basic principle of that sensing system is power detection. That sensing system is very suitable in acousto-ultrasonic detections. However, due to the phase and amplitude noise in the broadband incoherent light source, the sensitivity of the system was still not sufficient for detecting small AE signals in composites, such as transverse cracks in CFRP laminates. On the other hand, the demodulation technique based on edge filter technique with relative low noise level has the possibility to achieve higher sensitivity.

Usually, a uniform FBG is used as a sensor in the edge filter demodulation technique. Rosenthal *et al*. used a PS-FBG to enhance the sensitivity [76]. Another solution that enhances the sensitivity is to use the transmit and reflect detection method, proposed by Wild *et al*. [77]. In this design, the reflected and transmitted lights are detected by separated PDs, and the resulting signals are subtracted from each other to double the strain signal. However, some deformations of the signal are present due to the large DC component in the signal, and the noise level is almost the same according to the results. Sometimes, in order to achieve better performance, another PD is used to monitor the intensity of the laser, which increases the cost and complexity of the system. Although the sensitivity in these methods is relative high, it is still not enough to use in AE detection, in practice.

Another issue in both power detection method and edge filter method is the conversion of the strain signal encoded in the Bragg wavelength shift to power modulation. To a certain extent, this eliminates the major inherent advantage of the FBG sensor. Hence, the minimum detectable strain is limited by the noise generated in the system. For example, in the edge filter detection method, the noise level is mainly determined by the laser intensity noise. Thus, how to improve the sensitivity is a basic and important issue. The Pound-Drever-Hall technique [78-80] is used to eliminate laser intensity noise from the measurements; thus, frequency-noise-limited ultrahigh sensitivity can be achieved. Although the Pound-Drever-Hall technique has the potential to detect ultrasonic waves, until now the highest achieved frequency has been 20 kHz [80], which is lower than the requirement of AE signal detection. Furthermore, this technique is complicated, and expensive.

Thus, in this chapter, we proposed another sensing system, called PS-FBG balanced sensing system with very high sensitivity, broad bandwidth and simple structure [81]. We demonstrated that this design has enough sensitivity to achieve AE detection of transverse cracks in CFRP laminates. Furthermore, the AE results from tensile test and three point bending test were discussed and analyzed, and many interesting results were found.

4.1   System Setup and Detection Principle

Figure 4.1(a) is a schematic diagram of the PS-FBG balanced sensing system. The PS-FBG used in this chapter is PS-FBG2. The TLS with a 100-kHz linewidth and 0.1-pm tunable resolution is used as a light source. Port 1 and port 2 of a circulator are connected to the laser and the PS-FBG sensor, respectively. The reflected and transmitted light from the PS-FBG are input into the two ports of a BPD. This BPD contains two identical PDs, a two-stage transimpedance amplifier, and a band-pass filter [82]. The gain of the BPD was set to 10 to amplify the small signals. The 5-mm PS-FBG2 sensor is glued onto the surface of a $250 \times 250 \times 2$ mm^3 (L$\times$W$\times$H) aluminum plate. Another 1.5-mm uniform FBG sensor is also glued to the surface in order to compare the different sensitivities among different systems [21]. Both sensors are 50 mm away from the R-PZT actuator in the center of the aluminum plate. A high-acoustic-impedance ultrasonic couplant and a cyanoacrylate adhesive are used to glue the PZT actuator and FBG sensors to the aluminum plate, respectively. A three-cycle sinusoidal burst wave at 0.3 MHz with a Hamming window is generated by an FG, and the peak-to-peak voltage of the wave is amplified to 150 V by an E-Amp to drive the PZT actuator.

The basic principle of this system is edge filter detection, as shown in Figure 4.1. Compared to the spectrum of the FBG or the PS-FBG, the linewidth of the TLS is so narrow, that it can be treated as a single wavelength. Before measurement, in order to balance the reflected and transmitted optical powers entering the two ports of the BPD, calibration of the wavelength of the laser to the 3-dB position of the peak in the transmission spectrum of the PS-FBG sensor is needed. When the Bragg wavelength of the PS-FBG is shifted by the strain caused by the ultrasonic wave, the laser power is modulated, which leads the transmitted and reflected power vibration in port 1 and port 2, respectively. By monitoring the output voltage of the BPD, the ultrasonic wave is detected directly.
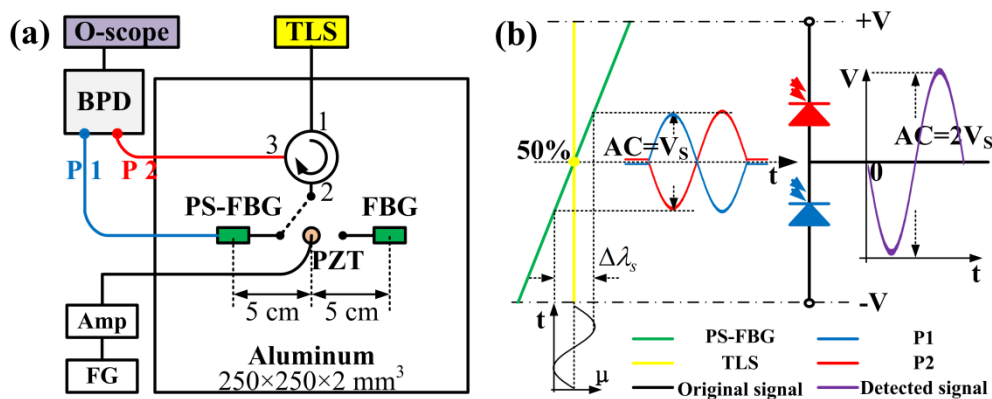
Figure 4.1. Setup and principle of the sensing system. (a) Schematic diagram of the sensing system: O-scope, oscilloscope; Amp, amplifier; FG, function generator; and P1/P2, port 1/port 2. (b) Principle of the sensing system.

The PS-FBG sensor has two functions in this design. First, it guarantees the broadband property of this system; then, it increases the sensitivity significantly due

to the steep peak. Similar to the theory presented in [48, 49], in this system, the AC voltage of the signal can be written as:

$$V_S = \Delta\lambda_S G R_D P g \qquad (4.1)$$

where V_S is the detected AC signal voltage, $\Delta\lambda_S$ is the Bragg wavelength shift caused by strain, G is the grating slope, R_D is the PD's response factor, P is the input laser power, and g is the amplifier's gain setting.
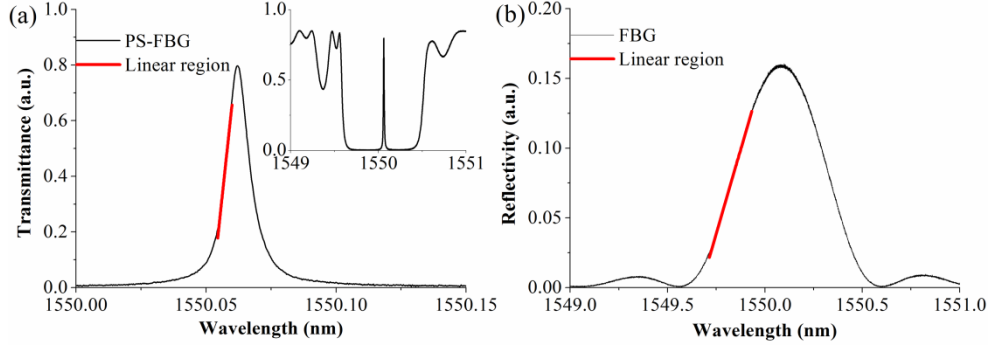
Figure 4.2. Spectra of the FBGs are measured by sweeping the TLS. (a) The sharp peak in the spectrum of PS-FBG has a steep linear region. The inset shows the complete spectrum of the PS-FBG. (b) The spectrum of normal FBG has a linear region with a gentler slope than that of the PS-FBG.

Figure 4.2 shows the spectra of the FBGs we used in the experiment. The sensing range (indicated by the red lines in Figure 4.2) in the FBGs is considered to be the region where there is a linear optical response to strain. This region is defined by using the magnitude of residual form. Compared to these two spectra, the slopes of the PS-FBG and the normal FBG in the linear regions are 87 nm^{-1} and 0.48 nm^{-1}, respectively, which will result in the same input signal yielding detected signals with amplitudes that differ by a factor of about 180 according to Eq. 4.1. Though the dynamic range is smaller in the PS-FBG because of the narrow peak, for the application of ultrasonic detection, this is not a problem since the strain is always small.

The BPD [83, 84] also has three important functions: 1) to remove the large DC component to clearly show the small AC component in a signal, 2) to double the amplitude of the AC signal, and 3) to reject laser intensity noise and common mode noise.

First, in static situations, the reflected and transmitted light powers of the PS-FBG are equal, leading to a 0-V offset in the BPD. This property can effectively prevent large optical power from saturating the output of the PD.

Second, when an AC signal is caused by the Bragg wavelength shift of the PS-FBG sensor, the voltages in port 1 and port 2 will simultaneously experience changes with opposite phases and the same amplitude, which leads to the final output AC signal having twice the amplitude that would be in a single port. Therefore, the final voltage can be written as:

$$V_S = 2\Delta\lambda_S G R_D P g \qquad (4.2)$$

Third, the noise level will decrease because the laser intensity noise and common mode noise will be rejected by the BPD. In a traditional system, there are four main kinds of noise sources. Those are the noise in the PD itself, common mode noise, laser intensity noise, and laser frequency noise. The measured noise can be written as Eq. 4.3, because all of those noise sources are uncorrelated.

$$V_N = \left(V_{IN} + V_{FRE} + V_{COM} + V_{PD}\right)g \qquad (4.3)$$

where V_{IN}, V_{FRE}, V_{COM}, and V_{PD} are the voltages corresponding to the laser intensity noise, the laser frequency noise, the common mode noise, and the PD's noise, respectively. Among these noises, laser intensity noise is dominant. By using the BPD instead of the traditional PD, the laser intensity noise is rejected automatically because it causes the voltages in both PDs to fluctuate in the same way. For the same reason, the common mode noise in our system is also rejected. Thus, under ideal conditions, the noise voltage in the final output of the BPD can be written as:

$$V_N = \left(V_{FRE} + V_{PD}\right)g \qquad (4.4)$$

Furthermore, according to the Eq 2.20, the Bragg wavelength shift is proportional to the applied strain when the ultrasonic wave propagates along the fiber, as expressed in Eq. 4.5:

$$\Delta\lambda_S = a\varepsilon \qquad (4.5)$$

where a is a parameter which can be treated as a constant at a certain wavelength. In this research, the Bragg wavelength is around 1550 nm; thus, the expected value is a 1.2-pm change as a result of applying 1 µε to the Bragg grating. The minimum detectable strain is defined as the strain when the voltages generated by the signal and noise are equivalent:

$$V_N = V_S \qquad (4.6)$$

By substituting Eq. 4.2, Eq. 4.4, and Eq. 4.5 into Eq. 4.6, the minimum detectable strain is expressed as:

$$\varepsilon_{min} = \frac{V_N}{2aGR_D Pg} = \frac{V_{FRE} + V_{PD}}{2aGR_D P} \qquad (4.7)$$

Eq. 4.7 indicates that the gain setting in the PD has no influence on the minimum detectable strain. Furthermore, as we know, V_{PD} is irrelevant to P, but V_{FRE} is proportional to P. Thus, increasing the input laser power partially functions to improve the minimum detectable strain, but the improvement is not linear with the laser power increase. In addition, because of the narrow linewidth of the TLS, V_{FRE} is enough small to compare with V_{PD}, as is demonstrated in the following experiment. For better analyzing the sensitivity of the system, Eq. 4.7 also can be written in the form of power spectral densities (PSDs), given by:

$$S_{\varepsilon}(f) = \frac{S_{V_{\mathrm{N}}}(f)}{2aGR_{\mathrm{D}}Pg} \qquad [\varepsilon/\mathrm{Hz}^{1/2}] \qquad\qquad (4.8)$$

4.2   System Evaluation

In this experiment, the performance of the BPD was verified firstly. Four different sets of experimental conditions were tested: 1) the BPD without laser input, 2) laser power of 0 dBm input into port 1 of the BPD, 3) laser powers of 0.13 dBm and -0.3 dBm input into port 1 and port 2 of the BPD, respectively, and 4) laser power of 0 dBm input into each of the ports of the BPD. The band-pass filter in the BPD was not used in this experiment. The DC voltages in each of these conditions were 0.0057 V, 6.3499 V, 0.8588 V, and -0.0008 V, respectively. The voltage in condition 1 means that this BPD was not perfectly balanced. However, we believe this low offset voltage barely influenced the experimental results. The voltages in other conditions show the ability of this BPD to remove the DC voltage in the signal, and the more balanced the optical powers are, the better the elimination of DC voltages is.
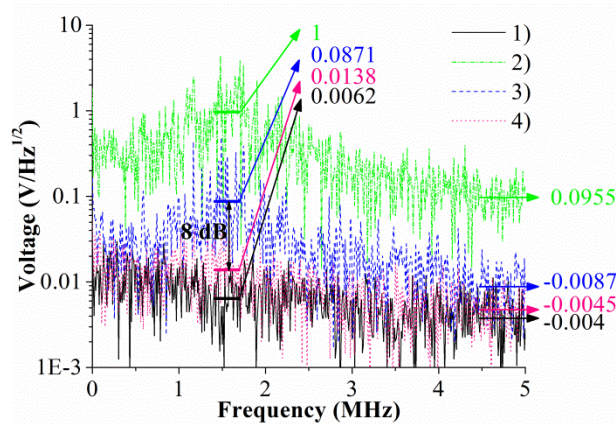
Figure 4.3. The noise levels under the different experimental conditions. The BPD has the ability to reject the laser noise, especially when the input laser power in two ports of the BPD are balanced. The noise rejection performance achieves an effective noise level that is approximately the same as the noise in the BPD without laser input.

The PSDs of the AC voltage signals are shown in Figure 4.3 to illustrate the noise rejection ability. The PSDs are calculated by the FFT of the temporal response, which is the method applied in all of the following PSD figures. In Figure 4.3, condition 2 indicates the largest noise level, while conditions 3 and 4 have lower noise levels, especially when the power in both ports of the BPD is matched. This phenomenon means that the BPD has efficient noise rejection ability, as suggested by Eq. 4.4. Though the DC component in condition 3 is small, the noise level is 3 dB larger at high frequencies and 8 dB larger at 1.5 MHz than that in condition 4, which means that in order to reject laser intensity noise, critical balancing of the powers of the two ports is very important. Thus, when the DC voltage is removed, the BPD will achieve

the best performance. Moreover, the noise level in condition 4 is slightly higher than that in condition 1. The possible causes for this difference are the interferometric noise [47], because the end of the fiber used in this experiment has a PC connector.
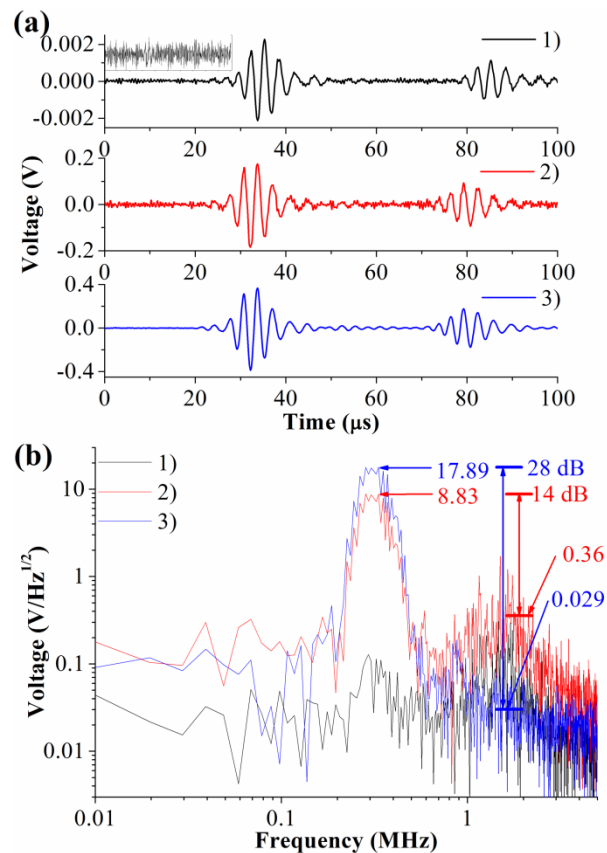
Figure 4.4. Temporal responses (a) and PSDs (b) obtained from three different sensing systems. Curve 1 is the signal obtained by the normal FBG sensing system after averaging over 1024 samples, and the inset in (a) is the detected signal in the same condition but without averaging. Curve 2 is the signal obtained by the PS-FBG sensing system. Curve 3 is the signal obtained by our novel PS-FBG balanced sensing system.

In the second experiment, a comparison of three different FBG sensing systems was performed to determine the SNR improvement of our system. Those systems are: 1) normal FBG sensing system [85], 2) PS-FBG sensing system [61], and 3) our novel PS-FBG balanced sensing system. The laser power was set to 0 dBm. In this part of the experiment, the band-pass filter in the BPD was set to transmit 10 kHz–12 MHz to filter out the low-frequency variation of the Bragg wavelength of the PS-FBG caused by temperature fluctuations. Figure 4.4 shows the temporal responses and PSD curves of the experimental results. The temporal responses in condition 2, condition 3 and the inset of condition 1 are real-time waveforms, and the temporal response in condition 1 is the averaged waveform. All the systems can detect the ultrasonic wave correctly. The AC amplitudes in each condition are 0.0044 V, 0.36 V, and 0.7552 V, respectively. The AC amplitude of condition 3 is larger than that of condition 2 due to

the property that this system uses both the reflected and transmitted light modulated by the PS-FBG. However, the amplification is not precisely a factor of two because the laser is not located in the 3-dB position of the transmission spectrum of the PS-FBG due to the 2-dB insertion loss from port 2 to port 3 of the circulator used in this experiment. Therefore, in order to compensate for the insertion loss of the circulator, the wavelength of the TLS is positioned at about the 5-dB position. Furthermore, the AC amplitude of condition 2 is 82 times larger than that of condition 1 due to the different slopes, as can be seen from Eq. 4.1. The actual amplification is also smaller than the prediction because the laser wavelength offset at the 5-dB position causes the slope to decrease. We believe that the performance of this system can be further developed by using a circulator with a small insertion loss. Furthermore, the effective ultrasonic bandwidth of the PS-FBG2 is wider than that of the normal FBG, as demonstrated section 2.3.3. Another explanation is that this is caused by the variation in strain coupling between the plate and sensor due to bonding variations. From Figure 4.4 (b), it is obvious that our novel system has the best SNR, as high as 28 dB, which is 14 dB better than the SNR in the PS-FBG sensor and about 30 dB better than that in a traditional FBG sensor. Moreover, the FBG sensor has the worst SNR, which requires averaging over 1024 samples to decrease the noise level for manifesting the wave enough to prevent it from being buried under the noise.
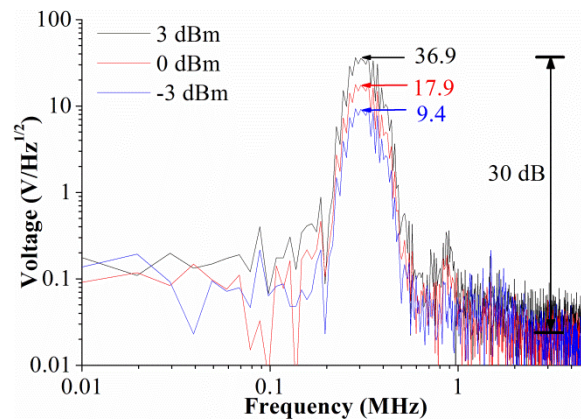
Figure 4.5. By changing the input laser power to three different levels, the detected signal is shown to be proportional to the laser power, but the increase of the noise level is much smaller than the increase of the laser power. The best SNR achieved in this experiment was 30 dB, which was when an input laser power of 3 dBm was used.

The performance of the system under different input optical powers was also tested, as shown in Figure 4.5. The input laser power was changed to 3 dBm, 0 dBm, and -3 dBm, while other experimental conditions were the same as in the above experiment. Figure 4.5 shows that the received signals also have 3-dB differences in each case, matching the differences of input laser power. Although the noise generated by the 3-dBm laser input is the largest and the noise generated by -3 dBm is the smallest, the difference between them is much less than 6 dB. This phenomenon matches the theory in Eq. 4.7 very closely, which means that both the PD's noise and

58

the laser frequency noise contribute to the final detected noise and that these two types of noise are comparable. Increasing the input laser power can partially improve the performance of the system. When 3-dBm laser power is used, an SNR of about 30 dBm can be achieved in this experiment.

In order to verified the performance of the PS-FBG balanced sensing system, more experiments were conducted.

A high-speed amplifier is always necessary for amplifying an ultrasonic wave to a large amplitude in other experiments [21, 85]. Thus, every PZT actuator needs an amplifier, leading to an expensive system. However, due to the high sensitivity in our system, a high-speed amplifier is no longer necessary. The PZT actuator was connected to the function generator directly in this experiment. Signals with peak-to-peak voltages of 10 V, 1 V, and 0.1 V were input into the PZT actuator, respectively. The band-pass filter in the BPD was set to transmit 10 kHz–1 MHz to filter out the high frequencies in order to improve the SNR further. The input laser power was 3 dBm. Figure 4.6 shows the PSDs of the system for signals of different input levels. From Figure 4.6, the signals for each of the experimental conditions are separated by differences of about 10 dB, which is proportional to the input amplitude of the input signal.

Under a separation of 5 cm between the PZT actuator and the PS-FBG sensor and a laser input power of 3 dBm, the strain generated by a 0.1-V signal is considered to be the minimum detectable strain because the signal level is almost the same as the noise level. At the 5-dB position, the slope of the PS-FBG is G =70 nm-1. The PD's response factor R_{D} is 1 V/mW. The detected noise level is V_{N} = 0.03 V/Hz$^{1/2}$. According to Eq. 4.8, the corresponding minimum detected sensitivity in this system is calculated as: $\varepsilon_{\min}$ = 9 nε/Hz$^{1/2}$.
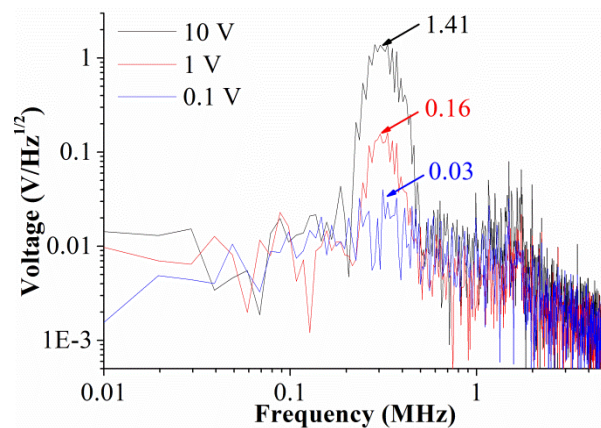
Figure 4.6 Due to the high sensitivity the system achieved, the generated ultrasonic waves without the need for an amplifier could be detected. In the experimental condition indicated by the blue line, the minimum detectable strain was generated by a 0.1-V signal, and the corresponding minimum detected sensitivity in this system is 9 nε/Hz$^{1/2}$.
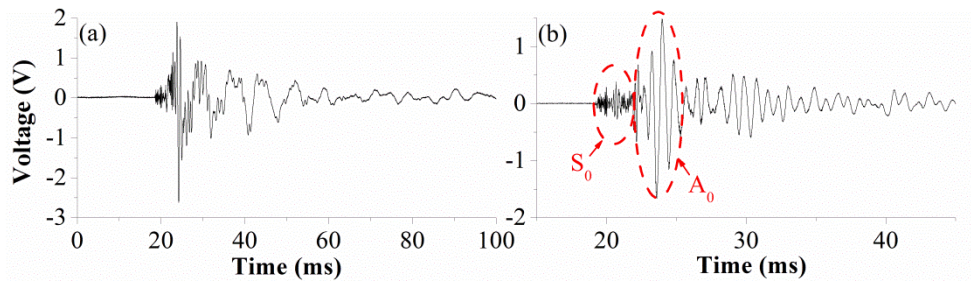
Figure 4.7. Detected AE signal generated by the pencil lead break, measured at a distance of 1 m. (a) Detected wave without a filter presents the sensitivity to both high and low frequencies. (b) Detected wave after the high-pass filter, showing the S_0 and A_0 modes of the Lamb wave clearly.

Then, a simulated AE signal generated by pencil lead break test was also performed to verify the practical application of this system. In this experiment, the testing subject was changed to a long, thin steel plate with dimensions of $1000 \times 35 \times 1.5$ mm^3 (L×W×H). The AE signal source was generated by breaking a pencil lead at one end of the plate, and detected by our sensing system at the other end. A laser input power of 0 dBm was used. Figure 4.7(a) shows the wave detected without a filter, which contains both low- and high-frequency signals. In order to obtain only the AE signal at high frequency as measured by the traditional PZT sensor, the band-pass electrical filter was set to a low cut-off frequency of 1 kHz. In the AE signal detected after the filter, as shown in Figure 4.7(b), the S_0 and A_0 modes of the Lamb wave are clearly separated. We believe this result shows strong potential for application to non-destructive testing.

In conclusion, a high-sensitivity ultrasonic PS-FBG balanced sensing system was proposed and demonstrated in this study. By adjusting the wavelength of the TLS, the reflected and transmitted optical powers of the PS-FBG sensor were balanced in two ports of a BPD. The BPD was used to detect the optical power modulated by the Bragg wavelength shift. Using the strain encoded in the Bragg wavelength shift, an ultrasonic wave was detected. The requirement of high sensitivity in ultrasonic testing is satisfied by two aspects of this approach: 1) the steep slope of the peak in the PS-FBG spectrum and 2) the ability of the BPD to eliminate the DC signal, double the AC signal, and reject the laser intensity noise and the common mode noise. Both theory and experimental results show that the system is immune to laser intensity noise, leading to the achievement of high sensitivity, which is limited by BPD's noise and laser frequency noise. The experimental results show that the sensitivity of this novel system is 14 dB and 30 dB higher than that of the PS-FBG sensor and the FBG sensor, respectively. The detectable sensitivity in this system is 9 nε/Hz$^{1/2}$. Moreover, a 0.1-V ultrasonic signal can be detected without the help of an amplifier, and a simulated AE signal at a distance of 1 m from the PS-FBG senor can be detected precisely. Due to the high sensitivity, broadband property, simple structure, and low cost, this system presents the potential for many practical applications, such as the AE detection in composite materials.

It is believed that the sensitivity of this sensing system can be further improved by using PS-FBG3 with ultra-steep slope. However, the PS-FBG3 is very difficult to be controlled and stabilized, because the temperature change easily shifts the Bragg wavelength out of the dynamic range. On the other hand, PS-FBG3 is not suitable for AE detection. Although common AE signals in composites have low energy, AE signals generated by fiber breaking have large energy, which can be seen in section 4.3. If we use PS-FBG3, the detected fiber breaking AE signals will have deformation perhaps. Therefore, we believe the PS-FBG2 is most suitable in this PS-FBG balanced sensing system.

4.3 Application to AE detection in Tensile Test 1

The experiment described in section 4.2 evaluates the performance of the PS-FBG balanced sensing system. In the section 4.3, 4.4 and 4.5, we will discuss its application in ultrasonic SHM of composites. Because section 2.5 has already proved its ability in acousto-ultrasonic detection, we will discuss its application in AE detection in the following three sections.

There are several FOSs proposed for the AE detection of composite materials based on the micro-bending concept [86], Fabry-Perot cavity [87], special coupler structure [88], and FBG [51, 89]. Although these techniques [86-89] can detect certain AE signals, their sensitivities are still low so that they only can detect large AE signals occurring near the final damage stage of CFRP laminates. Additionally, the number of cumulative hits detected by these FOSs is much lower than the number of cumulative hits detected by PZT sensors. Although the system [51] has relative high sensitivity, it cannot truly reflect the property of the AE signals because it is only sensitive to several frequencies due to its resonant structure. To our knowledge, no FOS that can detect small AE signals produced by transverse cracks has been reported.

In this study, we used improved PS-FBG balanced sensing system for AE detection of CFRP laminates in tensile test. Besides the components described in section 4.1, the system was improved in fiber attachment method, feedback controller, data acquisition system and data process methods. This system thus features a broad bandwidth, high sensitivity, and quasi-static strain immunity, satisfying the requirements of AE detection in CFRP laminate. Applying this novel system in an actual AE detection experiment, we succeeded in observing the Kaiser Effect and distinguishing AE signals generated by transverse cracks and fiber breaking, which were confirmed by the contrastive results from a PZT sensor. We also used a microscope to observe the transverse cracks at a low strain level for further verification.

4.3.1 *Experimental setup*

Figure 4.8 shows the experimental setup for AE detection in CFRP laminates. The practical application of the PS-FBG balanced sensing system requires systematic

stability and data acquisition, because the temperature change easily shifts the Bragg wavelength and many AE hits will occur in the tensile test. Thus, an O-scope was used to monitor the DC output of the BPD and create a feedback control loop to stabilize the wavelength of the TLS. The AC signals were collected by commercial AE-DAQ1 with a sampling frequency of 10 MHz. A Pre-Amp2 with an amplification factor of 30 dB was used before the DAQ to amplify the small signals, and a digital filter with a bandwidth from 20 kHz to 2 MHz integrated in the DAQ system was also used to filter out the signals. The data length recorded was 3k.
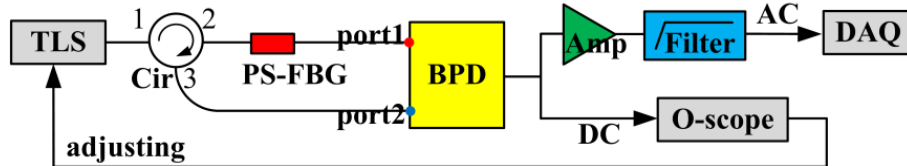
Figure 4.8. Experimental setup for AE detection in CFRP laminates.

Three CFRP laminates with dimensions of $175 \times 13.5 \times 1.15$ (L×W×H) mm^3 ($[0_2/90_2]_s$) were used in this research. One specimen was used to calibrate the FOS. The other two CFRP specimens were tabbed by 1.2-mm-thick aluminum at each end of the CFRP laminates for AE detection in tensile test. Thus, these two specimens have an effective length of approximately 112 mm. The edges of these CFRP laminates are carefully polished for later microscopic observation of the transverse cracks.

N-PZT with a diameter of 20 mm and height of 20 mm was utilized to compare the performance of the novel FOS. This N-PZT sensor is a non-resonant sensor and thus has a broad bandwidth and relatively flat sensitivity, similar to the properties of the PS-FBG. The signals detected by the PZT sensor were first amplified by a Pre-Amp1 with amplification factor of 40 dB and then also collected by the AE-DAQ1 with the same filter setup and data recording length as the setting for the FOS.
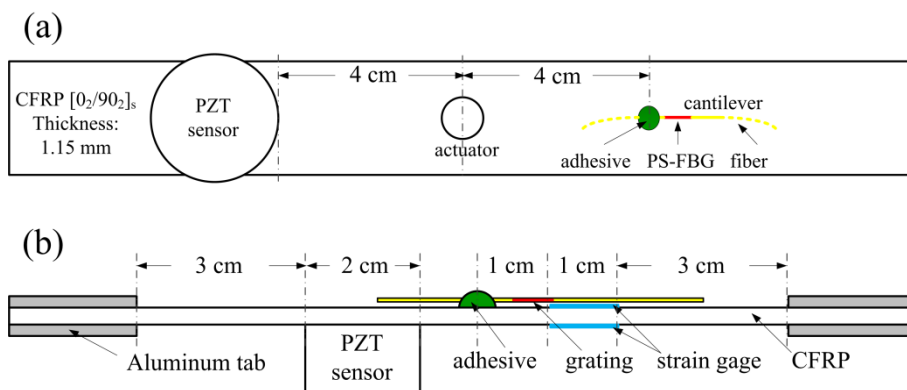
Figure 4.9. Setup of the CFRP specimen. (a) Setup for the calibration of the FOS.
(b) Setup for AE detection in tensile test.

Figure 4.9(a) shows the setup for the calibration of the FOS. In this experiment, the CFRP laminate without aluminum tabs was used. The R-PZT with a diameter of 3 mm and height of 3 mm was used to generate simulated ultrasonic waves. The voltage signal with peak-to-peak voltages of 20 V input into the PZT actuator was a one-cycle sinusoidal wave at 500 kHz with a Hamming window generated by the FG. The ultrasonic wave was received by a FOS and a N-PZT sensor 40 mm apart from the R-PZT actuator. The PZT sensor was glued by a high-acoustic-impedance ultrasonic couplant. The FOS was attached by applying cyanoacrylate adhesive near the grating area of the PS-FBG to create a cantilever structure. Figure 4.9(b) shows the setup for the AE detection in tensile test. In this experiment, CFRP laminates with tabs were stretched by an MTM. In addition to the FOS and PZT sensor for AE signals detection, two strain gages with length of 10 mm were glued on both surfaces of the CFRP laminates to monitor the strains. The strains were recorded by a data logger. The FOS, PZT sensor, and strain gages were arranged as shown in Figure 4.9(b). Figure 4.10 is the proto of the experimental setup.
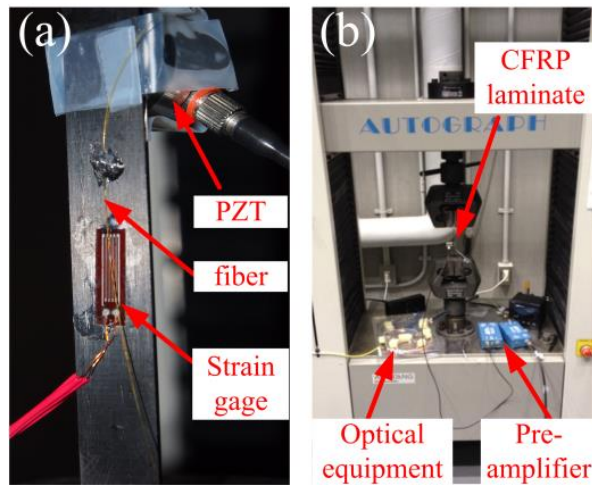
Figure 4.10. Photo of the experimental setups. (a) CFRP laminate; (b) tensile testing machine.

4.3.2 *AE detections in tensile test*

Calibration

Before the actual AE experiment, we calibrated the performance of our novel FOS for ultrasonic waves. Although, we have demonstrated its performance in section 4.2 and section 2.5, the performance of the sensing system after connecting preamplifier and data acquisition system maybe changes. Figure 4.11(a) shows the waveforms detected by the FOS and PZT sensor. Both sensors succeeded in detecting the ultrasonic waves. In Figure 4.11(a), both waves arrive at the same time, but the waveforms are different. It is because that FBG is mainly sensitive to the horizontal strain, whereas the PZT sensor is mainly sensitive to the vertical strain. On the other hand, the ultrasonic waves propagated in the CFRP laminates are Lamb waves with extensional modes and flexural modes. Thus, the waveforms detected by the FOS and PZT sensor are usually different.

63
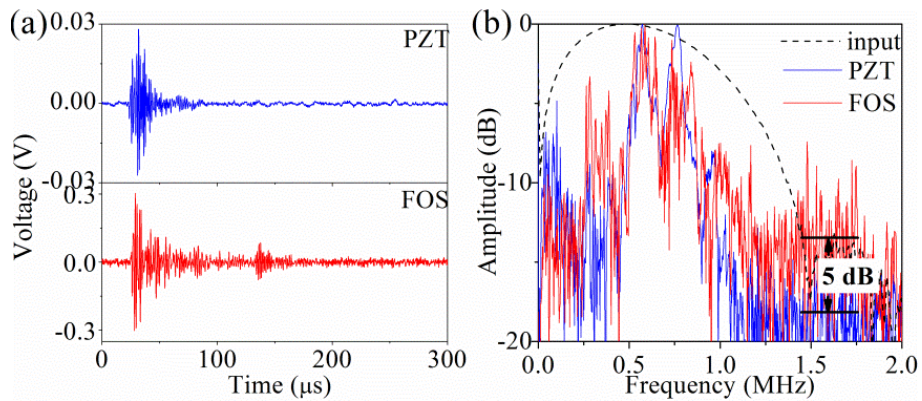
Figure 4.11. Waveforms and spectra for the calibration of the FOS. (a) Detected waveforms by PZT sensor and FOS; (b) corresponding spectra of input signal and signals from the PZT sensor and FOS.

The spectra in Figure 4.11(b) show the root mean square amplitude of the corresponding signals detected by the FOS and PZT sensor, calculated by FFT and then normalization. Although the waveforms are different, the spectra of both detected waveforms have similar broad bandwidths covered by the spectrum of the input signal and have peak frequencies of approximately 500 kHz. Furthermore, the FOS spectrum maintains all the frequency information, i.e., it is a non-resonant sensor. Based on the spectrum, it is also clear that the noise level obtained by the FOS is 5 dB higher than that obtained by the PZT sensor. In other words, the sensitivity of the FOS is only 5 dB lower than that of the PZT sensor, which is a very high sensitivity for high-frequency ultrasonic signals relative to other FOSs. We believe that the above results and analyses are sufficient to demonstrate that our FOS can detect real AE signals generated by transverse cracks, which also have small amplitude, and broad bandwidth.

Strain applied in the AE detection experiment

The Kaiser Effect is an important and unique phenomenon in AE detections as a result of the physical nature of AE because AE signals are produced when the loaded strain exceeds the previous maximal level [90]. To verify the Kaiser Effect, the load of the tensile testing machine used in the AE detection experiment had continuous triangle shapes. When the load from the tensile testing machine was generated, both the AE hits and strain information were collected. The total duration of this experiment was 385 s, ending when the CFRP laminate was broken.

The thresholds of AE detection used in this experiment were set as 51 dB and 48 dB for the FOS and PZT sensor, respectively. These thresholds were determined when no background noise was detected for one minute when the CFRP laminate was placed in the static experimental environment. The 3-dB higher threshold for FOS can be explained by the higher noise level in FOS, as explained in former section.
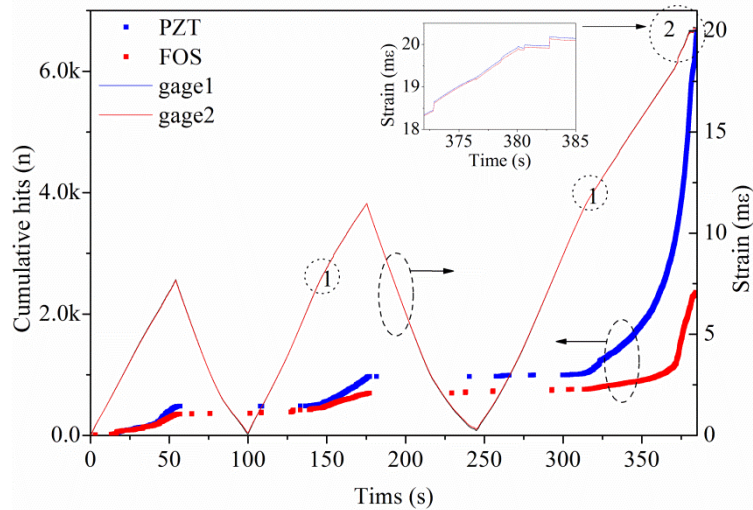
Figure 4.12. Strain curves and original cumulative hits detected by the PZT sensor and FOS with time as the abscissa. Inset shows the enlarged zigzag area at the end of strain curve.

Figure 4.12 shows the original collected data, including the strains recorded by the two strain gages and cumulative AE hits detected by the FOS and PZT sensor. The almost-overlapping strain curves indicate the absence of bending or twisting during the tensile test. In the strain curve, two areas are important, marked as black dot circle 1 and black dot circle 2 in Figure 4.12. The slope of the strain curve on the left side of area 1 is slightly higher than that on the right side, the reason of which will be explained in the following analysis. In the area 2, the increase of the strain curve is not smooth anymore; many zigzags are observed, as amplifier in the inset of Figure 4.12. The reason of these zigzags will also be explained in the following analysis.

Data processing for noise reduction

By analyzing the energy of the original detected hits in Figure 4.12, we found that many of the AE hits detected by the PZT sensor have 0 energy, derived from the EMI from the motor of the MTM. When the real AE signal exceeded the threshold set in the AE-DAQ1, both the AE signals and the following EMI signals were recorded, which caused the recorded number of AE hits to exceed the number of detected waves. To enable a meaningful comparison between the FOS and PZT sensor, the signals with 0 energy from both sensors were removed. Figure 4.13 shows the cumulative hits without the hits of 0 energy.

65
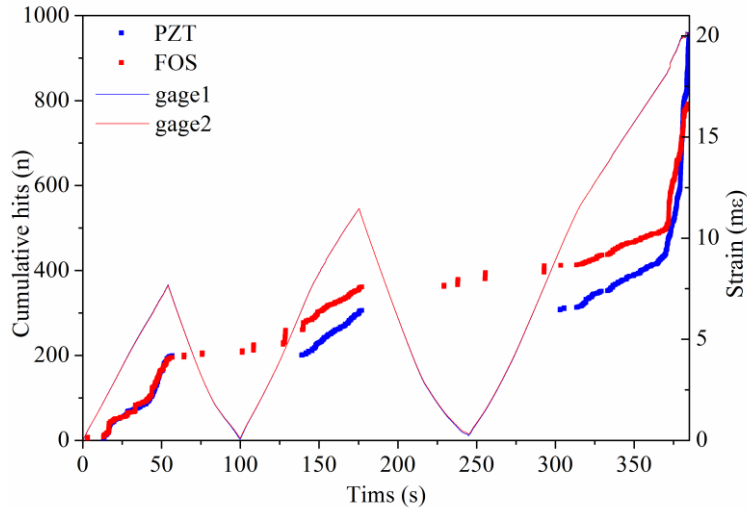
Figure 4.13. Cumulative hits obtained by removing the hits with 0 energy.

As noted in Figure 4.13, several AE hits detected by FOS were observed when the strain did not exceed the previous stages. By analyzing the signals in these ranges, we found that the recorded hits resulted from small vibrations of the PS-FBG when the tensile test was performed. Because the grating area was suspended in midair, weak airflow or machine vibration will trigger recorded AE hits. Although the FOS with a cantilever structure was immune to quasi-static strain, it was still sensitive to low-frequency vibration, which was another major difference between the FOS and PZT sensor. In this study, we focused on the AE signals; thus, we eliminated these signals manually.
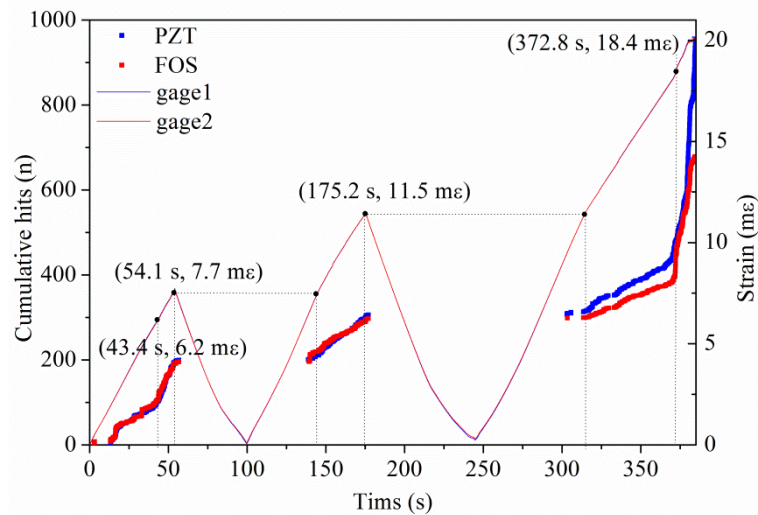
Figure 4.14. Cumulative hits without noise obtained by the PZT sensor and FOS showing the Kaiser Effect and different damage types.

After this two-step data processing, the cumulative hits without the influence of EMI in the PZT sensor and low-frequency vibration in the FOS are shown in Figure 4.14. These two curves coincide very well. The numbers of AE hits detected by the

FOS and PZT sensor were 678 and 954, respectively. The difference was caused by the lower sensitivity of FOS relative to the PZT sensor, but the similarity of these results is better than that for any previous reported results.

Cumulative hits with the Kaiser Effect

The data in Figure 4.14 also clearly display the Kaiser Effect. The coordinates of the maximal strains in the two triangles of the curves were (54.1 s, 7.7 mε) and (175.2 s, 11.5 mε). Obviously, the AE hits detected in the second triangle of the strain curve occurred only when the strain first exceeded the former maximal level of 7.7 mε. Likewise, the AE hits detected in the third triangle of the strain curve mainly occurred when the strain curve exceeded the former maximal level of 11.5 mε. However, a little Felicity Effect was also shown, which will discussed more clearly in the section 4.4.

Furthermore, the cumulative hits with the Kaiser Effect explain the different slopes of the strain curve on both sides of area 1 in Figure 4.12. When the strain was applied without exceeding the previous level, the absence of a detected AE signal means that new damage did not occur. Thus, the slope of this curve was linear. After the strain exceeded the previous level, AE signals were detected. Thus, new damages occurred and released certain level of the load from the tensile testing machine, which caused the lower slope of the strain curve in the detected AE area.

Distinguishing damage types in the CFRP laminate

In Figure 4.14, the curves of the cumulative hits exhibit two knee points with coordinates of (43.4 s, 6.2 mε) and (372.8 s, 18.4 mε). These two knee points separate the curves into three parts according to the different strains: 1) below 6.2 mε; 2) from 6.2 mε to 18.4 mε, and 3) above 18.4 mε. These three sections may correspond to different types of damages in the CFRP laminate under different strain levels. We believe that the AE hits in part 1 were caused by friction between the tabs and CFRP laminates or small initiations of not-yet-fully developed transverse cracks, the AE hits in part 2 were mainly caused by transverse cracks, and the AE hits in part 3 were mainly caused by fiber breaking when the transverse cracks were almost saturated. These speculations will be confirmed in the following discussions.
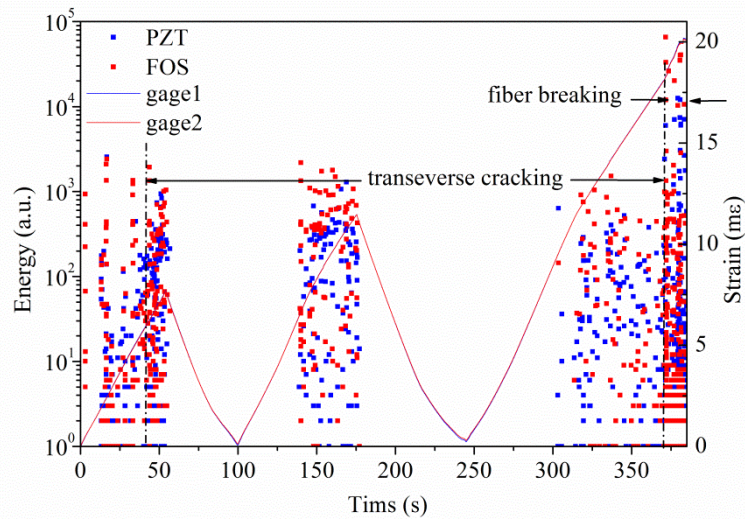
Figure 4.15. Density and energy distribution showing two damage types:
transverse cracks and fiber breaking.

Figure 4.15 shows the energy distributions of the AE hits. This energy distribution can also be used to identify different types of damage in CFRP laminates. First, the density of the AE hits reflects the health status of the CFRP laminates. The AE hits distributed from 43 s to 54 s are obviously denser than those from 0 s to 43 s, indicating that obvious transverse cracks began at 43 s. The AE hits distributed from 370 s to 385 s are evidently denser than those from 330 s to 370 s, indicating that the fiber breaking began at 370 s. Furthermore, before 370 s, the energy distributes under 2×10^3. However, the energy of the AE hits after 370 s has a much wider distribution, reaching 6.6×10^5. These findings can be explained by the much higher energy of fiber breaking than transverse cracks, which also can be used to distinguish the different types of damage in CFRP laminates.

The different damage separation also can partially be demonstrated in the area 2 of Figure 4.12 or the amplified strain curve in the inset of Figure 4.12. Due to the large energy of fiber breaking, the strain curve is not smooth.

Results obtained by analysis based on amplitude

For further proof of the correctness of our data process based on the method of removing the AE hits with 0 energy and our previous analysis of the Kaiser Effect and damage type in CFRP laminates, we performed the data processing from another aspect. Figure 4.16 shows the cumulative hits with amplitudes higher than 63 dB. These curves of the cumulative hits obtained based on the analysis of the amplitude are very similar to the curves obtained based on the analysis of the energy. In Figure 4.16, the total number of AE hits for the FOS and PZT sensor are 657 and 971, respectively. Furthermore, the Kaiser Effect and two types of damage in CFRP laminates shown in Figure 4.14 and Figure 4.15 are also clearly observed in Figure 4.16.
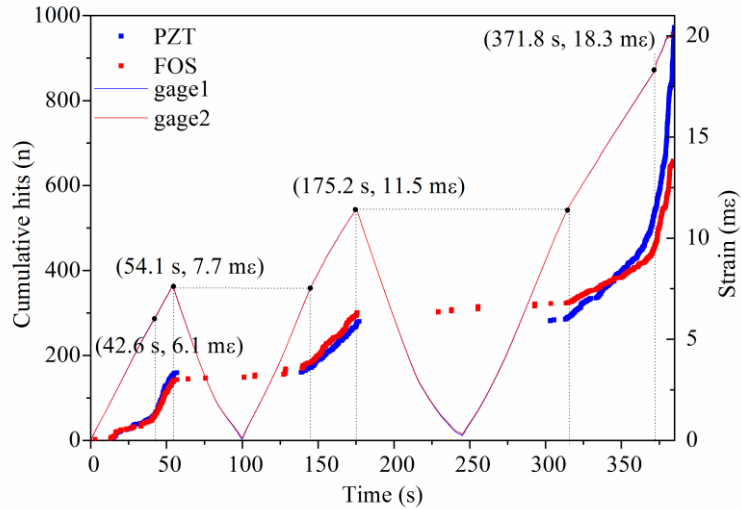
Figure 4.16. Cumulative hits obtained by analysis based on amplitude.

Confirmation of the damage types in CFRP laminates

To verify the different types of damage described above, one additional specimen was linearly stretched to the low strain level of 8 mε. In this case, we observed the edge of this CFRP laminate using a microscope. The transverse cracks were successfully observed, as shown in Figure 4.17(a). Figure 4.17(b) was taken when the first CFRP laminate was damaged, clearly revealing the fiber breaking. According to these observations, we confirmed that the two damage types in CFRP laminates, i.e., transverse crack and fiber breaking, appeared at different strain levels.
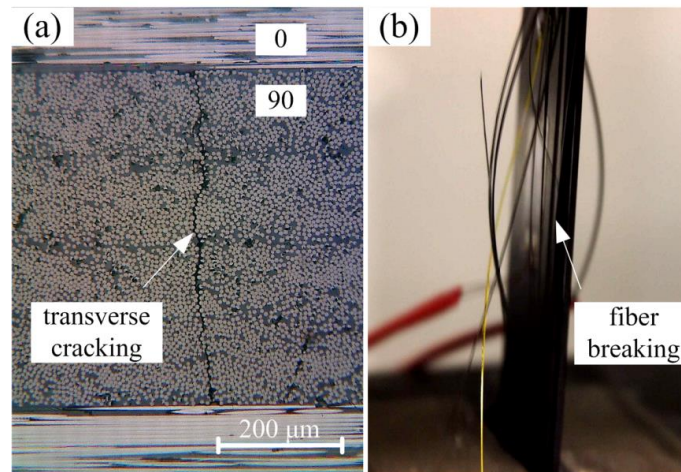
Figure 4.17. Confirmation of the damage types in CFRP laminates: (a) transverse crack, and (b) fiber breaking.

Waveform analysis

We selected several typical waveforms detected in this experiment, as shown in Figure 4.18. In Figure 4.18, the waveforms in the left part were detected by PZT

69

sensor, while the waveforms in right part were detected by our PS-FBG balanced sensing system.
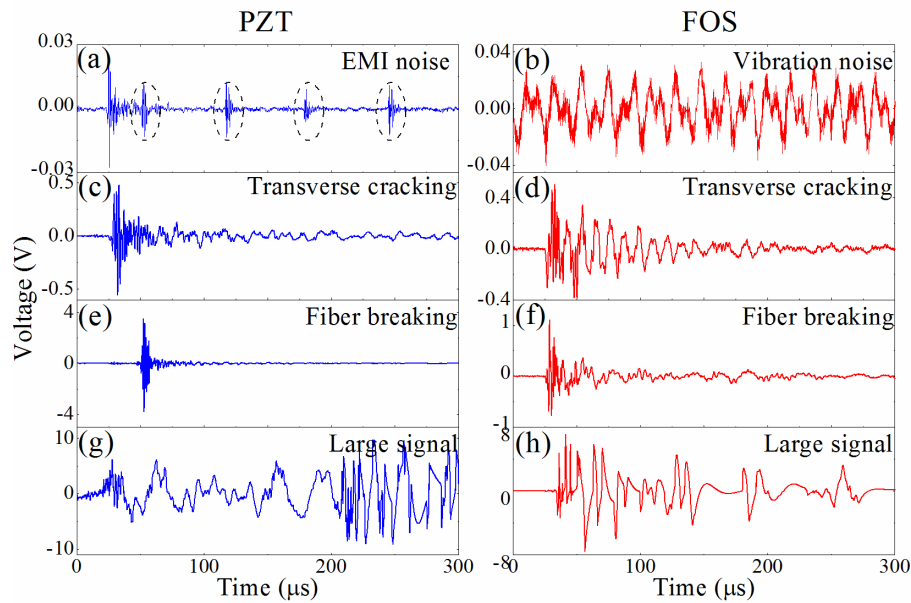
Figure 4.18. Typical waveforms detected by both PZT sensor and PS-FBG sensor in tensile test.
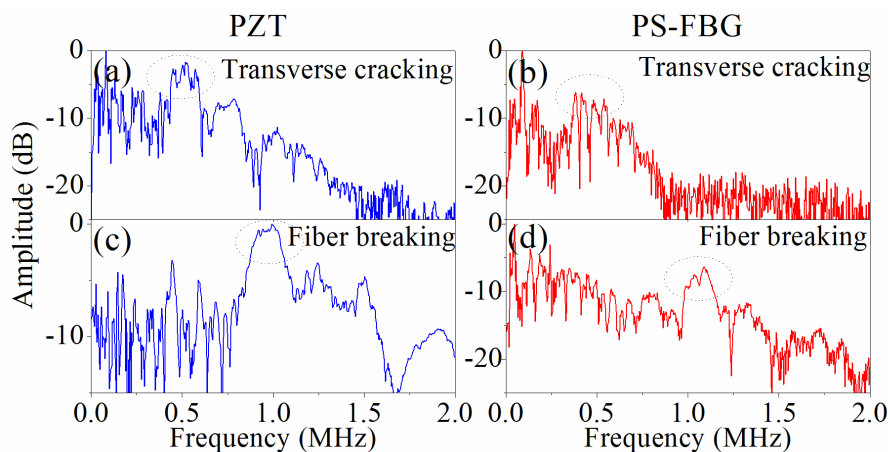
Figure 4.19. Spectra of the detected waveforms of transverse crack and fiber breaking.

Figure 4.18(a) and (b) are typical noises. In PZT sensors, the dominant noise was caused by EMI, as shown by the black dot circles in Figure 4.18(a). When real AE signal exceeded the threshold set in the DAQ system, both the AE signals and the following EMI signals were recorded, which caused the recorded number of AE hits more than the number of detected waves. On the other hand, FOS has inherent advantage of EMI immunity. The noise problem in PS-FBG, as shown in Figure 4.18(b), is its sensitivity to low frequency vibration, which also bothers quantitative analysis.

We guess Figure 4.18(c) and (d) are the detected waveforms of transverse cracks by both sensors. There are three reasons. Firstly, these two signals were obtained in

relative low strain level, when fiber breaking did not happen. Secondly, the amplitude of this signals are low, although it is higher than the amplitude of noise. Thirdly, after analyzing the corresponding spectra of these signals, we find that there exists a peak area around 500 kHz as shown in Figure 4.19(a) and (b), though the spectra are wide. Comparing the waveforms detected by PS-FBG and PZT sensor, we also noticed that the waveforms detected by PS-FBG contain more low frequency components than that of PZT sensor.

Figure 4.18(e) and (f) are believed as the waveforms of fiber breakings, which show different characteristics in contrast to that of transverse cracks. Firstly, the appearing time of the signals is close to the end of the tensile test when strain level is higher than the strain level of transverse crack. Secondly, the amplitudes of the fiber breaking signals are higher than that of transverse crack signals. Thirdly, the peak frequency shown in the spectra as Figure 4.19(c) and (d) appear much higher than 500 kHz.

The signals in Figure 4.18(g) and (h) are both obtained at time of 380 s with very small time difference. We think these signals are produced by the same signal source because of the very large amplitude and unique waveforms. These kinds of signals only appeared several times. Therefore, these signals were produced by some large fiber breakings, such as fiber bundle breaking, or produced by disbonding of aluminum tabs.

4.3.3 *Conclusions*

In this study, we applied improved PS-FBG balanced sensing system to the practical AE detection of CFRP laminates in tensile test, and analyzed the experimental results, including the Kaiser Effect, and separation of damage types.

An actual AE detection experiment was then performed by tensile test after calibration of the PS-FBG balanced sensing system. Applying simple data processing for the noise reduction of EMI in the PZT sensor and vibration in FOS based on energy analysis or amplitude analysis, the cumulative hits detected by both sensors almost coincided, providing very promising results for the use of our FOS in practical AE detection. The Kaiser Effect is demonstrated by the integral analysis of the cumulative hits and strain curves. Two different types of damage in CFRP laminates, transverse crack and fiber breaking, can be identified by analyzing the keen point in the curve of cumulative hits. Moreover, these damage types can be distinguished by the different energy distribution of the detected signals because fiber breaking generated more energy than did transverse crack. These two types of damage were proven by direct observation. Transverse crack was observed using a microscope when the applied strain on the CFRP was low. The fiber breaking was directly observed after the CFRP laminate suffered a large strain.

4.4 Application to AE Detection in Tensile Test 2

In the previous research in section 4.3, we conducted AE detection by the novel optical fiber sensor. However, the AE-DAQ1 system collects the data independently, which means the data collected from different sensors do not have solid relations. Therefore, we changed the DAQ system to AE-DAQ2. Once an AE signal gets the threshold in one channel of the AE-DAQ2, all the other channels will collect the data simultaneously. Due to these properties, we can relate signals in four channels to have a deep discussion. However, the AE-DAQ2 has its own disadvantages. Firstly, the noise level in this system is much higher than AE-DAQ1, leading to some different results. Secondly, the maximal output voltage in this system is only 5V, half of the AE-DAQ1. Thirdly, AE-DAQ1 can provide many useful analytical statistic data, including energy, amplitude, frequency, duration, counts, *etc*. AE-DAQ2 only provides the amplitude information, leading to limited analysis based on statistic viewpoint. The other difference of the experiment in section 4.4 is the specimen we used. In this part, we tried two different types of CFRP laminates (angle-ply and cross-ply), and compared their different waveforms. Therefore, we focus on the discussion on the waveform and its relation to different damage types in the following experiment.

4.4.1 *Experimental setup*

Two types of CFRP laminates were used in this research. The angle-ply CFRP laminates with dimensions of $193 \times 20 \times 0.83$ (L$\times$W$\times$H) mm^3 have structure of $[\pm 45/90]_s$, called CFRP1. The cross-ply CFRP laminates with dimensions of $198 \times 21 \times 1.09$ (L$\times$W$\times$H) mm^3 have structure of $[0_2/90_2]_s$, called CFRP2. All the specimens were edge polished, and examined whether they are intact ones under the microscope before experiments. The CFRP specimens were tabbed by 1.2-mm-thick aluminum at each end of the CFRP laminates for tensile testing. They were stretched by the MTM. The tensile test for CFRP1 had a linear loading with speed of 1 mm/min. The tensile test for CFRP2 had a saw-tooth loading formed from a sequence of triangular loading/unloading steps with speed of 2 mm/min. The different loading speed is because the final damages occur easier in CFRP1.

Three N-PZT sensors were utilized to compare the performance of the PS-FBG balanced sensing system. The signals detected by the PZT sensors were amplified by Pre-Amp2s and then collected by the AE-DAQ2. In the experiment of CFRP1, the preamplifier factors for PS-FBG and PZT are 10 and 20 dB; in the experiment of CFRP2, the preamplifier factors for PS-FBG and PZT are 20 and 30 dB. These amplifier factors are not so large, because we would like observe the complete waveforms in the range of the maximum output of the preamplifier (from -5 to 5 Voltage). The higher preamplifier factors for CFRP1 results from the smaller AE signal energies in CFRP1. The thresholds used in the experiments of CFRP1 and CFRP2 are 1% and 5% respectively. The thresholds were determined when sensors

did not detect any signals when specimen was statically put in the experimental environment.

On these CFRP laminates, we glued sensors according to the arrangement shown in Figure 4.20(a) and (b). The PZT sensors were glued by a high-acoustic-impedance ultrasonic couplant. The PS-FBG was attached by applying cyanoacrylate adhesive near the grating area to create a cantilever structure, as shown in Figure 4.20(c). PZT 2 and PZT 3 were used for Lamb-wave mode discrimination and identification because they were glued on both surfaces at the same attached position. 90-mm apart from the PZT 2 and PZT 3, PZT 1 and the PS-FBG grating area were at the same position for guaranteeing the same wave arrival time. In addition to the AE sensors, two strain gages were glued on both surfaces of the CFRP laminates to monitor the strains. The strains were recorded by a data logger with 20-Hz sampling frequency. All the specimens were loaded until the final damage stages, such as the CFRP2 shown in Figure 4.20(d).
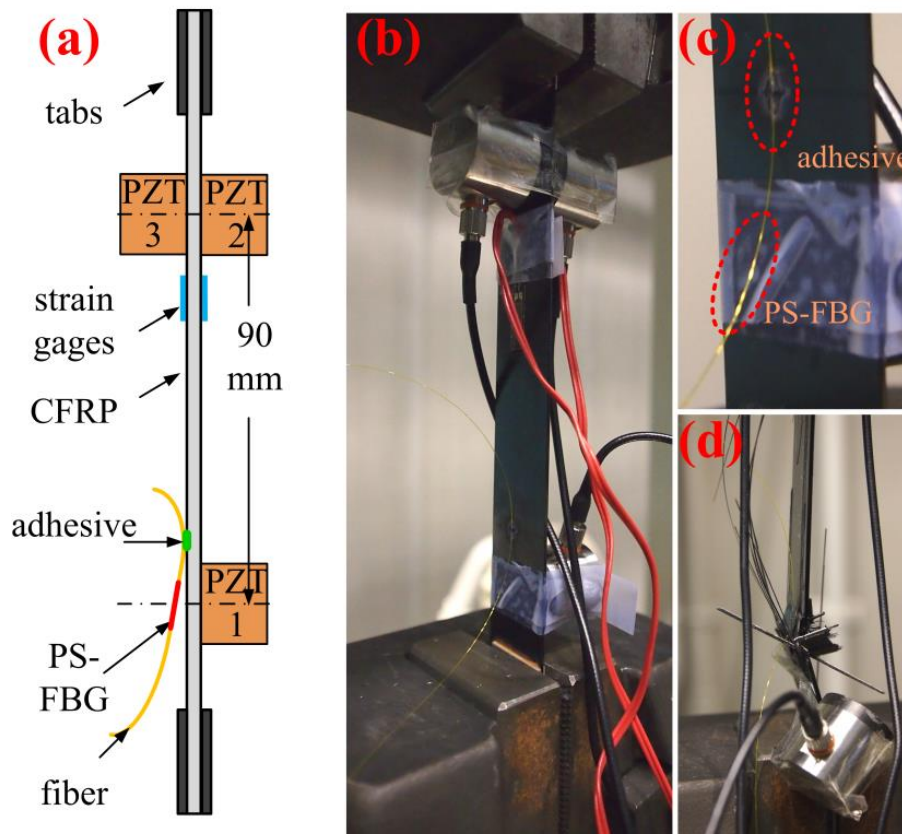
Figure 4.20. Setup of the AE tensile testing. (a) Schematic diagram of the sensor arrangement;(b) photo of the sensors and the CFRP specimen; (c) PS-FBG was glued via cantilever structure; (d) the final damage stage of CFRP2.

4.4.2 *Cumulative AE hits*

Cumulative AE hits in the [±45/90]$_s$ CFRP laminates

Figure 4.21 shows the strain on CFRP1. These three curves are very close, and show that final damage basically occurs after about 12 mε. Figure 4.22 shows the original

cumulative AE hits detected by different sensors, corresponding to different strain curves in Figure 4.21. The data from PZT 2 and PZT 3 almost coincide, because the same type PZT sensors were at the same position. However, the cumulative AE hits from PZT 1 differ to that from the PZT 2 and the PZT 3, mainly due to the different attached positions. The cumulative AE hits from the PS-FBG sensor also differ to that from the PZT 1. For example, in Figure 4.22(a) and (c), the hit number in PS-FBG is large. After seeing the waveform, we found that there are many low-frequency noises, as discussed in section 4.3. In Figure 4.22(b), the number is small, maybe it is because the cantilever structure we glued is longer than that we expected, leading to the extra attenuation of the ultrasonic wave. In order to remove the low-frequency noise, we applied a digital high-pass filter with cut-off frequency of 10 kHz to the detected AE waveforms from PS-FBG sensor. The cumulative AE hits shown in Figure 4.23 correspond to the original data in Figure 4.22(a). After the data process method, the number of the cumulative hits detected by PZT 1 and PS-FBG sensor are 187 and 203, respectively. Figure 4.24 shows the relation between the cumulative AE hits and the strain. The AE initially occurs after 30 s (3 mɛ strain), demonstrated by all the sensors. These coincided curves from PS-FBG and PZT 1 in Figure 4.23 and Figure 4.24 mean that our novel optical fiber sensor and the data process method are reliable and have high fidelity. Furthermore, because of the signal's low energy level in CFRP1, our sensor shows enough sensitivity to detect small AE signals.
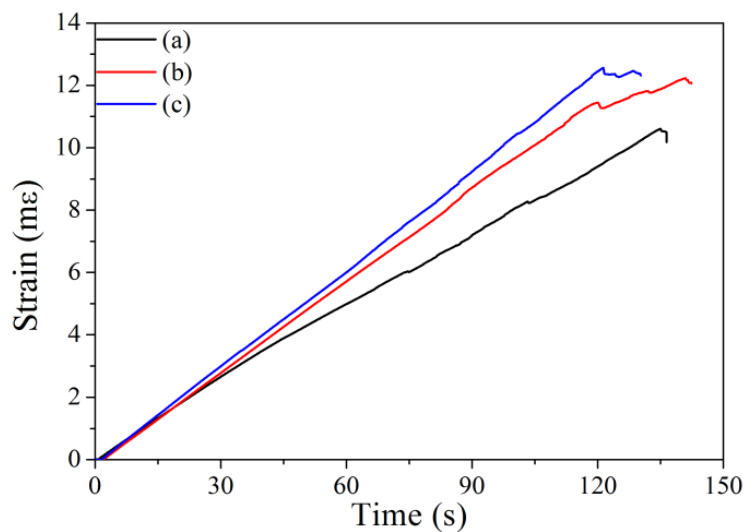
Figure 4.21. The linear strain applied to the CFRP1.
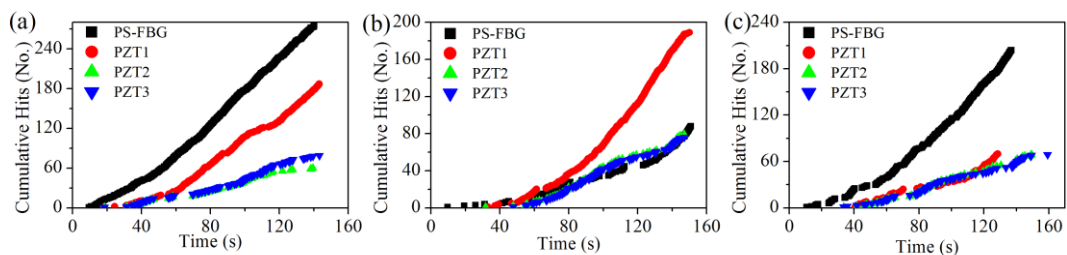
Figure 4.22. Original data of cumulative AE hits collected from PS-FBG sensor and PZT sensors.
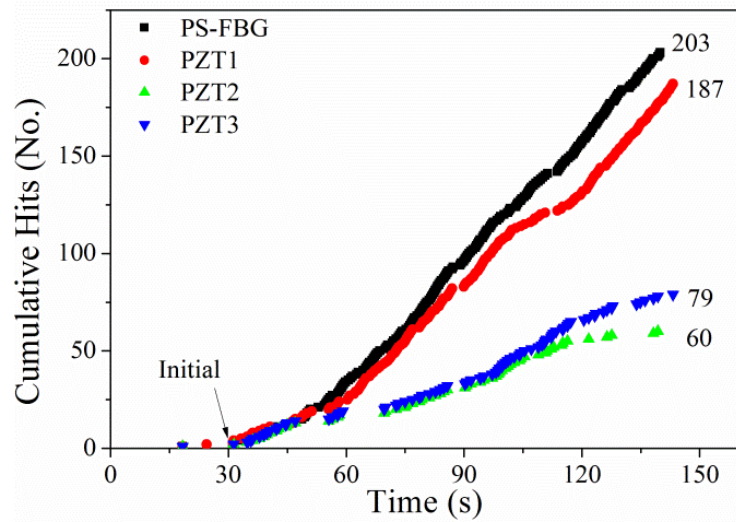
Figure 4.23. After removing the noises, the cumulative AE hits collected by the PS-FBG sensor coincides the data collected by the PZT sensors.
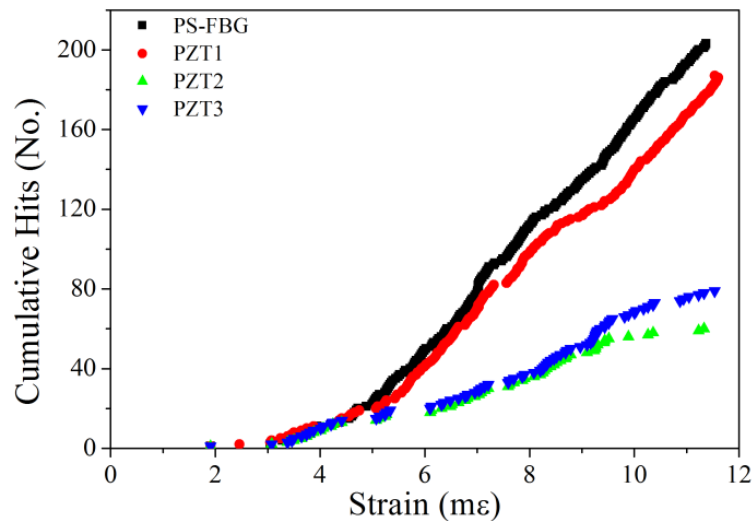
Figure 4.24. Relation between the cumulative AE hits and the strain in CFRP1.

Cumulative AE hits in the [0₂/90₂]ₛ CFRP laminates

Figure 4.25 shows a typical relation between the strain and the cumulative AE hits in the tensile test for CFRP2 detected by both traditional PZT sensor and our PS-FBG sensor. It clearly demonstrates the Kaiser Effect by both sensors, similar to the results shown in section 4.3. Furthermore, weak Felicity Effect is also seen in Figure 4.25 in the third loading period. When the loading did not exceed the former maximum strain value (10.5 mε), several AE hits were also detected from about 300 s to 335 s. The Kaiser Effect and the Felicity Effect both can be demonstrated according to the plot of the relation between the cumulative AE hits and strains, as shown in Figure 4.26. The strain curve shown in Figure 4.25 has different slopes after AE signals occur, similar to that shown in section 4.3. Furthermore, after comparing the strain in the experiment of CFRP1 and CFRP2, we found that CFRP1 much easier gets its final damage stage

in the relative low strain level (12 mε). However, CFRP2 gets its final damage stage at about 18 mε. The strain level when the finial damage occurs in the cross-ply CFRP laminate is also different to that in the experiment shown in section 4.3. In the previous experiment, after 18 mε, there still occurred many large AE signals. However, in this experiment, the cross-ply CFRP laminates fractured rapidly after about 18 mε. Thus, it does not show very clear knee point as the experimental results in section 4.3; only the cumulative AE hits from PS-FBG shows an a little increase of the curve slope at about 18 mε. The other explanation is the different noise level in these two DAQ systems. Because AE-DAQ1 can detect many small energy AE signals, the results are always different to that from AE-DAQ2.
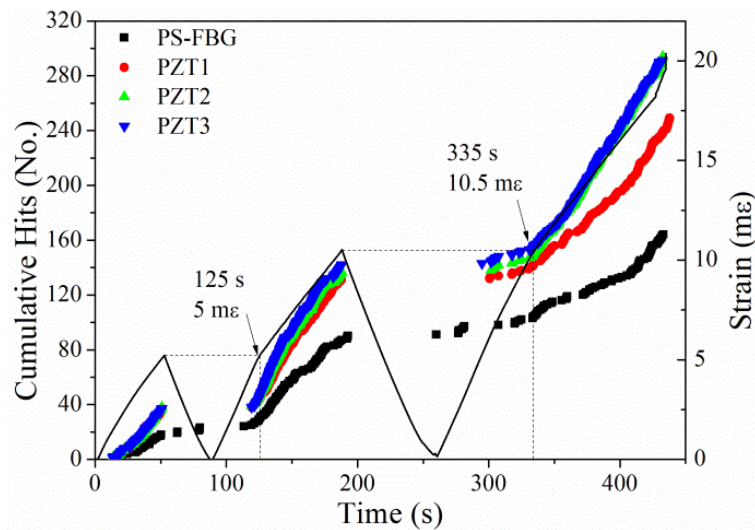
Figure 4.25. The cumulative AE hits collected by both PZT sensor and PS-FBG sensor in CFRP2 show Kaiser Effect and Felicity Effect.
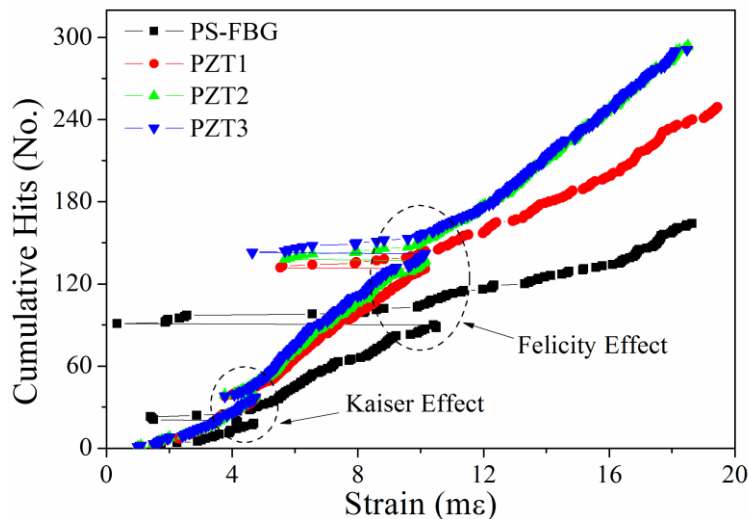
Figure 4.26. Relation between the cumulative AE hits and the strain in CFRP2.

4.4.3 *Waveforms*

Noises in sensors

The noise problems in the PS-FBG sensor and the PZT sensor are different. Figure 4.27 shows the typical noises to either sensor. The noise problem in the PS-FBG sensor and PZT are low-frequency noise and EMI noise as we discussed in section 4.3. Then, we evaluate the actual noise level in both sensors. According to the signals in Figure 4.27, the standard deviation (std) for PS-FBG sensor and PZT sensor are 0.0227 V and 0.0142 V, respectively, if we ignore the low-frequency noise and the EMI noise. Although the noise level in the PS-FBG is a little higher than that in the traditional PZT sensor, PS-FBG is clearly insensitive to EMI noise, showing large potential of AE detection in environment with large EMI noises.
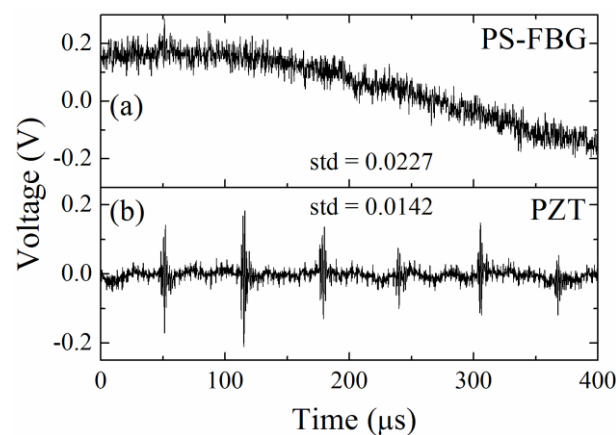
Figure 4.27. Noise problems in PS-FBG sensor and PZT sensor are low-frequency noise and EMI noise, respectively.

Typical AE waveforms

The detected AE signals can be roughly divided into 6 types. The signal type is determined according to the waveforms detected by PZT 2 and PZT 3. Figure 4.28 shows the typical waveforms from experiment of CFRP1.

In CFRP1, type 1 signal contains S mode in the front part and A mode in the following part. S mode with relative high frequency has the same phase, while A mode with relative low frequency has opposite phase in PZT 2 and PZT 3. Type 2 signal has obvious S mode with same phase. Its S mode contains narrow-bandwidth and relative high frequency. Type 2 signal almost does not have low frequency vibrations. The waveforms of type 3 and type 4 signals are more complex. The front part of the waveform has higher frequency components then the following part of the waveform. The phases of the waveforms in type 3 signals coincide better than that in type 4 signals. It means that type 3 signal contains mainly S mode, and type 4 signal contains large part of A mode. Type 5 signal has very unique shape, showing single peak with very low amplitude. Type 6 signal has very large amplitude. Once it

triggers the AE threshold, the following parts of the waveforms exceed the maximum output voltage of the preamplifier.
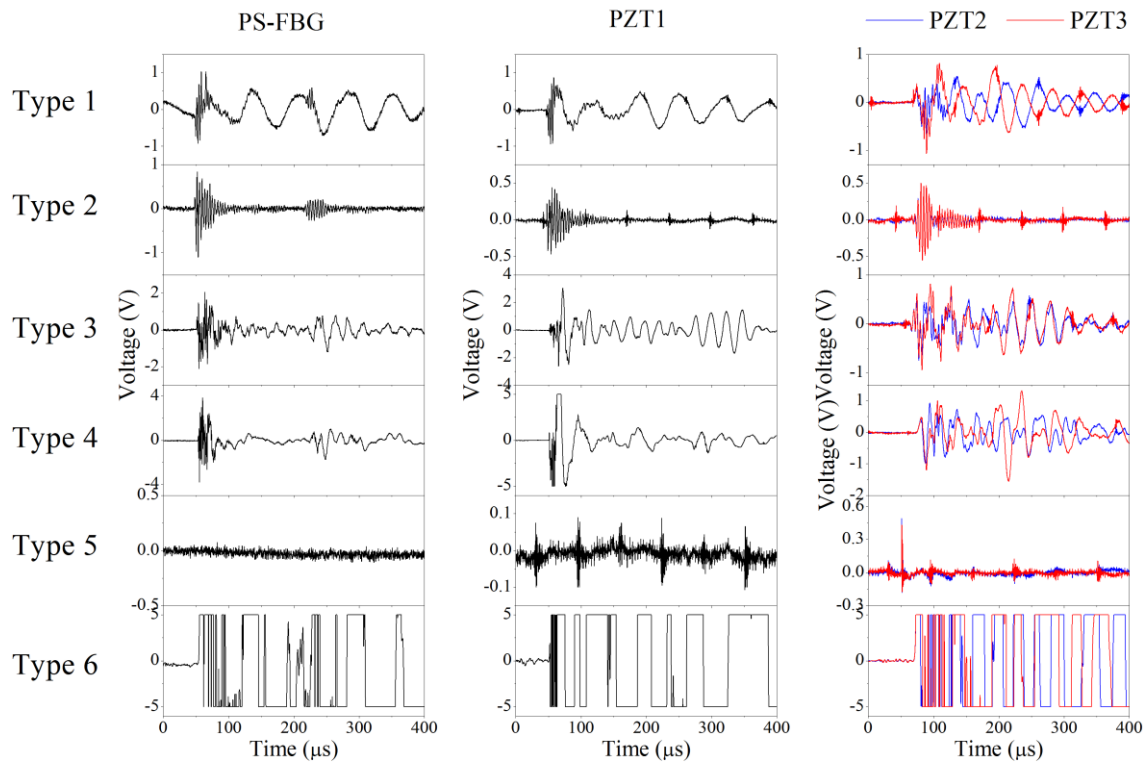
Figure 4.28. Six types of typical waveforms obtained from CFRP1.

PS-FBG's responses to different types of signals

PS-FBG has different responses to different types of the signals. In type 1, the waveform from PS-FBG also contains the high-frequency S mode in the front part and low-frequency A mode in the following part. Furthermore, the A mode has opposite phase to that in the PZT 1. In type 2, the waveforms collected by the PS-FBG and PZT 1 are very similar. In their corresponding spectra shown in Figure 4.29, only one peak at about 250 kHz exists. In type 3, more frequency information is detected by both PS-FBG and PZT, compared to the waveform of type 2 signal. However, as shown in Figure 4.29, the PS-FBG shows lower responses to signal frequency component under 50 kHz compared to PZT sensor, which can be explained by the cantilever structure used in this experiment. Because the fiber suspends in the midair, the low frequency vibration does not effectively affect the Bragg wavelength shift. In type 4, the signals detected by both sensors have much broader bandwidth than the other types of the signals. For example, the PS-FBG detected the signal frequency components as high as about 1.5 MHz. It means that this fiber sensor detects all the main frequency information and has broad bandwidth. In type 5, both PS-FBG and PZT 1 do not detect the signal, because of the high attenuation of the CFRP laminate to high-frequency AE signals and the low amplitude of type 5 signals. In type 6, both

PS-FBG and PZT sensor detect the signal, whose amplitudes are also over the maximum output voltage of the preamplifier.
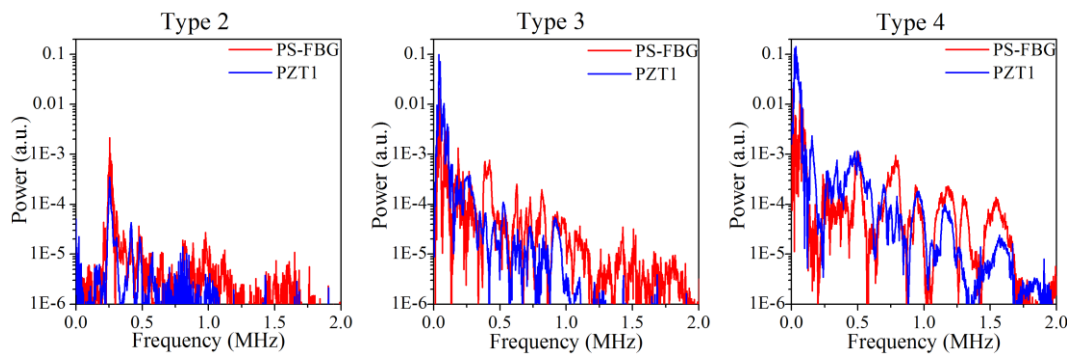
Figure 4.29. Corresponding spectra of type 2, type 3 and type 4 signals.

Relation between the signal type and different CFRPs.

Different types of the AE signals not only have different waveforms but also have different relations to the strain levels in different CFRP laminates.

Type 1 and type 2 signals are only observed in CFRP1. Type 3 and type 4 signals are observed in both CFRP1 and CFRP2. Especially, type 3 is the main signal type in CFRP2. Type 5 and type 6 signals are also observed in both CFRP1 and CFRP2, but have very small numbers. Type 5 signals have relative random distribution in both CFRP laminates. However, type 6 signals are only observed near to the final damage stage of the CFRP laminate. In the specimen 1 of CFRP1, we only detected one type 6 signal; however, in the specimen of the CFRP2, we detected six type 6 signals.
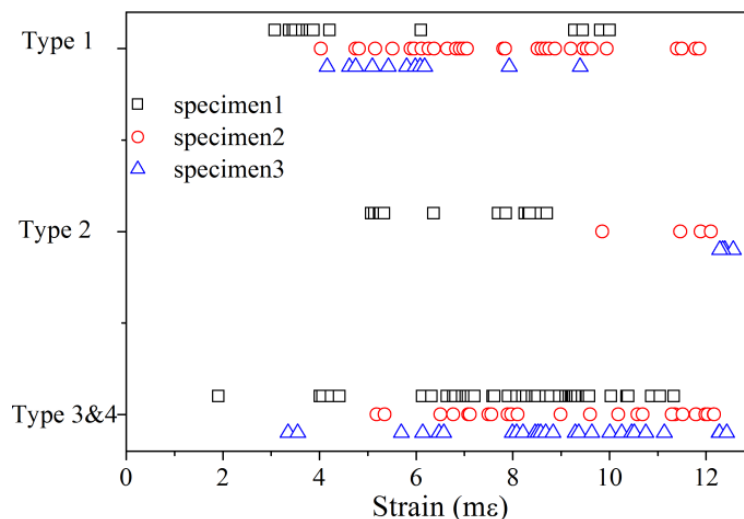
Figure 4.30. Different types of AE signals to different strain level in CFRP1.

We also observed that type 1 to 4 signals occur at different strain level in CFRP1, as shown in Figure 4.30 (we does not separate type 3 and type 4 signals herein because their waveforms do not have so obvious characteristics as type 1 and type 2

79

signals). The number of type 3 and type 4 signals are the largest among all signal types. Type 1 signals are more concentrated in the low strain level; however type 3 and type 4 are more concentrated in the high strain level. In these three specimens, type 2 signals have the smallest number, and have very different distributions. However, it always occurs after the appearance of type 1 and type 3 signals.

Because type 3 and type 4 signals are very similar, they are not easy to be identified or discriminated clearly. We use a mathematical evaluation to research them. The waveforms from PZT 2 and PZT 3 are subtracted to get their differences. Then the standard deviation of their differences is divided by the waveform amplitude. The results are shown as the open dots in Figure 4.31. The higher the value is, the more differences the waveforms from PZT 2 and PZT 3 have. A number of dots are distributed under 0.1. In this range, there are many noise signals, type 2 or type 3 signals. However, CFRP1 contains more dots which has higher waveform mismatch (higher than 0.1). It means that some waveforms detected from CFRP1 have larger A mode components. Especially in the range after 8 mε, the waveforms with large mismatch appear frequently. For example, there are 121 waveforms with mismatch level higher than 0.1, and 63% of them are concentrated in the range after 8 mε in CFRP1. However, in the CFRP2, there are only 46 waveforms with mismatch level higher than 0.1.
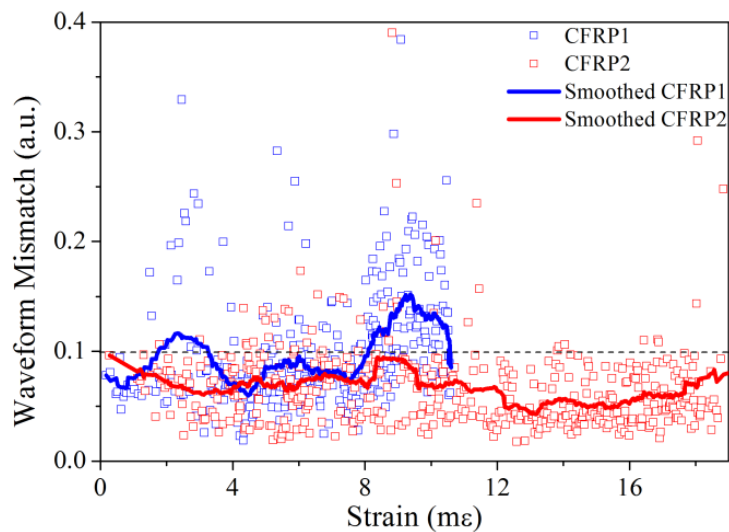
Figure 4.31. Discrimination between type 3 and type 4 signals according to the level of waveform mismatch.

In order to reveal the phenomenon clearer, we use adjacent-averaging method with window size of 20 to smooth the data, and show the results as the lines in Figure 4.31. In CFRP1, when the strain is lower than 4 mε, the waveforms in PZT 2 and PZT 3 have relative large differences, because they belong to type 1 signals which have opposite A mode in the waveforms as shown in Figure 4.28. From about 4 to 8 mε, the curve shows that the detected waveforms are very close in PZT 2 and PZT 3. It indicates that type 2 and type 3 are the main signal type in this area. However, after 8 mε, the waveforms become more and more different, which means type 4 signals

appears more frequently, and the waveform difference becomes severer. In other words, type 4 signal are more concentrated in the high strain level. However, in the CFRP2, the phenomenon is different. Basically, the curve of CFRP2 is relative flat and lower than 0.1. It means that type 3 is the main signal type in CFRP2.

4.4.4 *Damage type discrimination*

Damages in the CFRP laminates

After the tensile test, we observed the specimens via microscope. Figure 4.32 shows several typical damages in (a) CFRP1 and (b) CFRP2. One typical damage type in CFRP1 is the matrix crack. They appear in the 90 degree layer (transverse crack 1) and in the 45 or -45 degree layer (transverse crack 2). The other observed matrix crack is close to the intra-layer of 90 degree prepregs and is parallel to the loading direction. The delaminations in CFRP1 are long and large, it can both occur between layers of 90 and 45 or between layers of 45 and -45. On the other hand, the typical damages in CFRP2 are different. Before the severe fiber breaking shown in Figure 4.20(d), many transverse cracks are observed; and there are no long and large delaminations.
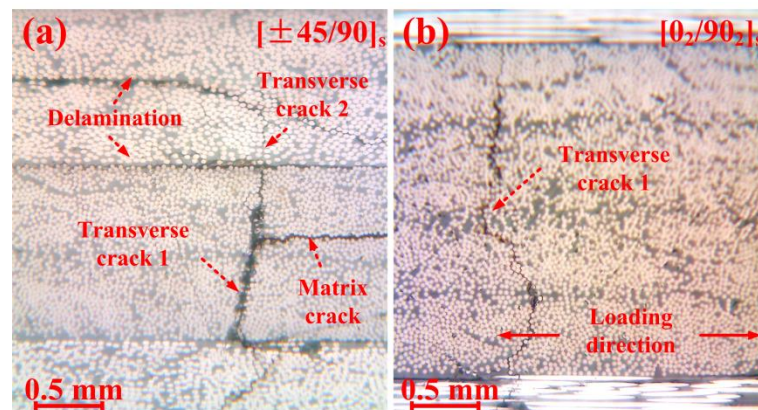
Figure 4.32. Typical micro damages of CFRP laminates observed via the microscope. (a) $[\pm 45/90]_s$ CFRP laminate shows matrix cracks and delaminations. (b) $[0_2/90_2]_s$ CFRP laminate shows many transverse cracks.

Damage discrimination on AE signals

Different damages in CFRP laminates will trigger different waveforms. According to modal AE viewpoints in references [12, 16, 91, 92], transverse cracks lead to in-plane strain, and delamination lead to out-of-plane strain in ideal conditions. Therefore, the wave generated by the transverse crack mainly contains S mode, and the wave generated by the delamination mainly contains A mode. Considering that the type 3 signal has main S mode and its large amount number in CFRP2, it can correspond to transverse crack. Considering that the type 4 signal with A mode component and its main appearance at the high strain level of CFRP1, it can correspond to delamination. Furthermore, the amplitude and the frequency characteristics also prove this

discrimination. Our experimental results show that the wave from delamination contains higher amplitude and higher frequency components than that from transverse crack (Figure 4.28 and Figure 4.29), fitting other researchers results [5, 93, 94]. Because type 1 and type 2 signals were only observed in CFRP1, they should correspond to some unique damage types in CFRP1. Transverse cracks at 45 degree or -45 degree layer may generate A mode with opposite phase as type 1 signals. Matrix cracks at the middle of the CFRP1 may generate the type 2 signals with simple S mode. As for type 5 signal, due to its unique waveform, very small amplitude and random distribution in both CFRP laminates, it can correspond to frictions of tabs in the tensile test. Type 6 signal clearly corresponds to large damage, for example the final damage in CFRP1 or bundle fiber breaking in CFRP2. Figure 4.33 shows the schematic of micro damages in CFRP1 and their corresponding signal types. The properties of the AE signals and their perhaps corresponding damage types in the CFRP laminates are also concluded in the Table 4. Although these damage discriminations need to be further proved, these experimental results and analyses show that the PS-FBG has potential to detect AE signals from all the damage types, and contain almost all the useful information in the waveform.
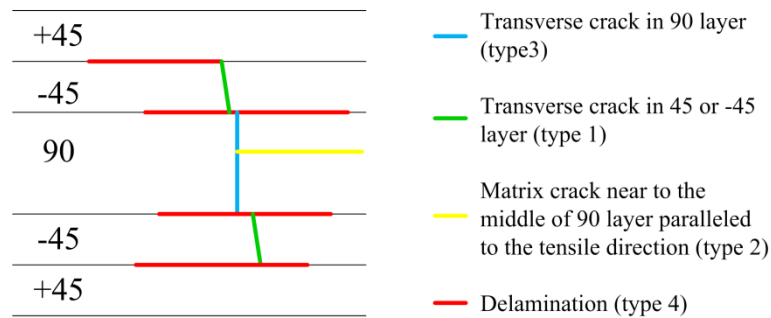
Figure 4.33. Micro damages in angle-ply CFRP laminates and their corresponding signal types.

Table 4. Properties of the AE signals and their corresponding damages.

Types	Waveform	Number	Amplitude	Frequency	Specimen	Strain level	Damage
1	A mode and S mode with low frequency				CFRP1	relative low	transverse crack in 45
2	S mode with high frequency	relative few		single peak	CFRP1	after type 1 and 3	matrix crack in 90
3	main S mode	large number*¹		relative low	CFRP1&2	medium	transverse crack in 90
4	S mode and A mode mixed		large	high (1.5 MHz)	CFRP1	higher	delamination
5	single peak	few	small	high	CFRP1&2	random	tab friction
6	unique	very few	ultra-large		CFRP1&2	final	finial damages

*¹ Especially in CFRP2

4.4.5 *Conclusions*

In this study, we applied PS-FBG balanced sensor to the AE detection of CFRP laminates in tensile test, and compared the results from this optical fiber sensor to that from traditional PZT sensor. Actual AE detection experiments of CFRP laminates with two different structures were then conducted via tensile testing. Applying simple data processing, the cumulative AE hits detected by both sensors almost coincided. The Kaiser Effect and the Felicity Effect were both demonstrated in the experiment. Besides demonstration of the sensor performance, Kaiser Effect and Felicity Effect, six different types of signals were obtained and discussed in details. By consideration of their relations to strain level and their properties, these different types of signals can correspond to observed different damages in different CFRP laminates, including transverse cracks, delaminations and so on. Therefore, this novel optical fiber sensor can detect the major damage types in the CFRP laminates, and contain almost all the frequency components in the signals.

4.5 Application to AE detection in Three Point Bending Test

We have gotten attracting results from the experiment in the last two sections. However, the tensile experiment of composites for AE detection by the novel PS-FBG balanced sensing system is far from enough. Because, in the above mentioned experiments, many data were collected, leading to the difficulty of relations of the detected waveforms and actual damages. Owing to the same reason, the position identification ability of the sensing system which is an important application of AE detection cannot be demonstrated as well. Thus, targeted signal analysis to a certain damage type is necessary.

In this research, we applied PS-FBG balanced sensing system in transverse crack AE detection in three point bending test. In the three point bending test, the number of transverse cracks was fewer than that in tensile test; thus the transverse cracks corresponded to detected signals more precisely. As a result, the waveforms and their corresponding CWT results can also be discussed deeply and comprehensively. Moreover, we demonstrated this novel optical system has position identification ability after simple data process.

4.5.1 *Experimental setup*

Figure 4.34 shows the setup for the AE detection of three point bending test. Figure 4.35 is the photo of this experimental setup. The CFRP laminates with dimensions of $176 \times 19 \times 0.575$ (L$\times$W$\times$H) mm^3 ([90/0]$_s$) were used in this research. The edges of these specimens were carefully polished for observing the transverse cracks under the microscope later. The CFRP laminate was settled on two 48-mm-separated support bars. The push bar pushed the CFRP laminate at the center with speed of 2 mm/min via the MTM. All the bars were covered by Polytetrafluoroethylene tape for decreasing frictions, which may be mistook as AE signals by detection system. A strain gage with length of 2 mm was glued beneath the center of the CFRP laminate,

and recorded by the data logger for monitoring the applied strain. On the left side of the CFRP laminate, two N-PZT sensors with diameter of 20 mm were glued on both surfaces of the CFRP laminate to discriminate the components in the Lamb wave for further deducing the property of the damage types in the CFRP laminate. On the right side, PS-FBG sensor and a third N-PZT sensor were glued on top surface and bottom surface of the CFRP laminate, respectively, for verifying the ability of position identification of the novel optical sensing system. All the sensors were glued by high-acoustic-impendence ultrasonic couplant and fixed by tape 60-mm away from the center of the CFRP laminate.
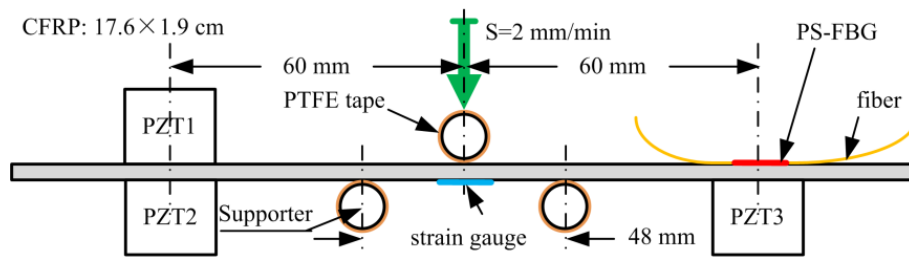
Figure 4.34. Setup for three point bending test.
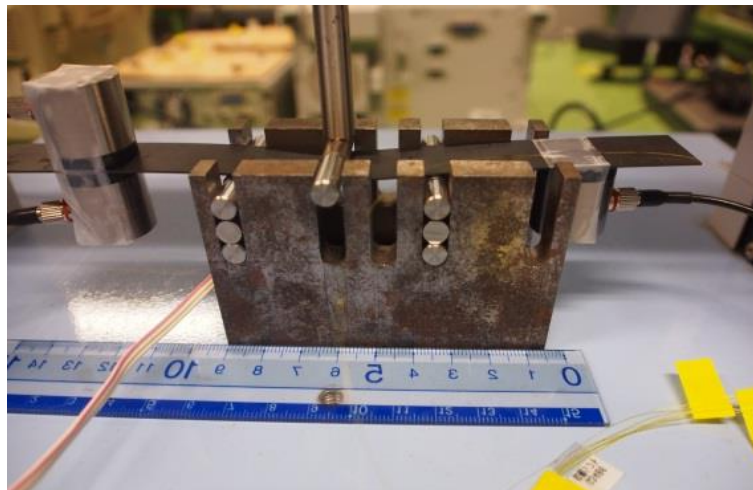
Figure 4.35. Photo of the three point bending test

The PS-FBG balanced sensing system used in this experiment was the same as that one used in the previous experiment. However, the output power of TLS was increased to 6 dBm for better SNR of the detected waveforms because the noise in the AE-DAQ2 is larger. The generated AE signals were detected by PS-FBG balanced sensing system and PZT sensor, and then collected by AE-DAQ2. Due to the small energies of the AE signals generated by transverse cracks, Pre-Amp2 with amplification factor of 30 dB were connected to the PZT sensors, while same preamplifier with amplification factor of 20 dB was connected to the PS-FBG balanced sensing system. Because of the large low frequency vibration in the three point bending test, high-pass filter with cut-off frequency of 50 kHz were also set in the preamplifier. The threshold in every sensor channel was set to 0.25 V. Once an

AE signal triggers one of the four sensor channels, other sensor channels will also recorded the measured waveforms simultaneously.

4.5.2   *Transverse crack AE signals*

AE signals and strain

In one of the three point bending test of the CFRP laminate, four-channel AE data were collected from PZT1, PZT2, PZT3 and PS-FBG, respectively. Figure 4.36 shows the relation between strain and AE signals. In Figure 4.36, the strain from 0 s to 200 s is omitted, because the strain was linear and no AE signals were detected in this range. The first AE signal occurred when the strain was 12.17 mε, which was about twice bigger than that in tensile test reported in our previous experiment. 12.17 mε was the strain we measured on the bottom surface of the CFRP laminate, where the strain had the highest value because of the un-equivalent strain in cross-section of the CFRP laminate. Thus, the actual strain able to trigger the occurrence of the transverse cracks will be lower.
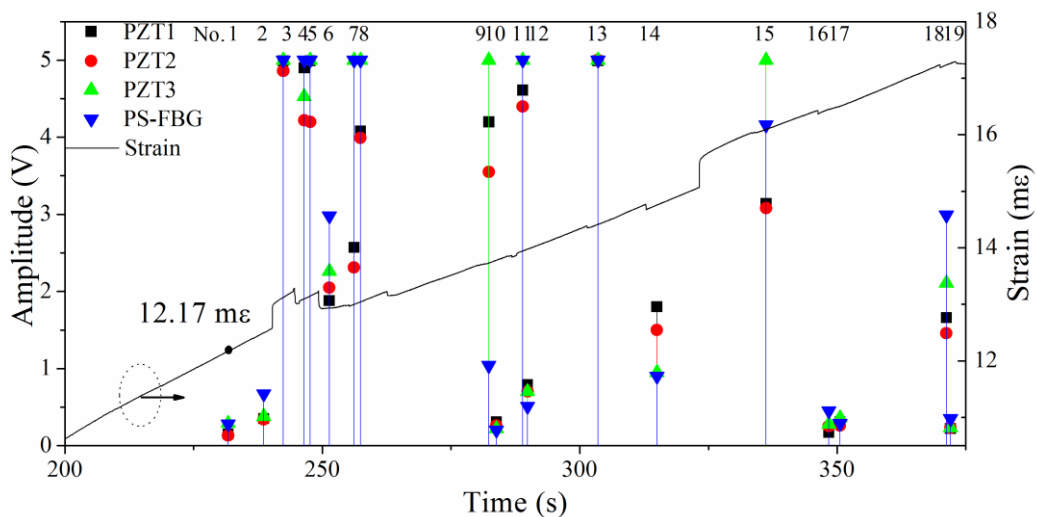
Figure 4.36. Relation between strain and AE signals in three point bending test.

In this experiment, 19 AE hits in each channel were detected. Observing the CFRP laminate under the microscope, we found 16 transverse cracks distributed with 14-mm range around the center of the CFRP laminate in both sides. The number of observed transverse cracks was fewer but close to the number of the detected AE hits, because some cracks did not penetrate in the width direction of the laminate and there was a possibility that other cracks also appeared from the other side surface.

From Figure 4.36, it is also noticed that AE signals have large different amplitudes: small one is as low as 0.2 V, while big one reaches the maximal output voltage of preamplifier. Furthermore, the signals detected by PZT1 and PZT2 have similar amplitudes in most case. However, the signals detected by PZT3 and PS-FBG sensor have relative large different amplitudes, such as the 9th AE signals, that can be explained in the following part.

Waveforms and wavelet transform results of the detected AE signals

Figure 4.37 shows typical waveforms of AE signals detected by four sensors. Figure 4.38 shows the CWT results of the waveforms detected by PZT3 and PS-FBG in Figure 4.37. In Figure 4.38(a) and (b), there both exist four areas. The wavelet coefficients in area 1 with low frequency have widest distribution on time domain, whereas those in area 4 with high frequency have most concentrative distribution on time domain from about 25 μs to about 40 μs. From area 1 to area 4, the distributions on time domain decrease, accompanying the increase of frequency. Figure 4.37 also shows this phenomenon, because the front part of the waveform contains higher frequency than the following part of the waveform. Furthermore, according to Figure 4.38, the different frequency components have different arrival time: area 1 has the earliest arrival time, whereas area 4 has the latest arrival time.
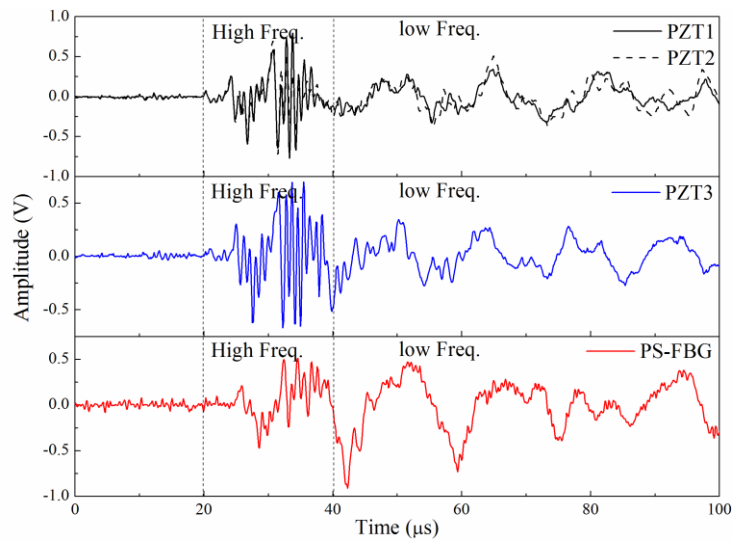
Figure 4.37. Typical waveforms detected by PZT sensor and PS-FBG sensor.
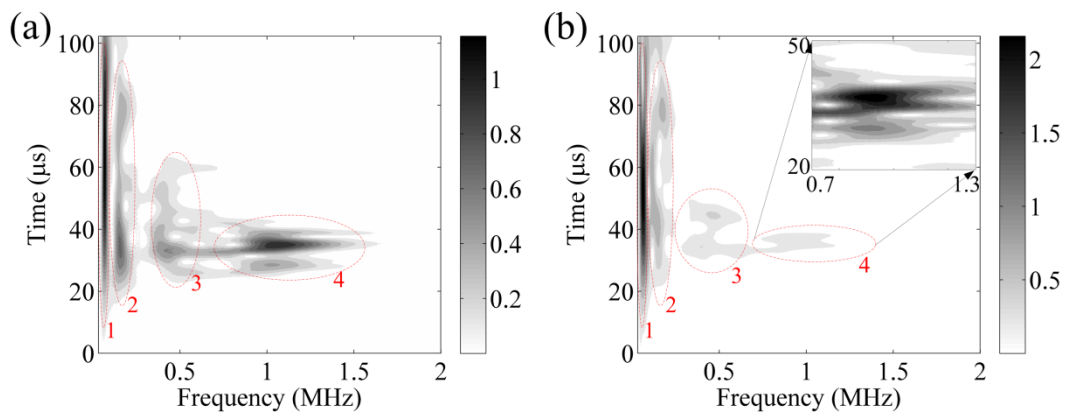
Figure 4.38. The CWT results of the waveform detected by (a) PZT3 and (b) PS-FBG. The inset shows the enlarged and normalized wavelet coefficients in area 4.

According to Figure 4.38, the signals detected by both sensors have broad bandwidth of about 1.5 MHz, which demonstrated that both sensors are broadband sensors, containing all the frequency information of the AE signals. For example, the inset in Figure 4.38(b), obtained by normalizing wavelet coefficients in area 4 in Figure 4.38(b), has almost the same shape as those in the same area in Figure 4.38(a). However, PS-FBG sensor and PZT sensor have different sensitivities to different frequency components. Specifically, PS-FBG sensor has higher sensitivity to low frequency. On the other hand, PZT sensor has relative flat sensitivity to high frequency. For example, the amplitude in the area 1 of PS-FBG sensor is about twice larger than that of PZT sensor, and the amplitude in the area 4 of PS-FBG sensor is about twice smaller than that of PZT sensor. The different sensitivities lead to the different amplitudes of the waveforms between front part and following part of the waveforms in Figure 4.37. For example, the front part of the waveform in PS-FBG sensor with high frequency components is smaller than the following part with low frequency components, whereas the phenomenon is opposite in the PZT sensor.

Moreover, the PS-FBG sensor has higher noise level than the PZT sensor. According to the waveforms in Figure 4.37, and by using standard deviation to evaluate the noise level in both sensors, the noise level in PZT sensor and PS-FBG sensor are 0.0123 V and 0.278 V, respectively. This higher noise level in PS-FBG sensor also can be seen in the inset of Figure 4.38(b), which contains more vague areas.

In addition, the waveforms detected by PZT1 and PZT2 in Figure 4.37 almost coincides with the same phase, showing the signals are basically S mode of Lamb wave, fitting theoretical and experimental results in reference [92] about the property of transverse crack very well. After comparing to the theoretical dispersion curve of grope velocity calculated by a commercial software DISPERSE, we further concluded that it is a specific S_0 mode mainly because the only existing S mode under the frequency of 1.5 MHz is S_0 mode. Due to the fact that all the signals present the same phenomena in PZT1 and PZT2, we assume all the detected signals were generated by transverse cracks. However, before applying this principle to PS-FBG sensor, additional calibration is needed. Because the phase of the waveform is not only decided by the phase of the Lamb wave, but also decided by the wavelength position of the TLS in the spectrum of the PS-FBG, and the connecting sequence of the transmitted light and reflected light to the BPD. For example, when the wavelength of the TLS is in the right sloping side of the peak of the PS-FBG, the Bragg wavelength shift to the left side will decrease the power. In contrast, when the wavelength of the TLS is in the left sloping side of the peak of the PS-FBG, the Bragg wavelength shift to the left side will increase the power. The influence of connecting sequence is derived from the positive and negative electrodes in BPD, which will not be explained in detail herein. In this experiment, the PS-FBG sensing system was calibrated to have the same phase response to the Lamb wave as the PZT sensor. Therefore, we also can apply the theory to check the property of the detected wave for further judging the damage types in composite materials.

Although AE signals were detected by this PS-FBG balanced sensing system, more solid evidences of the correspondences between detected signals and transverse cracks are needed. Thus, we repeated the three point bending test by the same experimental setup as previous experiment but with smaller applied strain. Only two AE signals were detected this time. The amplitudes of both signals were small, as the first two signals in Figure 4.36. Then, we observed the CFRP laminate under the microscope and found only two transverse cracks, which corresponded to the two signals very well. One of the transverse cracks is shown in Figure 4.39. Furthermore, we also noticed that these two transverse cracks did not penetrate the CFRP laminate. Thus, there is a possibility that the signals with small amplitudes correspond to the transverse cracks without penetration to the laminate. On the other hand, the signals with large amplitudes may correspond to transverse cracks that directly penetrate the laminate, as the large signals in Figure 4.36. However, this is an assumption which should be verified in future research.
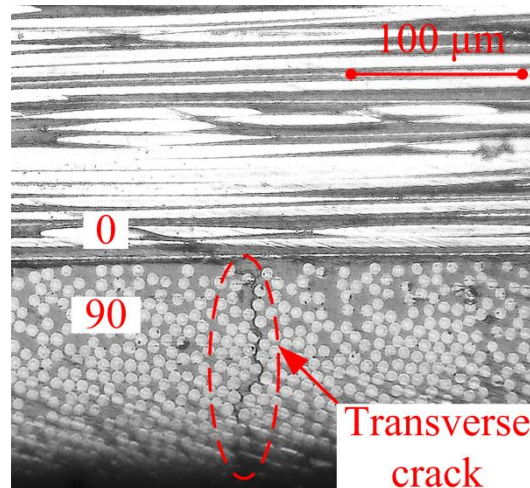
Figure 4.39. Transverse crack in the CFRP laminate observed by microscope

4.5.3   *Position identification*

Position identification based on the different arrival time of the Lamb wave

Because we only have one TLS in our lab, we cannot fully verify the position identification ability of PS-FBG balanced sensing system by using two PS-FBG sensors at the same time. Therefore, herein, the position identification was conducted by the combination of PS-FBG sensor and PZT sensor.
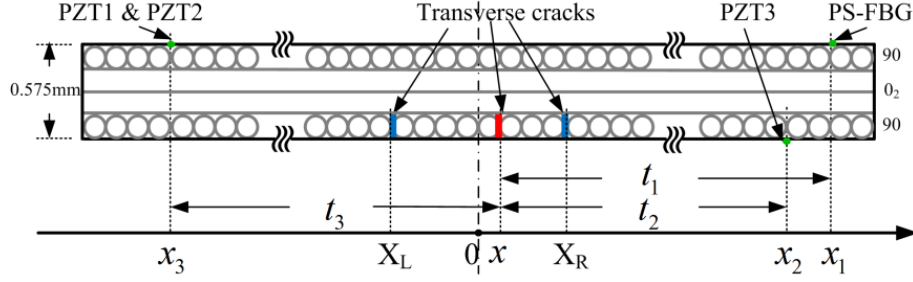
Figure 4.40. Schematic diagram of the position identification method. XR and
XL stands for the rightmost and leftmost observed transverse cracks.

Figure 4.40 shows the mathematical principle of the position identification based on the different arrival time of the Lamb waves in different sensors. Abscissa axis is firstly established with zero point at the center of the CFRP laminate. The right side of the coordination is positive. As we analyzed previously, the sensing point of the PS-FBG sensor is in the phase shifted point in the grating, whereas the sensing point of the PZT sensor is 4.33 mm near to the center of the PZT sensor. Thus, the actual corresponding sensing coordination of PS-FBG, PZT3, PZT1 (the same as PZT2) are $x_1 = 60$ mm, $x_2 = 55.67$ mm, $x_3 = -55.67$ mm. Then, we assume the propagation time of the Lamb wave from the AE position to the PS-FBG, PZT3, and PZT1 are t_1, t_2, and t_3, respectively. Although, t_1, t_2, and t_3 are unknown, the different arrival time Δt_1 (between t_1 and t_3), and Δt_2 (between t_2, and t_3) can be measured via the detected waveforms in different sensors. Therefore, we can obtain the following equations:

$$
\begin{cases}
(t_i + t_3)v = x_i - x_3 \\
t_i - t_3 = \Delta t_i \\
x_{PS-FBG} = x_1 - t_1 v \\
x_{PZT} = x_2 - t_2 v
\end{cases}
\tag{4.9}
$$

Where v is the velocity of the Lamb wave in CFRP laminate; $i = 1$, 2, x_{PS-FBG} and x_{PZT} stand for the position of transverse crack detected by PS-FBG sensor and PZT sensor. By simple calculation, we obtained the following equations.

$$
\begin{cases}
x_{PS-FBG} = \dfrac{(x_1 + x_3) - \Delta t_1 v}{2} \\
x_{PZT} = \dfrac{(x_2 + x_3) - \Delta t_2 v}{2}
\end{cases}
\tag{4.10}
$$

According to Eq. 4.10, we can calculate the AE position once we know the different arrival times of the AE signals in different sensors and the velocity of the Lamb wave in the CFRP laminate.

According to the calculated results by the software DISPERSE to this CFRP laminate, the group velocity of the S_0 mode of Lamb wave is dispersive. When the frequency is lower than 0.4 MHz, the group velocity is about 6 mm/μs; however, when the frequency is around 1.5 MHz, the group velocity decrease to about 4.7

89

mm/μs. Thus, before identification of the AE position based on detected wave, the velocity of the Lamb wave in an intact CFRP laminate was calibrated by acousto-ultrasonic detection. Two PZT sensors, the same type as used in the AE detection, were applied as actuator and sensor, respectively. The actual velocity of the Lamb wave in this CFRP laminate is 6.504 mm/μs, used as a reference. In addition, we also concluded that the effective sensing point of this PZT sensor is different by 4.33 mm from the center of the sensor. Therefore, the left most important issue in the position identification is precise determination of the arrival time of Lamb wave.

Data process method

Based on the waveform analysis in section 4.5.2, different sensors have different responses to different frequencies, which will cause errors in determination of arrival time because of the dispersion of the Lamb wave. Thus, we need to use threshold as low as possible to precisely measure the arrival time. However, the signals detected by PZT sensor and PS-FBG sensor both suffer noise problem, especially the PS-FBG sensor that has higher noise level. Therefore, suitable data process for noise rejection is necessary. In this case that the filter based on frequency analysis is not suitable owing to broadband property of AE signals., Wiener filter which is based on statistics is used to reject the noise effectively [95]. Then, Hilbert transform is to obtain the envelopes of the waveforms. The arrival time is determined by a threshold filter with threshold of 0.25 V, as the same setting value in the AE acquisition system. Then, based on the arrival time in different sensors, the different arrival time Δt_1 and Δt_2 can be calculated. Lastly, substituting Δt_1 and Δt_2 into the Eq. 4.10, we can identify the positions of the transverse cracks. Figure 4.41 is the flow chart of the data process method. Figure 4.42 shows the performances of the Wiener filter and Hilbert transform to the signal shown in Figure 4.38 detected by PS-FBG sensor. In Figure 4.42, we can see that Wiener filter effectively decreases the noise level and Hilbert transform obtains the envelope of the waveform.

Wiener filter is able to reduce the in-band noise; however, there are also two disadvantages. It has deformation to the detected waveforms, especially to the area with large amplitude. Because of the small amplitude of the front part of the waveform, it has small influence to the position identification accuracy. On the other hand, it may cause error especially when the SNR of the detected signal is low. Because Wiener is based on statistics, it sometimes mistakes the noise to signals. However, these two problems are mathematic, we do not discuss it deeply in this dissertation.
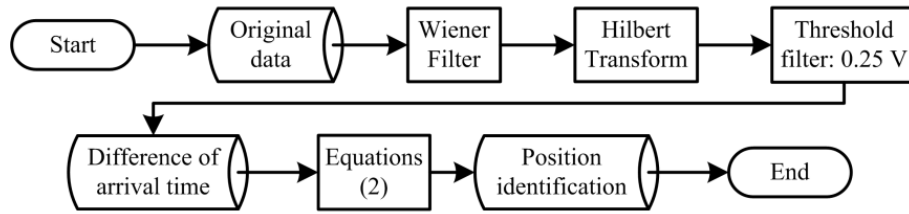
Figure 4.41. Flow chart of the data process method
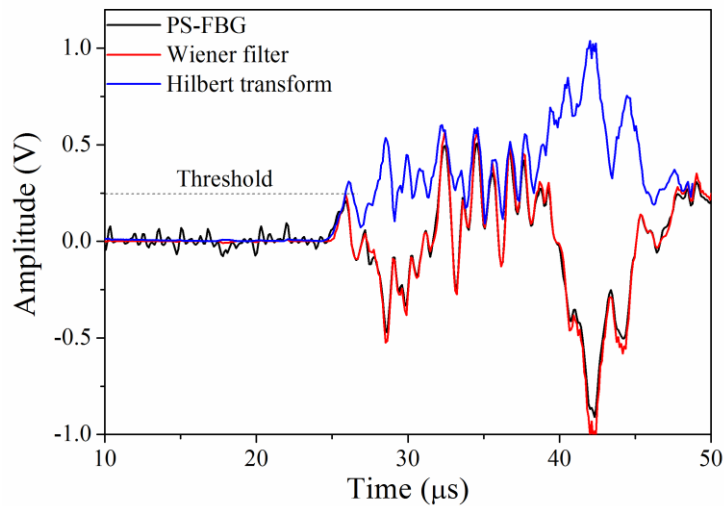
Figure 4.42. The performance of the Wiener filter and the Hilbert transform.

Position identification results

Figure 4.43 shows the position identification by PS-FBG sensor and PZT sensor. The right boundary with coordinate of 24 mm and left boundary with coordinate of -24 mm are defined by the position of the support bars in view of our assumption that the AE signals only generated between the bars. The two dot lines stand for the observed rightmost transverse crack at 7 mm and leftmost crack at -7 mm. In Figure 4.43, the positions identified by PZT sensor were treated as references because using PZT sensor to estimate the AE position is a commercial and mature technique. The positions identified by PZT sensor are almost in the range from 7 mm to -7 mm. The positions identified by PS-FBG sensor are also in the same range and close to the position identified by PZT sensor, except the 16th and the 17th AE hits. The 16th AE hits detected by PZT sensor and PS-FBG sensor have large different positions, and the 17th AE hit detected by PS-FBG sensor is not shown in Figure 4.43, because it is out of the boundaries. After comparing to Figure 4.36, we believe these errors are mainly caused by the low SNR in PS-FBG sensor. The stand deviation of differences of positions identified by PS-FBG sensor and PZT sensor are 2.098 mm, i.e. the error of position identification is controlled around 2 mm by PS-FBG sensor combined with this data process method. Considering the propagation length of the Lamb wave, we believe that the percentage error of the position identification is lower than 4%, which is very precise. Furthermore, the average position difference detected by PZT sensor

91

and PS-FBG sensor is 2.177 mm, caused by the inaccurate gluing position of the PS-FBG sensor. The leftmost transverse crack detected by PS-FBG sensor and PZT sensor are -7.43 mm and -6.5 mm, respectively. The rightmost transverse crack detected by PS-FBG sensor and PZT sensor are 6.23 mm and 7.97 mm, respectively. There results fit the observed results very well, showing the large potential of the position identification by the PS-FBG sensor.
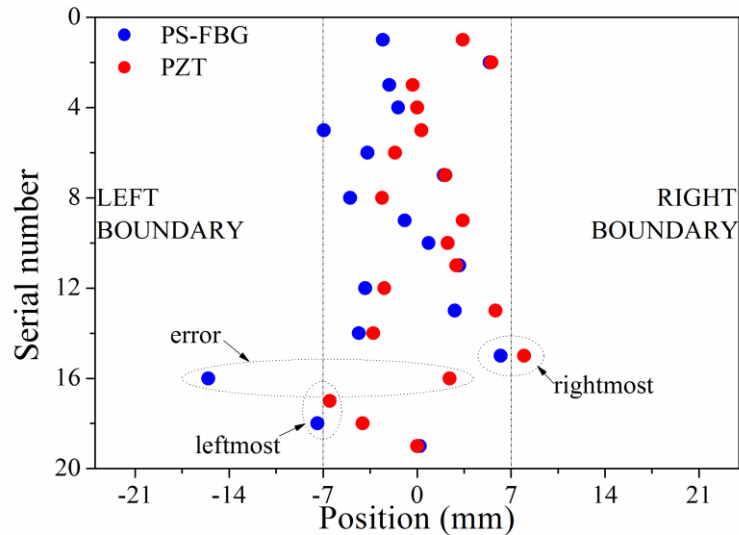
Figure 4.43. Position identification by PS-FBG sensor and PZT sensor

In this data process, the threshold in the threshold filter has apparent influence to the results, similar to other experiments [96, 97]. For example, if we increase the threshold of PS-FBG and PZT3 to 0.3 V, although the results are basically similar to what are shown in Figure 4.43 with threshold of 0.25 V, the 19th AE hits detected by PS-FBG sensor, and the16th AE hits detected by PS-FBG sensor and PZT sensors will be out of the boundaries.

By further analyzing, we found that the signals with large amplitudes have better capability of immunity to threshold. Signals with low amplitude sometimes easily cause error of position identification, such as 16th, 17th and 19th analyzed previously. In addition, PZT sensor with higher SNR suffers smaller influence by threshold. However, PS-FBG sensor with lower SNR, especially the low sensitivity to front part of the wave with high frequency, is easily influenced by threshold. Therefore, enhancing the sensitivity of PS-FBG sensor to high frequency ultrasonic wave is the crux to guarantee the ability of position identification.

4.5.4 *Conclusions*

In this research, we applied PS-FBG balanced sensing system to AE detection and position identification of transverse cracks in CFRP laminate in three point bending test.

In the three point bending test, the signals detected by PS-FBG sensor and PZT sensor had the same number, though the amplitudes were different. PS-FBG sensor

had high sensitivity to low frequency while PZT sensor had high sensitivity to high frequency. We also did the CWT to confirm the different responses to different frequency components between these two different sensors. By analyzing the properties of the detected waveforms and comparing to observed transverse cracks, we demonstrated this sensing system can detect transverse crack AE signals with low amplitude and high frequency in composite materials.

Based on the detected waveforms and suitable data process method, we partially verified the position identification ability of the optical sensing system. By precisely measuring the arrival time of the Lamb wave in every sensor, we can identify the position of the transverse cracks precisely with percentage error lower than 4%. Moreover, the leftmost and rightmost transverse cracks also fit the observed positions very well.

The report in this section is the first report of the successful detection of transverse crack AE signals in composite materials in three point bending test using optical fiber sensor to our knowledge. Furthermore, it also demonstrates the position identification ability of this sensor.

5 FIBER RING LASER SENSING SYSTEM WITH INBUILT PS-FBG

In chapter 4, we proposed a high performance ultrasonic optical fiber sensing system based on edge filter technique and used it in practical AE detection of composites. Theoretically, according to Eq. 4.8, the sensitivity of the PS-FBG balanced sensing system can be improved further by using PS-FBG sensor with narrower FWHM. However, it is not practical in reality. The narrow peak in the PS-FBG leads to the demodulation system instability because environmental temperature changes or quasi-static strain changes will easily shift the Bragg wavelength of the PS-FBG out of the dynamic range. Although feedback controller or the Pound-Drever-Hall method can stabilize sensing systems, these methods require complex configuration and high costs. Therefore, the demodulation of PS-FBGs using normal external independent laser should be carefully considered in practice, especially for the case of ultrasonic detection of CFRP laminates. Because CFRP laminates are commonly used in harsh aerospace environments, traditional demodulation systems are not sufficiently robust. Tsuda has recently proposed using optical fiber lasers incorporated with FBG to achieve temperature or quasi-static strain robustness [98]. However, it is believed that these systems are not sensitive enough. To our knowledge, there is no sensing system which can simultaneously solve or even alleviate the problems among sensitivity, bandwidth, robustness, and cost.

On the other hand, fiber laser has been studied in these years. Fiber laser is a novel laser source. Many kinds of optical amplifier provides the gain in the fiber laser, including EDFA, semiconductor amplifier, Raman amplifier, Brillouin amplifier, or hybrid amplifier. In this dissertation, we discuss erbium fiber laser (EFL). The optical amplifier in the EFL is EDFA, which is the most widely used optical amplifier [99, 100]. EDFA is constituted by a pump power which is 980-nm or 1480-nm, a section of erbium doped fiber (EDF) as gain media, and necessary accessories including wavelength-division multiplexer and so on. When 980-nm pump is used, pump light pumps erbium ions from their ground-state manifold $^4I_{15/2}$ to the $^4I_{11/2}$ manifold, where there is a quick non-radiative transfer to the upper level $^4I_{13/2}$. Thus, population inversion occurs during this process. When, a signal light with wavelength in the C-band (from approximately 1530-1570 nm) injects into the EDF, simulated emission occurs to amplify the signal light. Due to many merits of EDFA, the innovation of EDFA leads the revolution in optical communication for practical long distance information transmission.

Usually fiber laser has long laser cavity, which is SMF in almost all the cases. Thus, fiber laser has usually multi-longitudinal modes. For single longitudinal mode oscillation, short cavity or ultra-narrow filter is required [101]. Furthermore, due to the dominantly homogeneous broadening of the EDF, two wavelengths lasing cannot oscillate simultaneously unless certain techniques are used [102, 103].

The EFL has been used as a light source for optical communication or sensing. Then, some researchers have proposed the potential application of the fiber laser as a sensing element by itself. When the temperature shifts the Bragg wavelength of the inbuilt FBG, which has function of sensor and filter, the lasing wavelength will also shift [104-106]. The application in communication and sensing until now are almost on the static properties of the EFL. On the other hand, the dynamic properties of the EFL are always treated as negative effects, which should be prevented from in practical applications [107]. However, several researchers explore the potential application of EFL for dynamic sensing recently. A gas sensor based on EFL has been proposed by Stewart *et al*. [108, 109]. The ultrasonic sensing system proposed by Tsuda is another example [98]. Han *et al.* also proposed an ultrasonic sensing system based on intensity modulation of fiber laser with inbuilt FBG [110, 111]. However, in their design, the lasing wavelength is decided by a tunable Fabry-Perot filter, which is controlled and stabilized by an external electrical signal, i.e., it does not have temperature robustness. To a certain extent, this technique is a refurbished design of the edge filter sensing system, except that the light source is fiber laser. The above mentioned researches are the attempts of fiber laser application in sensing area related to its dynamic properties.

In this research, we propose and demonstrate a novel ultrasonic optical fiber sensing system (laser-sensor) based on an EFL with an inbuilt PS-FBG. A corresponding theory is also proposed to explain the physical phenomena and the properties of the sensing system. All of our experimental results fit the numerical simulation results well, showing that this design has high sensitivity, broad bandwidth, robustness, and low cost. However, we also point out several problems in the laser-sensor system, and proposed reasonable solutions. As a result, this sensing system has great potential as an alternative to traditional PZT sensors in high-standard practical applications, especially in harsh environment.

5.1   System Setup and Detection Principle

Figure 5.1 shows the experimental setup of this EFL and spectra of FBGs. As shown in Figure 5.1(a), an erbium doped fiber amplifier (EDFA) (FiberLabs, AMP-FL8013) with 980-nm pump generates enough gain for laser oscillation. Two polarization controllers are used to control the polarization status in the EFL. 10 percent of the laser power is lead out of the ring cavity by an optical coupler, then monitored by an OSA and detected by a PD1 with gain setting of 10. After the PD1, an ESA and an O-scope are connected for observing EFL's response to ultrasonic wave. PS-FBG3 and AFBG are connected after a circulator are inbuilt in the ring cavity. Figure 5.1(b) shows the transmitted spectrum of the PS-FBG3 and the reflected spectrum of the AFBG, observed by OSA. The AFBG and the PS-FBG3 have approximately the same Bragg wavelength, and the reflected peak of the AFBG almost covers the transmitted peak area of the PS-FBG. The inset of Figure 5.1(b) shows the detailed observation of the peak area of the PS-FBG3 with about 1.6-pm FWHM, obtained by wavelength sweeping of a TLS. According to Figure 5.1(b), these two FBGs constitute a filter

with ultra-narrow FWHM for laser wavelength determination; however, their insertion losses are high. Besides being used as a filter, the PS-FBG3 is also used to receive the ultrasonic waves. Acousto-ultrasonic method is used to investigate the dynamic responses of the EFL to ultrasonic wave. The N-PZT is used as an actuator, glued on an aluminum plate. The PS-FBG3 in the EFL is glued about 8 cm away from the actuator in line. The other N-PZT and PS-FBG2 demodulated by the balanced sensing technique, are also glued near to the PS-FBG3 in the EFL as references. All the sensors are glued using high-acoustic impedance ultrasonic couplant.
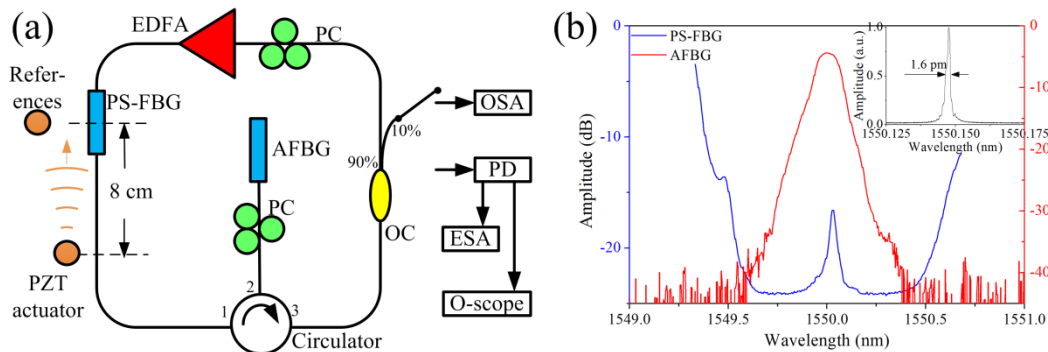
Figure 5.1. Experimental setup of EFL and spectra of FBGs. (a) Configuration of the EFL. (b) The transmitted spectrum of the PS-FBG3 and the reflected spectrum of the AFBG. The inset shows the peak area of the PS-FBG3 has a FWHM of approximately 1.6 pm.

Figure 5.2 shows the principles of EFL. First, the laser emits when the gain generated by the EDFA and tailored by both the PS-FBG3 and AFBG exceeds the loss in the ring cavity. Because of the ultra-narrow FWHM of the PS-FBG and the dominantly homogeneous broadening property of the EDF, single longitudinal mode will oscillate under the ideal steady-state condition. The exact lasing wavelength is determined by both the Bragg wavelength of the PS-FBG and the longitudinal mode positions of the ring cavity, i.e., the longitudinal mode which is nearest to the Bragg wavelength of the PS-FBG is the exact lasing mode.

After the laser is established, the sensing principle of the EFL is similar to FBG demodulation by an external independent TLS [48]. The output power of the EFL changes when ultrasonic strain shifts the Bragg wavelength of the PS-FBG, because the insertion loss from the PS-FBG is varied. Mainly due to the short effective grating length and the ultra-steep peak area slope of the PS-FBG, the achievable sensing bandwidth and sensitivity of this EFL will be much better than that of traditional FBG sensing system. However, EFL's ultrasonic dynamic responses show several unique properties, such as waveform deformation and frequency-dependent amplitude.

Besides the high sensitivity and the broad bandwidth, the EFL is very robust. When temperature or quasi-static strain significantly shifts the Bragg wavelength of the PS-FBG, the lasing longitudinal mode will hop to a neighboring position, emitting light with different wavelength. From another view point, the intra-cavity PS-FBG is

96

still interrogated in the save way by the light within the cavity after the mode hop(s), giving a solution between high sensitivity and temperature-induced instability.
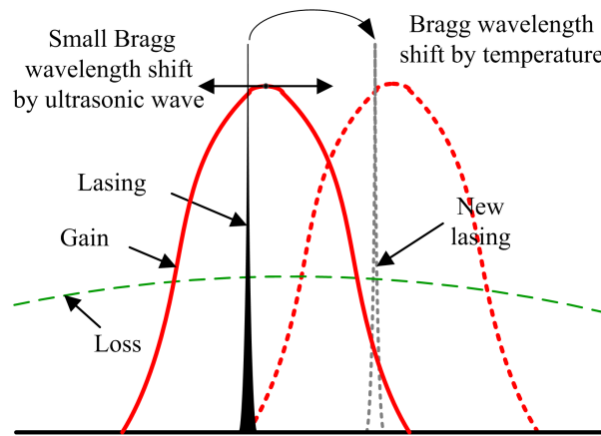
Figure 5.2. Sensing and self-adjustment principles.

5.2 Numerical Simulation

5.2.1 *Assumptions*

Before establishment of the numerical simulation model, several assumptions are clarified herein firstly.

The first assumption is about the model of EDFA. Two-level model is used to describe the EDFA in the EFL. When the pump power has wavelength of 980 nm, although it is more precisely described by three-level model, two-level model is enough precious for making the results accurate due to the short life time of atoms on the pump level of $^4I_{11/2}$, when the pump power is lower than 1 W according to previous research. This simulation condition fits our experimental condition. Furthermore, usually EDF is divided into several sections because actually the photon number in the upper states is not uniform along the EDF section. However, it will make the equations very complicated. We mainly focus on the dynamic behavior of the EDF in this study, thus the gain in the EDF is averaged, i.e., averaged parameters are used in the simulation. The possibility and the accuracy of this method have been studied by other researchers. Owing to this process, the partial differential equations (time and distance related) which are used to describe the amplifying physical theory of EDF are degenerated to differential equation which is only time dependent.

The second assumption is about the longitudinal modes in the EFL. Normal EFL contains many longitudinal modes, thousands perhaps, due to dense longitudinal mode spacing (LMS) and relative broad FWHM in the filter. Although the cavity length of our fiber laser is long, leading to dense LMS. the filter which is PS-FBG3 has ultra-narrow (1.6 pm) FWHM. Therefore, there are only dozens of longitudinal modes may exist in the output of our EFL. Assume 100 longitudinal modes exist, the spectrum range is 0.2 nm, corresponding to 0.0002 dB change in the absorption and emission coefficients of the EDF. These differences can be neglected. Thus, according to this evaluation, the absorption and the emission coefficients of the EDF in our

mode are constant rather than wavelength dependent for simplification. Due to the same reason, the wavelength of the output light is assumed at 1550 nm.

The EDF in our model is considered as homogeneous broadening gain media. It is true that EDF also shows certain properties of inhomogeneous broadening; however due to its small effect, we ignore it. But it may contribute some difference between simulation results and experimental results. Neither spectral hole burning nor polarization hole burning is taken into account in this simulation. More common assumptions are the same as those listed in the references [112].

Then, certain assumptions are applied to the optical filter which is the PS-FBG3 in our design. According to our previous research, the spectrum of PS-FBG has complex shape. However, due to its similarity, Gaussian function can approach the filter characteristic of this PS-FBG. Moreover, the response of the PS-FBG3 to ultrasonic wave, specifically the Bragg wavelength shift, also shows complicate behavior when the ultrasonic wave has high frequency. It has been studied in previous simulation in Chapter 2. We simply assume the Bragg wavelength shift follows sinusoidal function and maintains its spectrum shape herein.

5.2.2 *Parameters and Equations*

Table 5. Parameters used in the simulation of dynamic EFL.

Symbol	Meaning	Unit	Value
h	Planck Constant	Js	6.626
c	light speed	m/s	3e8
n	index of the fiber		1.456
L	cavity length of the EFL	m	28
ρ	erbium ion density	ions/m^3	2e24
S	core cross sectional area of the fiber	μm^2	8.04
l	length of the EDF	m	3.6
τ_0	lifetime of the upper state	ms	10
α	loss in the ring cavity excluding the EDF	dB	8
λ	Signal wavelength	nm	1550
P	pump power	mW	225
α_p	absorption coefficient of the EDF at the pump wavelength	dB/m	4.64
γ_g	emission coefficient of the EDF at the signal wavelength	dB/m	3.7
α_g	absorption coefficient of the EDF at the signal wavelength	dB/m	3
$\Delta\lambda$	FWHM of the filter	pm	0.8
T	maximum transmittance of the filter		1
F	ultrasonic frequency	kHz	Changed
λ_s	Bragg wavelength shift	pm	Changed
N_2	length averaged inversion level		unknown
M_m	photon numbers of the mth longitudinal mode		unknown

Firstly, basic parameters including their symbols, meanings, units and values, are given in this simulation, as shown in Table 5.

Then, several parameters are derived.

The round trip time of the laser cavity τ can be derived by $\tau = nL/c$.

The LMS is λ^2/nL, which is about 0.06 pm. In our simulation, we consider the wavelength range from 1549.997 nm to 1550.003. Thus, about m=100 longitudinal modes are considered in this range.

The amount output photons M are the summation of all the photons of the m longitudinal modes $\sum_{1}^{m} M_m$.

The pump power P_p in unit of photons/second has relation to the pump power P, as $P_p = P\lambda/hc$.

Then, according to the same relation, the output power detected by PD is proportional to the power shown as $P_{out} = \dfrac{hc}{\tau\lambda} \sum_{1}^{m} M_m$.

The transmission characteristic of the filter is written as Gaussian function:

$$F_m = T \exp\left(-\left(\frac{\lambda_m - \lambda}{\Delta\lambda}\right)^2\right) \tag{5.1}$$

where F_m is the transmittance at the wavelength λ_m of mth longitudinal mode.

The Bragg wavelength shift under the ultrasonic wave is written as $\Delta\lambda(t) = \Delta\lambda \sin(2\pi ft)$.

The length-averaged pump absorption coefficient can be written as $g_p = -\alpha_p(1 - N_2)$.

The length-averaged gain coefficient for laser mode is $g_g = (\gamma_g + \alpha_g)N_2 - \alpha_g$.

The ASE amplification factor for laser mode is written as $A_g = (e^{g_g l} - 1)/g_g l$.

Eq. 5.2 and 5.3 are the expression for the dynamic properties of the EFL. These differential equations describe the change rate of N_2 and M_m.

$$(\rho Sl)\frac{dN_2}{dt} = P_p\left(1 - e^{g_p l}\right) - (\rho Sl)\frac{N_2}{\tau_0}$$
$$- \sum_{1}^{m} \frac{M_m}{\tau}\left(1 - e^{-g_g l}\right) - 4m\frac{\gamma_g l N_2}{\tau}\left(A_g - 1\right) \tag{5.2}$$

$$\frac{dM_m}{dt} = \frac{M_m}{\tau}\left(F_m e^{g_g l - \alpha} - 1\right) + \frac{2}{\tau}\gamma_g l N_2 A_g \tag{5.3}$$

In the Eq. 5.2, the left-hand side (LHS) represents the total photon changes in the upper state; the first term in the right-hand side (RHS) represents the pump absorption

rate; the second term in the RHS represents spontaneous emission rate; the third term in the RHS represents the stimulated emission rate; the forth term in the RHS represents the change rate of N_2 caused by the ASE. In the Eq. 5.3, the LHS represents the photon change of certain longitudinal mode; the first term in the RHS represents the photon number change in each circulation of the EFL; the second term in the RHS represents the influence from ASE.

These two equations are deduced from the equations in references [109, 110]. In those researches, the laser is multi-longitudinal modes with relative spectral width. Thus, mode group which has similar coefficients, are used. However, according to our second assumption, we consider the longitudinal modes individually albeit with same absorption and emission coefficients.

5.2.3   *Simulation Methods*

In order to solve the Eq 5.2 and 5.3, Runge-Kutta method is applied and relative programs are written by Matlab code, appended in the appendix C. There are two points we would like to specify here. The reason of selection ode45 is due to the high accuracy and the un-stiff differential equations. If other ODE member is used, such as ode15s, large error will occur, especially in the simulation of initial setup process of the laser (it cannot get stable). ode45 has variable step size and conflicts to the normal simulation of the input ultrasonic signals. Thus, the method used in our simulation is interpolation of the input ultrasonic signal based on the step position of the ode45. The interpolation method used here is 'pchip' (shape-preserving piecewise cubic interpolation). 'linear' and 'nearest' interpolations are not accurate when the step is large; 'spline' will cause large error in certain conditions, especially when abrupt change exists.

Firstly, we assume that the filter is stable, and a step pump power input with level of P is applied. After a period of time with spikes and damped relaxation oscillation (RO) [113, 114], a stable condition can be obtained, including the optical spectrum and the temporal response. Then, this stable condition is used as initial value for further dynamic simulation. Three cases are considered in this simulation. Firstly, we simulate the output of the laser when low frequency vibration is applied to the filter to demonstrate its self-adjustability, which is the case of the environmental temperature change or quasi-static change. Then, we simulated the output of the laser when the continuous sinusoidal wave shifts the PS-FBG. Lastly, the case that a burst signal is applied to the filter is considered. The dynamic properties are evaluated under the different initial position of the longitudinal mode and the different frequency of the input signal.

5.2.4   *Simulation Results*

Initial steady-state condition

Figure 5.3 shows the transmittance of the filter (red line) and the simulated lasing wavelength of the EFL (blue dots) in steady-state condition. Although the transmittances near to the peak of the filter are very similar, only the longitudinal mode which processes the largest transmittance oscillates, fitting the dominantly homogeneous broadening property of the EDF well, i.e., the EDF usually only supports single longitudinal mode laser oscillation in ideal steady-state condition. Because the longitudinal modes have the identical LMS, the wavelength of the laser will always be near to the peak of the filter in the range of one LMS (from –LMS/2 to LMS/2), as shown in the inset of Figure 5.3. However, the exact position is uncontrollable in practice. Thus, we consider 9 different positions with equal interval of LMS/20 in the left side of the filter marked as 1 to 9 in our simulation. These different positions will influence the sensing results, as discussed in the section 4.5 and 4.6. Due to the symmetric property of the PS-FBG filter, the other side of the filter should have the same waveform results albeit with opposite phase.
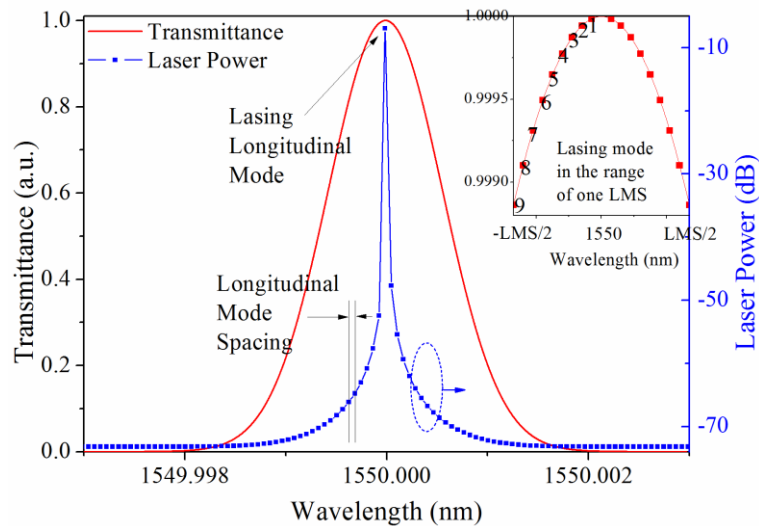
Figure 5.3. Transmittance of the filter and lasing wavelength of the EFL. Red line is the transmittance of the filter; blue dots are the laser output power in each longitudinal mode positions. Inset shows 9 different initial lasing longitudinal mode positions near to the peak of the filter.

Figure 5.4 shows the laser establishing process. When a step pump is applied at 0 ms, after a certain delay, the laser output shows a number of spikes and undergoes damped relaxation oscillation (RO) before the steady state is reached. The simulated laser will finally get stable, as shown in the inset of Figure 5.4. The exact laser wavelength determined by the longitudinal mode position has little influence on the DC output of the laser, because the transmittance of the filter has negligible differences in the range of one LMS. The final stable output of the laser at different initial lasing longitudinal mode positions is used as initial conditions in the dynamic simulations in section 4.4 - 4.6.
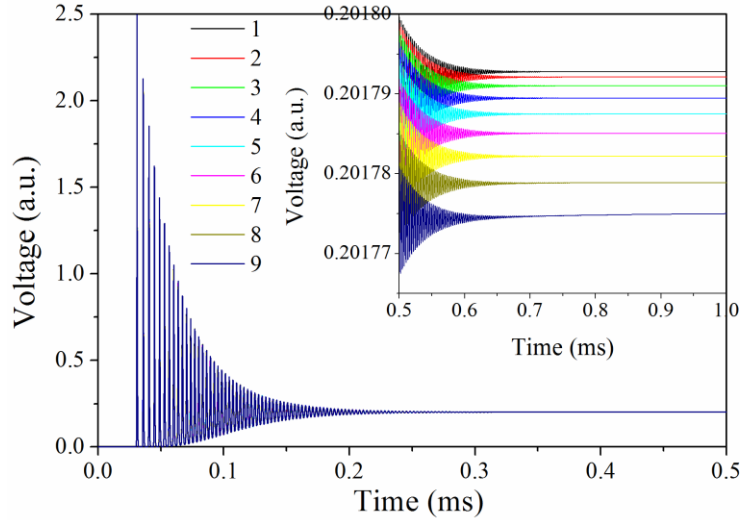
Figure 5.4. Laser establishing process at different initial longitudinal mode positions shows spikes and damped ROs. The inset shows different DC output when the laser is stable.

Response to quasi-static change

Firstly, we consider the dynamic response of the EFL to quasi-static change, corresponding to the environmental influences from strain and temperature. Under the quasi-static change, we assume the Bragg wavelength of the PS-FBG shifts as a half-cycle cosine curve shown in Figure 5.5(a). The Bragg wavelength changes 0.25 pm (about 5 LMSs) in 20 ms, equaling to 1.25 degree temperature change or 10.5-με strain change per second. Figure 5.5(b) shows each longitudinal mode changes in the time domain. When the Bragg wavelength of the filter is within one LMS (over 0 – 5ms), the output intensity of the lasing longitudinal mode varies due to the changing transmittance of the PS-FBG. Once the Bragg wavelength shift exceeds one LMS (around 6 ms), the longitudinal mode at initial position will decrease rapidly due to the large loss; however, the neighboring longitudinal mode (+LMS) will lase because the gain of the EDFA exceeds the loss of the cavity. This physical phenomenon repeats, once the Bragg wavelength caused by quasi-static change shifts out the range of one LMS. In our simulation, 5 longitudinal modes lase one by one. Although, the lasing modes are different, the power output (proportional to voltage) is almost stable as shown in Figure 5.5(c). The vibration of the power output is smaller than 0.2% of the DC voltage. Owing to the low-frequency negligible change, it will have no influence to the ultrasonic detection of this EFL. Thus, this EFL is robust due to its adjustment ability.
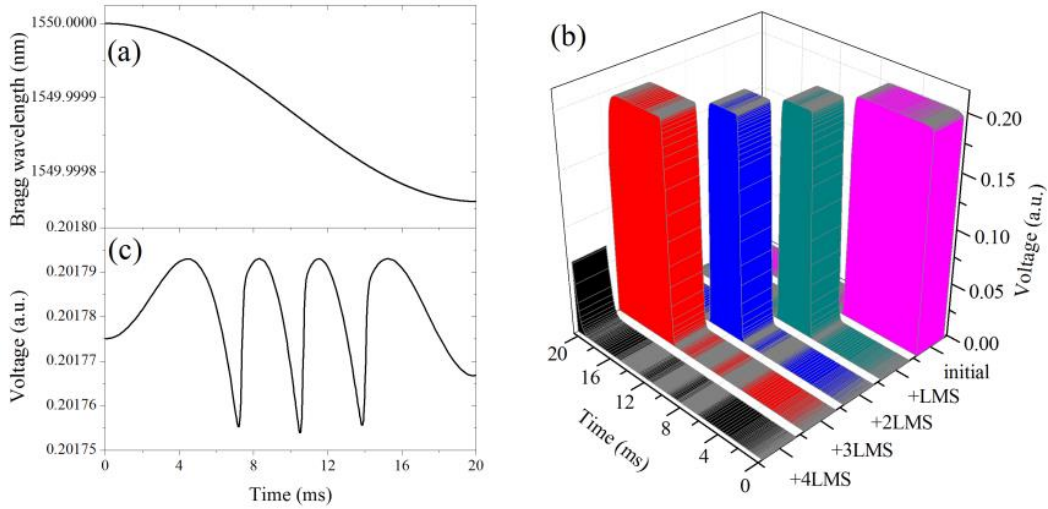
Figure 5.5. (a) Bragg wavelength shift of the PS-FBG under the quasi-static strain change or temperature change. (b) Lasing mode hopping. (c) Amount output change shows very small power fluctuation.

Responses to continuous ultrasonic wave

Then, we consider the dynamic response of the EFL to continuous ultrasonic sinusoidal wave. Herein we assume the ultrasonic wave has frequency of 1 MHz, and shifts the Bragg wavelength of 0.005 pm. As shown in Figure 5.6, the output of the EFL shows clear and periodic waveforms after transition time. The inset of Figure 5.6 amplifies one small section of time for clearly manifesting the output curve. The output sinusoidal waveform has the same frequency of the input signals, demonstrating the dynamic response of the EFL to ultrasonic wave, because the EFL demodulates the Bragg wavelength shift of the PS-FBG filter.
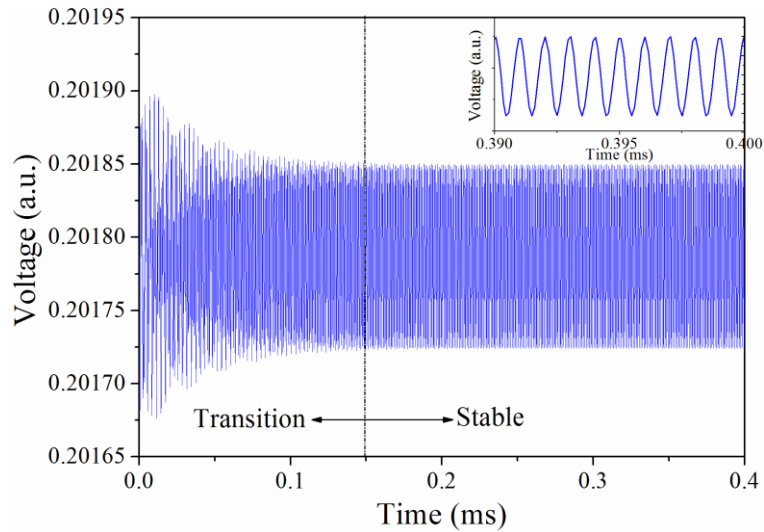
Figure 5.6. Dynamic response of the EFL to continuous sinusoidal wave. The inset shows a short time range of the dynamic response.

103

Responses to burst signal

Next, we simulate the response of the EFL when the input burst signal is ten-cycle sinusoidal wave with a Hamming window. The input middle frequency is 1 MHz. Figure 5.7(a) and 5.7(b) show the different responses of the EFL with different initial lasing longitudinal mode positions when the Bragg wavelength shift are 0.1 fm and 0.01 pm, (corresponding to 0.083 nε and 8.3 nε [39]), respectively. Compared with the ultrasonic waveform, the output intensity waveform from the EFL has small deformations, such as the areas marked by the dotted circles. The decaying tail-like oscillation after the main envelope has the same frequency as the RO.
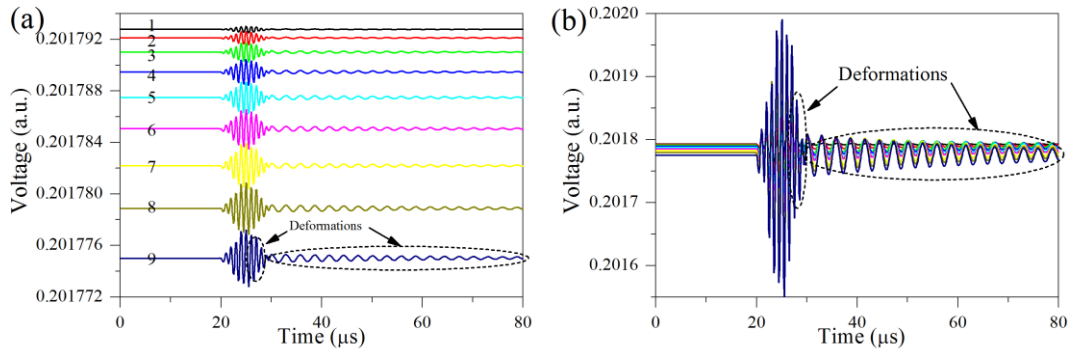
Figure 5.7. Dynamic response of the EFL to burst sinusoidal wave. (a) When the input strain signal is small; (b) when the input strain signal is relative large.

It is better that the deformation can be removed in order to perfectly recover the actual ultrasonic waveform for performing analysis of ultrasonic NDT. Figure 5.8(a) shows the normalized input waveform (red line) and the detected waveform (blue line). Figure 5.8(b) shows the corresponding spectra, which clearly contain 1-MHz signals. However, there is a large 350-kHz peak in the EFL caused by the RO. This deformation in the detected waveform can be removed by applying a supposed high-pass filter. Figure 5.8(c) shows the recovered waveform after this supposed high-pass filter with suitable 500-kHz cut-off frequency, which perfectly matches the actual input waveform. In Figure 5.8(b), the small peak in 2 MHz (twofold frequency of the input single) is probably caused by nonlinear slope of the PS-FBG, because the slope of the filter is not completely linear around the peak area. However, it will not influence our analysis in the ultrasonic NDT due to its very low energy; thus, the higher order peak is ignored in the following experiment and data process.
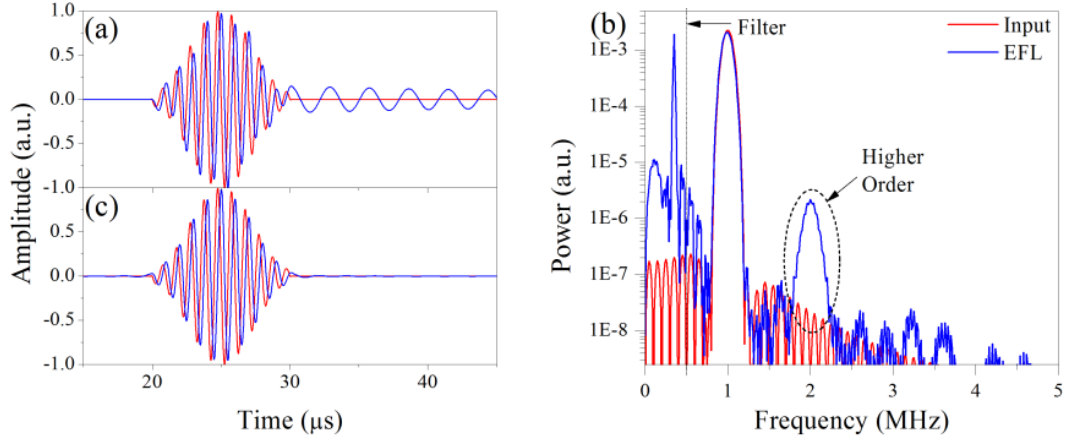
Figure 5.8. (a) Original normalized burst signals; (b) the corresponding spectra; (c) burst signals after high-pass filter.

Ultrasonic response properties

Figure 5.9 shows the effective estimated sensitivity of the detected waveforms from the EFL and from the same PS-FBG but demodulated by external independent TLS under different strains. The effective estimated sensitivity is evaluated by:

$$\text{Sensitivity} = \frac{\left(V_{\max} - V_{\min}\right)}{V_{DC} \cdot S}. \qquad (5.4)$$

where $V_{\max}$ and $V_{\min}$ are the maximum and minimum values of the output voltage, V_{DC} is the DC output voltage, and S is the input ultrasonic strain. In Figure 5.9, neither small strain (0.083-nε) nor large strain (8.3-nε) affects on the sensitivities detected by this EFL. When the lasing longitudinal mode is at position 9, although 8.3-nε strain will shift the Bragg wavelength out of one LMS, the ultrasonic signal is still detectable. Because the neighboring longitudinal mode does not have enough time to oscillate due to the high frequency of the ultrasonic signal, the actual dynamic range of the EFL to ultrasonic signal is larger than one LMS. According to Figure 5.9 as well as Figure 5.7, the sensitivities of the detected ultrasonic signals are influenced by the initial lasing longitudinal mode positions. When the position approaches to the peak of the filter (such as position 1), the sensitivity decreases due to the relative gentle slope. However, the sensitivity is still very high due to the steep slope and the broad ultrasonic bandwidth. In practice, the exact lasing wavelength of the EFL is unknown and uncontrollable due to the environmental quasi-static change. Therefore, the sensitivity of the detected ultrasonic signal always vibrates, which is a bad side-effect of the self-adjustment. As a result, this EFL is suitable to be used in application based on mode analysis rather than amplitude analysis in ultrasonic NDT, such as the technique demonstrated in reference [21].

Unlike demodulation by an external TLS, the slope of the response curve for the EFL in Figure 5.9 is influenced by ultrasonic frequency, i.e., the EFL has different responses to different frequencies. The open dots shown in Figure 5.10 are the intensities (square of the amplitude) of the detected signals from the EFL. Figure 5.10

can be roughly divided into three areas. In area 1, the intensity decreases with the increase in frequency, exactly fitting to Lorentz curve with central frequency of 350-kHz, which is the frequency of RO. In the area 1, all the waveforms detected by the EFL can be recovered by the data process method mentioned in section 4.5. In area 2, the detected intensity is very large, marked by red square. The waveform in this area has frequency so close to the frequency of RO, that it cannot be recovered by data process based on frequency analysis, such as the waveform with 350-kHz shown in the inset of Figure 5.10. Thus, the frequency in area 2 is not suitable for ultrasonic NDT, but maybe has other applications. In area 3, the intensity decreases rapidly with decrease in frequency and deviate from the Lorentz curve, although the waveform can be recovered.
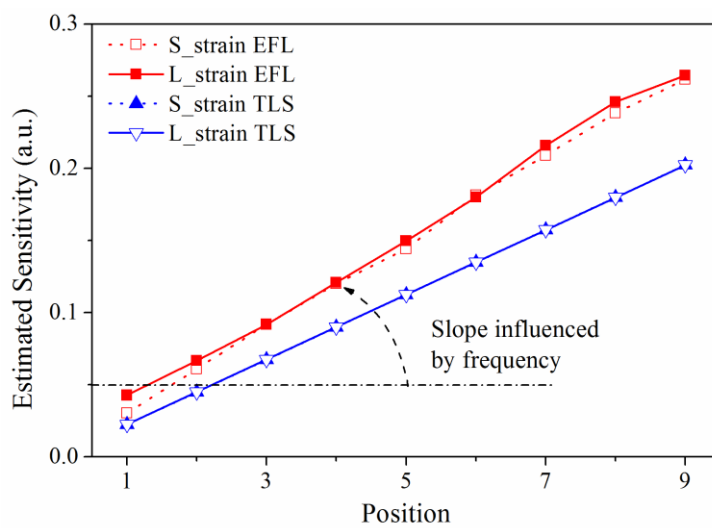
Figure 5.9. Comparison results of the effective estimated sensitivity between the EFL and the same PS-FBG demodulated by external independent TLS.
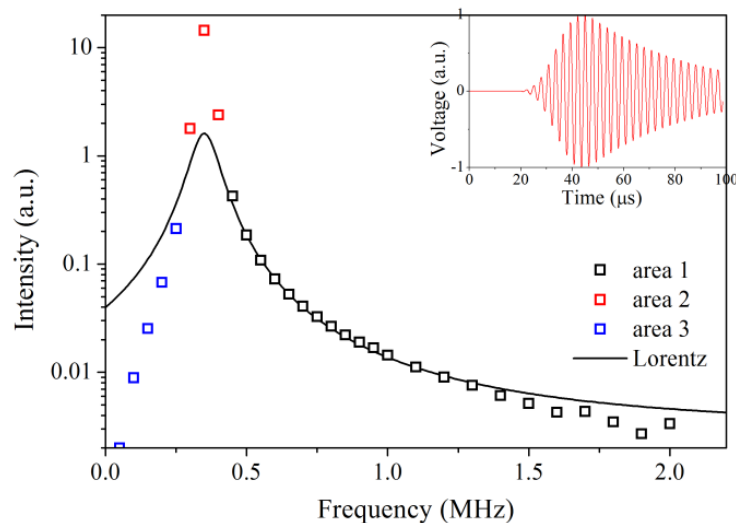
Figure 5.10. Intensity of the detected signals from the EFL to different frequencies shows Lorentz curve with resonance equal to the frequency of RO.

According to the above simulation and analysis, the ultrasonic response of the EFL resembles the behavior of the forced 1-DOF vibration with damping [115] to a certain extent. The resonance of the vibration model is the frequency of the RO of the EFL, and the force corresponds to the dynamic loss from the PS-FBG in the ring cavity. This result can be partially seen according to the equation of the EFL in reference [109]. We cite this Equation herein:

$$\frac{d^2\left(\delta M_g\right)}{dt^2}+2\alpha\frac{d\left(\delta M_g\right)}{dt}+\omega_0^2\delta M_g=0. \tag{5.5}$$

where ω_0 is the frequency of RO, α is the decay constant. Eq. 5.5 has similar format of 1-DOF vibration with damping. If the laser is disturbed by small and random vibrations, such as the case when the laser is in stable condition but with very small pump instability, the RHS of Eq. 5.5 is 0. In this case, the noise of the EFL shows peaks at RO [116]. When the ultrasonic loss in the ring cavity disturbs the EFL relative largely, 0 in the RHS of Eq. 5.5 is replaced by the function of the dynamic loss. Thus, the dynamic response of the system can be predicted from vibration view point. For example, when the input frequency is much larger than resonance, the dynamic response of this EFL shows same frequency as the input continuous wave. For another example, the response of the EFL to non-period ultrasonic signal is the convolution of EFL's impulse response and the format of the input signal. Furthermore, it also explains why the intensity of the detected signal has Lorentz relation to the frequency in Figure 5.10. We believe these results are universal in all the intensity-modulated EFL, which is a very helpful direction in the ultrasonic sensing application.

5.3   System Evaluation

5.3.1   *Characteristics of the EFL*

Figure 5.11(a) shows a number of spikes and damped ROs occurred in the experimental laser establishing process. The estimated parameters in the numerical model and the linear increasing pump power in the experiment cause the differences between the simulation results and the experimental results. Figure 5.11(b) shows the output voltage of the EFL in environmental quasi-steady-state conditions (small and low frequency temperature change). The output voltage is usually constant at about 0.32 V. When we were conducting this experiment, there was a 5 degree temperature fluctuation in the lab. Therefore this system can resistant at least 5 degree quasi-static change without feedback controller. However, sometimes burst signals with very similar and unique format were observed, as shown in the inset of Figure 5.11(b). They are caused by the mode hopping, we think. This is one problem in this EFL. Figure 5.11(c) shows the observed optical spectrum of the EFL. Lasing wavelength is around 1550 nm, matching to the Bragg wavelength of the PS-FBG. The output power

of this EFL is about -27 dBm (2 µW), which is much smaller than the pump power, meaning low efficiency of the EFL caused by the large insertion loss of the FBGs. However, it is essential for guaranteeing the ultrasonic detection, because single longitudinal mode oscillates when the ring cavity loss is large or pump power is small. Otherwise, more sidelobe longitudinal modes with large output power will oscillate due to the partial inhomogeneous broadening property of EDF, destructing the sensing ability of this EFL.
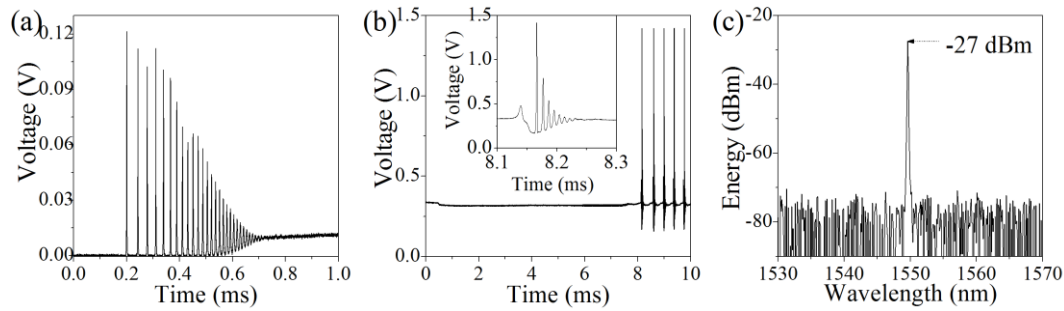
Figure 5.11. Characteristics of the EFL. (a) A number of spikes and damped ROs were observed in laser establishing process. (b) Stable DC output voltage in the quasi-steady-state condition with sometimes mode hopping signals. Inset shows a typical mode hopping signal in short time period. (c) Optical spectrum shows low efficiency of the EFL caused by large insertion loss.

5.3.2   *Response to Continuous Signals*

Figure 5.12(a) and 5.12(b) show the dynamic responses of the traditional PZT sensor and the EFL, respectively, when the input continuous sinusoidal signal has 1-MHz frequency and 5-V peak-to-peak voltage. Both sensors can detect ultrasonic wave. Figure 5.12 (c) shows the spectra of the detected signal from the EFL observed via ESA. In 1-MHz frequency, clear signal peaks are observed; however, the signal level has about 22 dB instability, caused by the uncontrollable initial longitudinal mode position and uneven slope of the PS-FBG around the peak area. Furthermore, small peaks are observed in about 6.8 MHz, caused by the longitudinal mode beating due to the partial inhomogeneous broadening property of the EDF. However, due to the very small energy, the lasing sidelobe longitudinal modes do not affect the sensing ability of the EFL, which can be ignored. In 2-MHz, very small higher order peaks are also shown, as predicted in simulation.
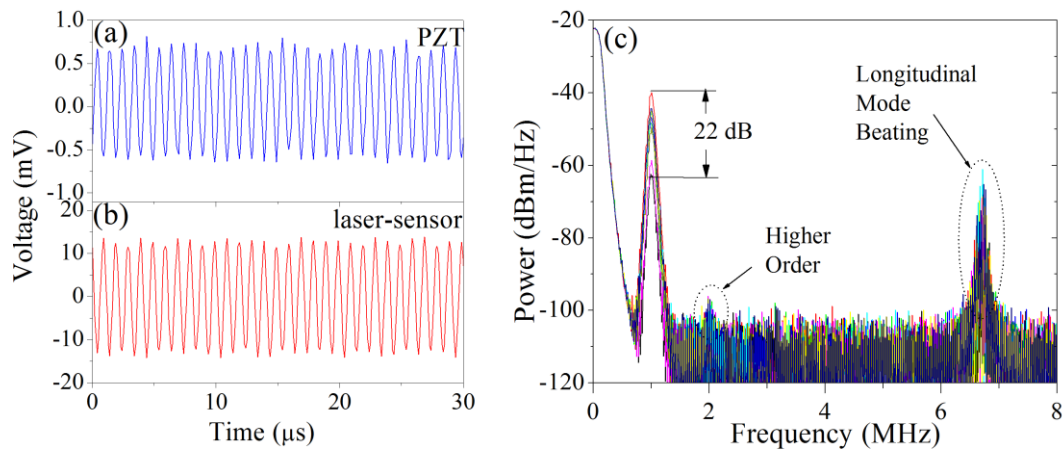
Figure 5.12. Typical dynamic response of (a) the traditional PZT sensor and (b) the EFL to continuous sinusoidal wave. (c) Spectra of the detected signals from the EFL.
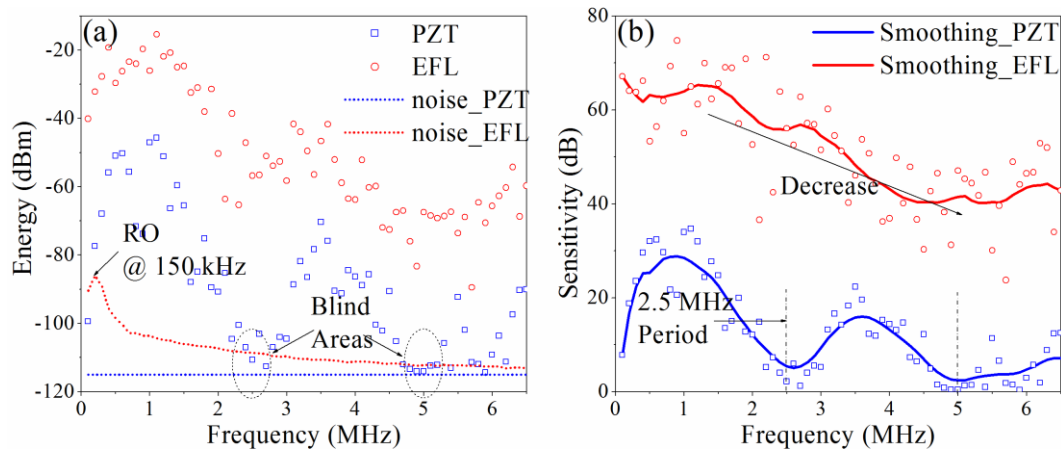
Figure 5.13. Response of the PZT and the EFL to every frequency. (a) Original data of detected energy and noise in the PZT and the EFL. (b) Sensitivity of the PZT and the EFL obtained after data process method.

For further analysis on the properties of the sensitivity and the bandwidth of the EFL, we changed the input frequency with 0.1-MHz step. Figure 5.13 shows the results from the EFL (red) and from the traditional PZT sensor (blue) when preamplifier is not connected after it. In Figure 5.13(a), the noise level detected from the PZT is lower than that from the EFL, and has equivalent value to every frequency. The electrical noise in the ESA perhaps is the main noise source in the results from the PZT. However, the noise in the EFL decreases with frequency increment, and resembles the Lorentz curve. The peak of the noise in EFL is at 150-kHz, which is the frequency of RO. According to Figure 5.13(a), both sensors have a broad bandwidth up to 6.5 MHz It is very high for applications of acousto-ultrasonic detection in NDT. The ultrasonic bandwidth is limited by the longitudinal mode beating of the EFL, and can be improved by using shorter laser cavity. In the traditional PZT sensor, blind areas exist around the frequency multiples of 2.5 MHz where the PZT cannot detect

109

ultrasonic waves. These blind areas greatly influence PZT's practical performance. However, the EFL detects every frequency ultrasonic signals.

The detected energies shown in Figure 5.13(a) are influenced by the piezoelectricity efficiency of the PZT actuator; thus data process should be done to obtain the correct sensitivity of the EFL. Thanks to the same piezoelectric coefficient in the same type of PZT actuator and PZT sensor, we can evaluate the sensitivity of the PZT [23]. Then, we use the energy detected from the EFL to subtract the influence from PZT actuator in order to evaluate the sensitivity of the EFL. These results are shown as open dots in Figure 5.13(b). Lastly, we use adjacent-averaging method with window of 10 to smooth the data, as the red line and the blue line for the EFL and the PZT in Fig. 13(b), respectively. Although the signal data from the EFL in Figure 5.13 were collected when they were in large level, the sensitivity of the EFL is larger than that of the PZT, even by considering the 22-dB amplitude instability of the EFL. The high sensitivity of the EFL is beneficial for the sensing distance and sensing accuracy, important for ultrasonic detection. Furthermore, both curves decrease with increase in frequency. However, 2.5-MHz periodic resonant property is shown in PZT rather than in EFL. The sensitivity of the EFL decreases about 27 dB gently, which has similar value to the decrease of the noise level in EFL shown in Figure 5.13(a). Although this measurement is not so precisely due to the influence from the propagating efficiency of Lamb wave in aluminum plate, the trend of the curve of the EFL is similar to area 3 shown in Figure 5.10. Therefore, we believe the sensitivity of the EFL does depend on the frequency as Lorentz function.

5.3.3 *Response to Burst Signals*

Then we evaluated the response of the EFL to burst signals. The input signal with 5-V peak-to-peak voltage has the same waveform as that used in simulation in section 4.5. Figure 5.14(a) shows the waveform detected by the traditional PZT sensor after 1024 times averaging. The dot line in Figure 5.14(a) shows the waveform detected by the PZT without averaging. Figure 5.14(b) shows the waveform detected by our previous PS-FBG balanced sensing system after 1024 times averaging. Figure 5.14(c) shows typical waveforms detected by this EFL when the ultrasonic wave amplitude is relatively large. Clearly, previous systems need amount data averaging with time-consuming for clear waveform presentation; only the EFL achieved real-time ultrasonic detection with good resolutions. All the detected signals have the same arrival time, which means that the ultrasonic detection ability of the EFL is derived from the Bragg wavelength shift rather than the polarimetric heterodyning [36]. If the detected signals are caused by the polarization change of the optical fiber, the EFL will be more sensitive to the ultrasonic wave propagated in the transverse direction, which is caused by the reflection of the aluminum plate edges. This will delay the arrival time of the detected wave. The waveform in Figure 5.14(c) fits the simulation result shown in Figure 5.7 very well, showing small waveform deformation and low frequency vibration behind the wave envelop.

By performing Fourier transform, we obtained the corresponding spectra of the detected waveforms, as shown in Figure 5.14(d). At about 1 MHz, there are clear ultrasonic signals. In the EFL, there are also low-frequency peaks with relative large energy caused by RO and higher order small signals as we predicted in simulation. The detected ultrasonic signal level and the noise level of the EFL and the PS-FBG balanced sensing system are marked. After recalling the sensitivity of the PS-FBG balanced sensing system of ε_{min} = 9 nε/Hz$^{1/2}$ and considering the 1024 times averaging, the sensitivity of the EFL to the waveform in Figure 5.14 is evaluated as ε_{min} =5.6 pε/Hz$^{1/2}$. If adding the influence of instability of the amplitude, the sensitivity of the EFL varies from 0.9 nε/Hz$^{1/2}$ to 5.6 pε/Hz$^{1/2}$ in 1-MHz frequency. This evaluation is just a reference, because the sensitivity of the ultrasonic detection is related to the frequency, influenced by the attachment condition and so on. We then applied a high-pass filter with cut-off frequency of 200 kHz to the detected signal from EFL. The recovered signal shown in Figure 5.14(e) resembles the waveform in Figure 5.14(b), also resembles the results in Figure 5.8. It demonstrates the practice of this data process method.
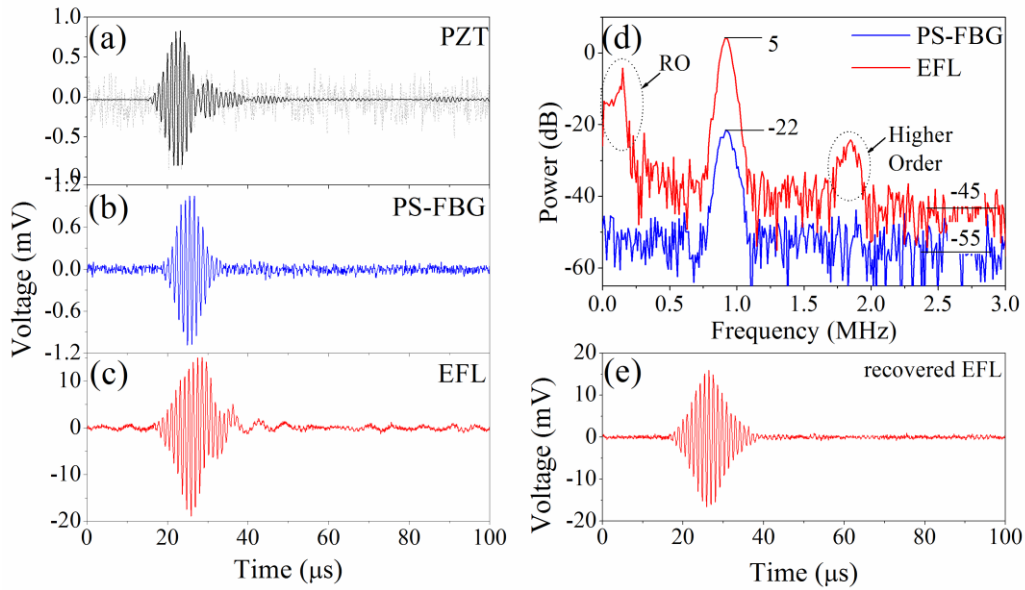
Figure 5.14. (a) Waveform detected by the PZT after 1024 times averaging. Dot line shows the detected signal without averaging. (b) Waveform detected by the PS-FBG balanced sensing system after 1024 times averaging. (c) Waveform detected by the EFL in real time. (d) Corresponding spectra. (e) Recovered waveform after high-pass filter detected by the EFL.

5.4   Application to Evaluation of Impact Damage

Due to the very unique and attracting characteristics in laser-sensor system, we proposed a possible application of this system for evaluation of impact damage in CFRP laminate by acousto-ultrasonic method. Figure 5.15 shows the experimental setup of acousto-ultrasonic method for impact detection. The specimen was CFRP

laminate with dimension of $20\times20\times0.3$ cm^3 (L$\times$W$\times$H). The CFRP laminate was fixed on an impact machine by iron frame, and about 15-J impact energy was applied to the middle of the CFRP laminate.
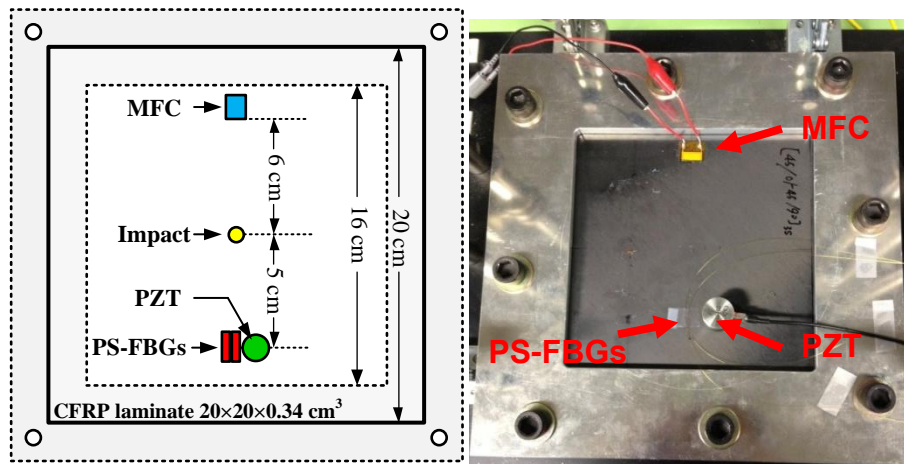
Figure 5.15. Experimental setup of acousto-ultrasonic method for impact damage detection in CFRP laminate.

6-cm away from the impact position, a MFC with length of 6 mm was used to generate ultrasonic wave, driven by FG with output peak-to-peak voltage of 5 V. The input signals had different waveforms: three cycles sinusoidal wave with Hamming window had middle frequency of about 300 kHz; ten cycles sinusoidal wave with Hamming window had middle frequency of about 1 MHz.

5-cm away from the impact position, two PS-FBGs were glued, facing to the MFC and impact point in line. PS-FBG3 was used in the laser-sensor system, and the PS-FBG2 was used in our previous PS-FBG balanced sensing system as a reference. The system setup of the PS-FBG balanced sensing system was the same as that used in our previous research. Furthermore, the N-PZT sensor was also glued near to the PS-FBG sensors for providing reference.

All the sensors detected the ultrasonic waves before and after the impact. By comparing the waveform changes, the impact damage was monitored and evaluated.

Figure 5.16 shows the case when low-frequency input signals were applied in the acousto-ultrasonic detection. Figure 5.16(a) is the input waveform; Figure 5.16(b) and (c) are the waveforms detected by the PZT sensor and the PS-FBG balanced sensing system, respectively. Although some waveform changes occurred after the impact was applied to the CFRP laminate, the change was very small, marked as the dot circles in Figure 5.16, leading to the difficulty of damage judgment.
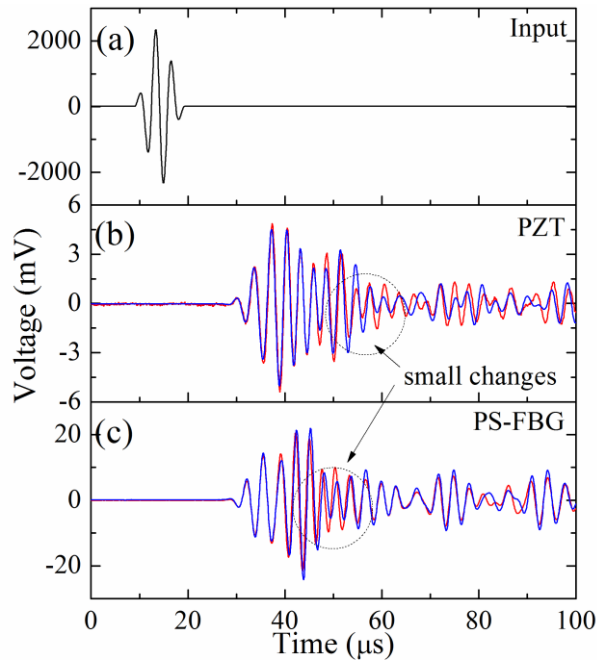
Figure 5.16. Detected waveforms when the input signal has relative low frequency. Red curves and blue curves are the waveforms before and after the impact, respectively.
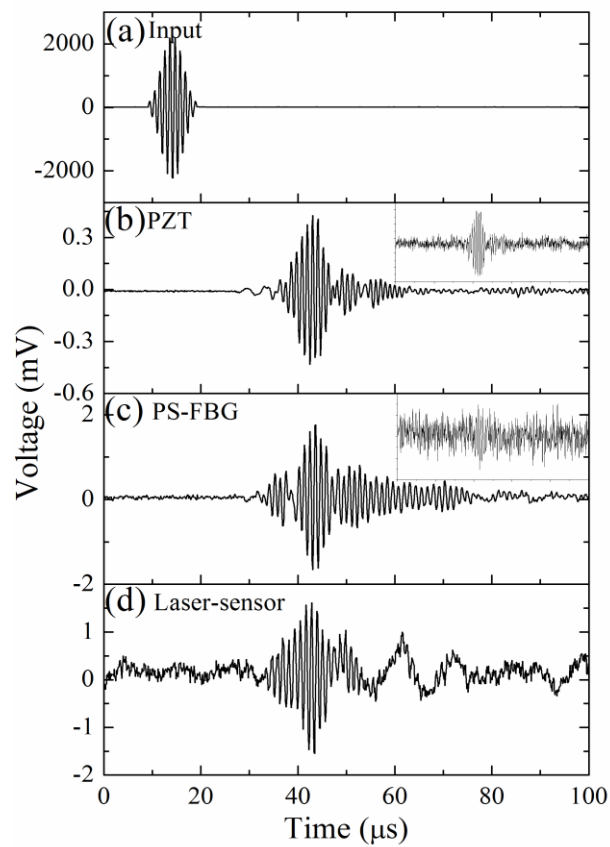
Figure 5.17. Waveforms before impact damage obtained when the input signal has high frequency of about 1 MHz.

113

Therefore, we alternated the input signal to that with high frequency, hoping that the resolution can be enhanced. Figure 5.17 shows the waveforms in this experiment. Figure 5.17 (a) shows the input signal; Figure 5.17 (b), (c) and (d) show the waveforms before impact detected by the PZT sensor, the PS-FBG balanced sensing system and the laser-sensor system, respectively. The waveforms detected by the PZT sensor and the PS-FBG balanced sensing system were obtained after 1024 times averaging for noise reduction. The SNR of the waveforms detected by the PZT and the PS-FBG balanced sensing system are very low, as shown in the insets of Figure 5.17, leading to large analysis mistakes. However, the waveform obtained by our novel laser-sensor system in real time (without averaging) is relative clear. As we mentioned before, the input signal had peak-to-peak voltage of 5 V which is very low, our sensing system shows very high sensitivity compared to other traditional techniques.
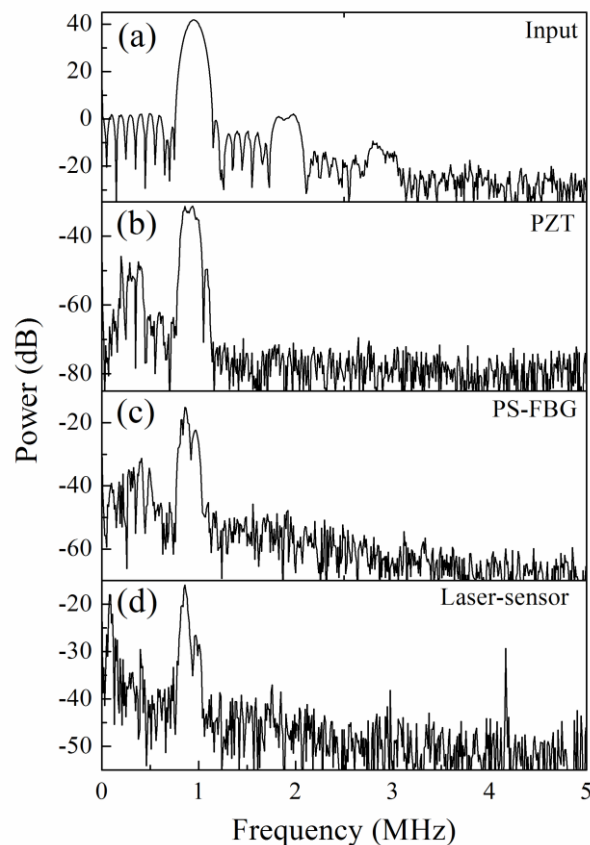
Figure 5.18. Corresponding spectra.

Then, we applied FFT to the waveforms shown in Figure 5.17. Figure 5.18 shows the corresponding results. The input single has frequency range mainly from 0.7 MHz to 1.2 MHz. The waveforms detected by PZT and PS-FBG balanced sensing system also have frequency components in this range. Around 85-kHz low frequency range, there are several peaks, explained as the RO in the EFL. It obviously influences our waveform analysis. e.g., the waveform detected by our laser-sensor system is different to that detected by PS-FBG balanced sensing system. Thus, we need to filter out these

unnecessary frequency components. Furthermore, in the frequency of 4.2 MHz, there is also a peak. It does not fit the frequency of the longitudinal mode beating, which may be caused by polarization mode beating when we did not perfectly adjust the polarization status of the fiber by those two PCs. However, the exact reason is unknown. It is also better to be removed by frequency-filter.
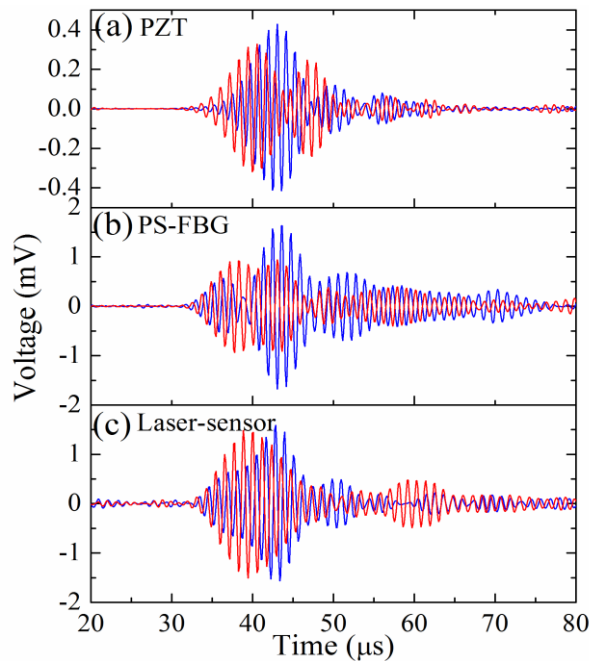
Figure 5.19. Waveforms detected by three different sensors before (red curve) and after (blue curve) the impact damage.

According to the spectrum analysis, we applied digital band-pass filter from 0.7 MHz to 1.2 MHz to all the detected signals. Figure 5.19 shows the waveforms detected before and after the damage through data process. Compared to the results shown in Figure 5.16, the waveform changes are very obvious when high frequency input signals were used. This phenomenon can be explained by high resolution in the case of high-frequency wave because high frequency corresponds to short wavelength. The other possible reason is that in high frequency range, the Lamb wave has more modes. They are easily changed when the condition of propagation media changes, e.g. the impact damage changes the CFRP laminate in our case. If we perform Hilbert transform to the detected signals, we can see the amplitude peak change. For example, the amplitude peak of the waveforms detected by laser-sensor system change from 39.5 μs to 43.1 μs, as shown in Figure 5.20. This phenomenon exists in all the sensors, which may has possibility to reflect the damage level caused by the impact. In order to verify the damage in the CFRP laminate, we used A-scan to evaluate the specimen. The results fit the experimental results very well.

This data process method is based on waveform analysis rather than amplitude analysis. Thus, the instability of the detected amplitude in the laser-sensor system

does not have influence to the analytic results. Therefore, there are practical applications of this sensing system.
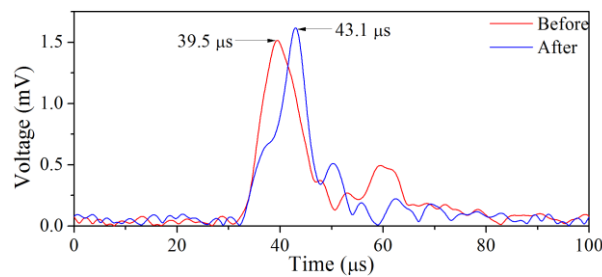
Figure 5.20. Hilbert transform results of the waveforms detected by laser-sensor system show amplitude peak change.

In this research, we proposed a novel ultrasonic optical fiber sensing system with high sensitivity and broad bandwidth. This laser-sensor system was based on an EFL with an inbuilt PS-FBG sensor. The PS-FBG sensor had very short effective grating length and an ultra-steep peak area slope, thus the sensitivity of this sensing system is very high. Because the lasing wavelength of the EFL was always in the FWHM of the PS-FBG, this laser-sensor system can self-adjust to resist both environmental temperature changes and quasi-static strain changes. We proposed and simulated the dynamic properties of the laser-sensor system based on two level model of EDFA in three different conditions, including quasi-static change, continuous ultrasonic wave and burst ultrasonic wave. Then, we demonstrated that the detectable ultrasonic bandwidth by the laser-sensor system was nearly 7 MHz. Furthermore, this laser-sensor system had a better ultrasonic response. All the experimental results fit the simulation results well. Due to these advantages, we applied this laser-sensor system to acousto-ultrasonic detection for evaluation of impact damages in CFRP laminate. The experimental results show that the laser-sensor system can detect ultrasonic wave with very high frequency in real time and keeps the waveform reliability via certain data process method. It makes the judgment of impact damage easier. It shows large practical potentials in this application. On the other hand, the research on the dynamic properties of the EFL is also useful for the study in the field of optical fiber laser. For example, by improving the theoretical model, it perhaps can explain the intensity detection reported in reference [117]. Also, the author thinks the dynamic response of the EFL is the real reason for ultrasonic detection in reference [98] rather than the nonlinear property of the EDF.

Lastly, we proposed several potential improved ways to this laser-sensor system. Reducing the laser cavity is the most efficient way to make the EFL more stable, it also can enlarge the dynamic range of the laser-sensor system. We also can use PS-FBG with narrower FWHM; however, this kind of PS-FBG may be difficult to be manufactured. Furthermore, data process method also should be improved.

6 CONCLUSIONS

In this dissertation, PS-FBG sensor is proposed and researched for ultrasonic SHM of composites. Based on the PS-FBG, three novel sensing systems are proposed for solving certain problems in different applications. Acousto-ultrasonic detection and AE detection are used to monitor the health state of CFRP laminates. This chapter summarizes the researching works, compares different sensing systems, concludes the contribution of this dissertation, and recommends future works.

6.1 Summary and Comparison

Firstly, PS-FBG is proposed for ultrasonic SHM of composites. Due to the phase shift in the middle of the grating area, it has short effective grating length and steep slope in the peak area, leading to the positive proportion of the sensitivity and bandwidth. In order to research these phenomena, we simulate the response of PS-FBG to longitudinal ultrasonic wave according to transfer matrix method. The simulation results show that PS-FBG is a very suitable for ultrasonic detection.

Then, we researched two properties of PS-FBG. Unlike traditional PZT sensor which has omni-directional sensitivity, the sensitivity distribution properties of PS-FBG are complex. The distance, angle, and other parameters of the PS-FBG not only determine the amplitude but also waveforms, spectra and CWT results. Additionally, we also researched the influence of different attachment methods, which influences the ultrasonic sensitivity, strain-sensitivity, birefringence, removable property, and arrival time of the wave. Therefore, different SHM or NDT methods have their most suitable attachment method.

Then, cascaded PS-FBGs sensing system, based on power detection, is proposed for demodulation of the quick Bragg wavelength shift caused by ultrasonic wave. The output power of ASE light source is changed due to the vibration of the overlapping area between PS-FBG filter and PS-FBG sensor. Because of the properties of the PS-FBG, the sensitivity and bandwidth of this system is improved. This sensing system can detect ultrasonic Lamb wave in composites without averaging, and discriminate different modes with relative high accuracy. It also can detect impact signals with low energy or from long distance; however, wave deformations should be paid attention to when the signals is large or close to the sensor. Because it uses broadband light source, multiplexing ability is achieved when dozens PS-FBG with different Bragg wavelengths are connected after WDM component, such as AWG filter. Due to these characteristics, it is most suitable in acousto-ultrasonic detections, and the total cost of this system is low.

The PS-FBG balanced sensing system, based on edge filter detection, improves the sensitivity further by using TLS and balanced sensing technique, compared to the first sensing system. The TLS has low noise level, and the balanced sensing technique can remove the DC signal, double the AC signal and reject laser intensity noise when the wavelength of the TLS is precisely controlled. On the other hand, this balanced

sensing technique sacrifices the multiplexing ability, and the cost of this system is relative high because of the expensive TLS. Thus, this PS-FBG balanced sensing system is most suitable in AE detection, where high sensitivity and broad bandwidth is the primary and fundamental requirements owing to the certain AE signal with high frequency and small energy, such as transverse cracks in CFRP laminate. We use this sensing system in AE detection in CFRP laminates in tensile test and three point bending test. In the first tensile test, after simple data process methods for noise reduction, we verify the Kaiser Effect, discriminate transverse crack and fiber breaking according to the cumulative AE hits or energy distribution. In the second tensile test, Kaiser Effect and Felicity Effect are also demonstrated. Furthermore, 6 different waveform types are discussed and try to relate to different damage types in angle-ply and cross-ply CFRP laminates. In three point bending test, we analyze the waveforms and the corresponding CWT results of the AE signals from transverse cracks. Furthermore, we demonstrate its position identification ability via data process method and different arrival time. All of these results are compared to the results from traditional PZT sensors, and show high practical potential of this sensing system in AE detections.

As for the third laser-sensor system, the highest sensitivity and the broadest bandwidth were accomplished by using EFL to demodulate the Bragg wavelength shift. A dynamic response of the laser-sensor system to ultrasonic wave is simulated based on two-level mode. Three different conditions are considered, including continuous sinusoidal wave, burst ultrasonic wave and quasi-static change. The simulation results fit the experimental results very well. The laser-sensor system shows ultrasonic bandwidth of about 6.5 MHz, and better response property to ultrasonic wave than traditional PZT sensor, albeit with certain waveform deformation due to the RO in EFL. However, the waveform deformation can be removed by digital high pass filter for recovering the actual waveform. This system has low multiplexing ability because one EDFA only can connect one PS-FBG sensor. Due to the inability of multiplexing and medium cost of the EDFA, the cost of this sensing system is medium among these three systems. Furthermore, unlike the previous two sensing system which needs controller to stable the position of PS-FBG filter or TLS for practical application, this sensing system has robustness to temperature change or quasi-static strain change, although the amplitudes of the detected waveform are not stable. This is because the wavelength of the laser is self-adjusted by the PS-FBG. In other words, the PS-FBG sensor is always illuminated by the EFL to realize edge filter detection. Therefore, this sensing system is most suitable to detect weak-energy and high-frequency signal in harsh environment, such as acousto-ultrasonic detection when airplane is working. In lab, we have successfully applied this system in acousto-ultrasonic detection in CFRP laminate for impact damage evaluation.

In conclusion, any of these three sensing systems has unique characteristics, and has its most suitable application area. Table 6 briefly shows the comparisons among three sensing systems, including the aspects of principle, sensitivity, bandwidth, multiplexing, robustness, deformation, cost and application.

Table 6. Comparison among three sensing systems.

Systems	Principle	Sensitivity	Bandwidth	Multiplexing	Robustness	Deformation	Cost	Applications
Cascaded PS-FBGs Sensing System	Power detection	High	Broad	Yes	Needs controller	No (only occurs in large signal)	Low	Acousto-ultrasonic detection
PS-FBG Balanced Sensing System	Edge filter & balanced detection	Very high	Very Broad	No	Needs controller	No (only occurs in large signal)	High	AE detection
Fiber Ring Laser Sensing System with Inbuilt PS-FBG	Edge filter detection & self-adjustment	Ultra-high	Ultra-broad	No	Self-controllable	Yes	Medium	Acousto-ultrasonic in harsh environment

6.2   Contributions

The major contributions of this dissertation include:

- For the first time, PS-FBG is used in ultrasonic SHM of composites.
- The response of PS-FBG to longitudinal ultrasonic wave is simulated by transfer matrix method.
- The sensitivity distribution properties and related attachment methods of PS-FBG are systematically researched, which directs and helps study on other kinds of ultrasonic fiber sensors for SHM.
- A cascaded PS-FBGs sensing system with high sensitivity, broad bandwidth and multiplexing ability is proposed and demonstrated. It is successfully used in real-time acousto-ultrasonic detection in composites with mode discrimination ability.
- A PS-FBG balanced sensing system is proposed and demonstrated. Frequency-noise-limitation detection is achieved by this simple method.
- For the first time, a fiber optical sensing system detects AE signals with small energy and high frequency in composites. In this relative novel academic field, three basic experiments are conducted. The Kaiser Effect, damage discrimination and position identification were achieved according to the data detected by fiber optical sensing system. The transverse crack AE signals were as well analyzed for the first time.
- An EFL sensing system with inbuilt PS-FBG is proposed and demonstrated. For the first time, an optical fiber sensing system with ultra-high sensitivity, ultra-broad bandwidth and robustness to temperature change is achieved simultaneously.
- A mode of EFL with very few longitudinal modes is proposed to study the dynamic responds of the EFL. In this study, the dynamic response of the EFL is treated as positive effect rather than negative effect; and the optical dynamic phenomenon is explained by a mechanic viewpoint.

6.3   Recommendation of Future Works

Based on the research that has been done in this dissertation, future works are recommended here. We believe the following work could make higher performance and better practical applications to these sensing systems.

In the previous simulation, the ultrasonic wave is assumed as simple longitudinal wave. However, complicated Lamb wave is much normal in practices. Therefore, simulation of the response of PS-FBG to Lamb wave can reflect its behavior in ultrasonic SHM more precisely. Researchers always use LS-DYNA to simulate Lamb wave in composites. The program running time, which is always long, is related to the size of the mesh and the dimension of the composite. However, the length of each fiber section is very short for guaranteeing the accuracy of the simulation of PS-FBG. Thus, I believe that the method to balance or solve this conflict is probably the key to make the simulation successfully.

There exists a best overlapping position of PS-FBG filter and PS-FBG sensor in the cascaded PS-FBGs sensing system. However, the relation between the overlapping position and the sensitivity of this system has not been researched until now, because we still cannot precisely stable the Bragg wavelength of the PS-FBG. Furthermore, the method to stable the overlapping position is another issue which needs to be considered.

In the PS-FBG balanced sensing system, the feedback controller should be optimized. Furthermore, in the AE detections, the data process method is post-processing, i.e., we do the data process after we collect the data. It is not the best for AE detection because it needs real-time detection. Thus, how to improve the data process method and make the data acquisition system smarter is what we should think about later.

We have conducted tensile test and three point bending test until now. More AE detection experiment should be done for researching the possibility of using FOS as an alternative of traditional PZT sensor in this novel field. Part of this work has been continued by Mr. Yu. He researched the Extensional/Flexural ratio of the AE signal detected by PS-FBG for discriminating delamination in CFRP laminate. Furthermore, we have begun to conduct AE detection by the PS-FBG balanced sensing system on other novel composite materials, such as ceramic matrix composite.

Although the advantages in the third sensing system are very attracting, the disadvantages are also very apparent, such as the waveform deformation, amplitude instability and mode hopping. The former two problems can be solved by data process method, such as inverse calculation or deconvolution. However the mode hopping problem does affect the practical performance of the system. We should improve this system or use other method to solve it.

The other application areas of these three proposed ultrasonic fiber optical sensing systems should be considered. For example, the PS-FBG balanced sensing system could be used in leakage detection in long distance pipeline. Moreover, ultrasonic SHM of composites requires many advanced sensing techniques for guaranteeing its safety. Therefore, different sensing techniques should be designed, aiming to specific problems.

APPENDICES

A. Core Program of FBG Simulation

```
% clear all
% clc

% definition of injection light
lamda1=1548e-9;                               % beginning wavelength
lamda2=1552e-9;                               % ending wavelength
N1=1001;                                      % wavelength sampling
lamda=linspace(lamda1,lamda2,N1);            % vector of wavelength

% definition of the parameters in the fiber
C=3e8;                                        % speed of the light
neff=1.45;                                    % effective refractive index
delta_N=4e-4;                                 % initial index change
v=1;                                          % fringe visibility
LamdaB=1550e-9;                               % Bragg wavelength
%p=5.35e-7;                                   % period
p=LamdaB/2/neff;                              % period

% definition of the influences from ultrasonic wave
P11=0.12;                                     % stress-optic coefficient
1
P12=0.275;                                    % stress-optic coefficient
2
vv=0.17;                                      % Poisson ratio
Ws=2*pi;                                      % angular frequency
t=0:0.02:1;                                   % time vector

% definition of the length of fiber
L=0.005;                                      % length of the fiber
N2=1000;                                      % number of the sections
l=L/N2;                                       % length of each section
z1=linspace(l,L,N2);                          % vector of the section

% definition of the length of the ultrasonic wave
ratio=1;                                      % length ration
lamda_S=L*ratio;                              % ultrasonic wavelength
em=100e-6;                                    % displacement amplitude
```

```matlab
delta_phase=pi;                                    % phace shift
pp_1=exp(-1i*delta_phase/2);
pp_2=exp(1i*delta_phase/2);
Matrix_phase=[pp_1,0;0,pp_2];                      % phace shift matrix

% dynamic simulation (time)
for ii=1:length(t)

        % Elasto-Optic Effect
        delta_N2=-(neff^3/2)*(P12-vv*(P11+P12))*em.*cos(2*pi.*z1/lamda_S-
Ws*t(ii));                                         % index change
        Neff=neff+delta_N2;                        % actual effective index

        % Geometric Effect, solved by Newton-Raphson method
        for j=1:N2
                syms x fx gx;
                fx=x+em*lamda_S*sin(2*pi*x/lamda_S-
Ws*t(ii))/2/pi+em*lamda_S*sin(Ws*t(ii))/2/pi-z1(j);
                                % transcendental equation

                gx=diff(fx,'x');                   % derivation
                x=z1(j);                           % initial
                k=1;                               % cycle counter
                fx1=subs(fx,'x',x);                % substitution

                while abs(subs(fx,'x',x))>1e-12;   % accuracy controller
                        x=x-subs(fx,'x',x)/subs(gx,'x',x);   % calculate and iteration
                        k=k+1;                     % countering
                        if k>100;                  % stop cycle
                                break;
                        end
                end
                z0(j)=x;                           % position change
        end

        P=ones(1,N2).*z0(1);                       % initial section vector
        for i=2:N2
                P(i)=z0(i)-z0(i-1);                % actual section length
        end
        pp=l*p./P;                                 % actual period

        lamda_B=2*(Neff).*pp;                      % the Bragg wavelength
```

```matlab
for j=1:N1
    Matrix=[1,0;0,1];                          % initial transfer matrix
    for k=1:N2

        %the caculated parameters
        dc=2*pi*delta_N/lamda(j);              % ac coupling coefficient
        ac=pi*v*delta_N/lamda(j);              % dc coupling coefficient
        sigma=dc+2*pi*Neff(k)*(1/lamda(j)-1/lamda_B(k));
                                    % general dc self-coupling coefficient
        gama=sqrt(ac^2-sigma^2);
        A=l*gama;

        T11=cosh(A)-1i*(sigma/gama)*sinh(A);
                                    %   Bragg   propagation
matrix
        T12=-1i*(ac/gama)*sinh(A);
        T21=1i*(ac/gama)*sinh(A);
        T22=cosh(A)+1i*(sigma/gama)*sinh(A);
        matrix=[T11,T12;T21,T22];

        Matrix=Matrix*matrix;                  % time matrix

        % phase shift
        if k== N2/2
            Matrix=Matrix*Matrix_phase;        % time phase shift
        end

    end

    TT11=Matrix(1);                            % matrix elements
    TT12=Matrix(3);
    TT21=Matrix(2);
    TT22=Matrix(4);

    Reflect=TT21/TT11;                         % reflection
    Reflectivity=(abs(Reflect))^2;
    rr(j)=Reflectivity;                        % reflectivity
end

plot(lamda,rr);                                % plot figure
[Y,I]=max(rr);                                 % peak position
value(ii)=Y;                                   % reflectivity in peak
position(ii)=I;                                % Bragg wavelength
axis([1550e-9 1560e-9 0 1])                    % axis
```

```
        pause(0.5)                                      % pause
        mov(ii)=getframe;                               % movie frame
end

movie2avi(mov,'dynamic.avi', 'compression', 'None');        % movie maker
```

B. Core Program of FFT and CWT

```matlab
% clear
% clc

y1=wave(1:1024);                        % input wave controller
F=10e6;                                 % sampling frequency
T=1/F;                                  % sample time
L=length(y1);                           % length of signal
t=(0:L-1)*T;                            % time vector

NFFT=2^nextpow2(L);                     % 2^P >= abs(L)
Y1=fft(y1,NFFT);                        % spectrum after fft
nfft=NFFT/2;                            % Nyquist law
FF=F/2*linspace(0,1,nfft);             % Nyquist frequency X axis
Y2=Y1(1:nfft);                          % single side band

LPF=10e3;                               % low-pass filter
for i=1:nfft                            % filter out the low frequency
   if FF(i)<=LPF
       Y2(i)=0;
   end
end

HPF=2e6;                                % high-pass filter
for i=1:nfft                            % filter out the high frequency
   if FF(i)>=HPF
       Y2(i)=0;
   end
end

% figure
% plot(FF,abs(Y2))                      % spectrum after filter

y2=2*ifft(Y2,NFFT);                     % ifft, remember times 2
y3=real(y2(1:L));                       % real part of the ifft
% figure
% plot(t,y3)                            % waveform after filter

wname='cmor1-1.5';                      % mother wavelet

fmin=300e3;                             % sweep frequency range
fstep=5e3;
fmax=2000e3;
```

126

```matlab
f=fmin:fstep:fmax;                          % sweep frequency vector

FREQ=centfrq(wname);                        % M-wavelet central
scal=FREQ*F./f;                             % change frequency to scale
result=cwt(y3,scal,wname);                  % wavelet transform
A1=abs(result');                            % abs part of the result
A2=real(result');                           % real part of the result
A3=imag(result');                           % image part of the result

figure
contourf(f,t,A1,10,'linestyle','non');      % plot the figure
xlabel('Frequency','fontsize',10)
ylabel('Time','fontsize',10)
colorbar
```

C. Core Program of Erbium Doped Fiber Ring Laser

```
% clear
% clc
Tic                                           % time counter begin

global Lamda h c T up                         % global parameter defination

up=0;                                         % monitoring upper level emission

Lamda=1550e-9;                                % Bragg/laser wavelength
h=6.626e-34;                                  % plank constant
c=3e8;                                        % light speed

n=1.456;                                      % index
L=28;                                         % cavity length
T=n*L/c;                                      % round trip time

freq=1e6;                                     % ultrasonic frequency
shift=10e-15;                                 % Bragg wavelength shift

sampling1=10e6;                               % signal time domain defination
Span1=2e-5;
sampling2=20e6;
Span2=1e-5;
sampling3=10e6;
Span3=5e-5;


time1=0:1/sampling1:Span1;                    % time vector definition
time2=Span1+(1/sampling2:1/sampling2:Span2);
time3=Span1+Span2+(1/sampling3:1/sampling3:Span3);
time=[time1 time2 time3];

Hamming=0.54-0.46*cos(linspace(0,2*pi,length(time2)));   % Hamming window

m_lamda1=Lamda*ones(1,length(time1));         % Bragg wavelength vector
m_lamda2=Lamda+shift*sin(2*pi*freq*time2).*Hamming;
m_lamda3=Lamda*ones(1,length(time3));
m_lamda=[m_lamda1 m_lamda2 m_lamda3];

% figure
% plot(time,m_lamda)
```

```matlab
d_lamda=0.8e-12;                                  % FWHM of the filter
LMS=6e-14;                                        % longi-mode spacing=lamda^2/n/L
lamda=1550e-9-3e-12-1*LMS/1000:LMS:1550e-9+3e-12-1*LMS/1000;
                                                  % matrix of filter
for i=1:length(time)
    X(i,:)=1*exp(-((lamda-m_lamda(i))/d_lamda).^2);
end

% figure
% contourf(lamda,time,X,100,'linestyle','non')

m=length(lamda);                                  % number of longitudinal modes
span=[0 Span1+Span2+Span3];                        % span definition
% initial=zeros(1,m+1)';                          % input initial values

[t,y]=ode45(@(t,y) EDFAto(t,y,time,X,m), span, initial);    % Runger-Kutta method

for i=1:length(t)                                 % amount emission photons
    amount(i)=sum(y(i,1:m));
end

Pout=amount*h*c/Lamda/T;                          % in-cavity power

figure                                            % dynamic power
plot(t,Pout);
% figure
% plot(t,y(:,m+1))

strain=shift*1e12/1.2                             % output corresponding parameters
temperature=shift*1e12/10
sensitivity=(max(Pout)-min(Pout))/Pout(1)

% figure                                          % final output specrum
% plot(lamda,y(length(T),1:m))
toc                                               % time counter over


function dy=EDFAto(t,y,time,X,m)                  % function of the EDFA

global Lamda h c T up                             % redefinition of the global parameters

for i=1:m
    x(i)=interp1(time,X(:,i),t,'pchip');          % Interpolate the filter data set at time t
end
```

129

```
pp=0.225;                                    % pump power
dy=zeros(m+1,1);                             % a column vector

p=2e24;                                      % erbium ion density
s=8.08e-12;                                  % cross sectional area
l=3.6;                                       % erbium fiber length
T0=10.2e-3;                                  % upper state lifetime
a=10;                                        % total loss
P=pp*(Lamda/h/c);                            % input pump power

ve=3.7;                                      % emission coefficient at signal wavelength
ae=3;                                        % absorption coefficient at signal wavelength
ap=4.64;                                     % absorption coefficient at pump wavelength

gp=-ap*(1-y(m+1));                           % length averaged pump absorption coefficient
gg=(ve+ae)*y(m+1)-ae;                        % length averaged gain coefficient for signal
Ag=(exp(gg*l)-1)/gg/l;                       % ASE amplification factor

R=4*l*ve*y(m+1)*m*(Ag-1)/T;                  % influence from ASE

dy(1:m)=y(1:m).*((x')*exp(gg*l-a)-1)/T+2*ve*l*y(m+1)*Ag/T;
                                             % differential equation for emission photons

up=sum(y(1:m));                              % summation of the emission photons
emission=up*(1-exp(-gg*l))/T;                % influence from ASE

dy(m+1)=(P*(1-exp(gp*l))-p*s*l*y(m+1)/T0-emission-R)/p/s/l;
                                             % differential equation for upper level atoms
```

BIBLIOGRAPHY

[1]   Y. Mizutani*, et al.*, "Fracture mechanism characterization of cross-ply carbon-fiber composites using acoustic emission analysis," *NDT & E International,* vol. 33, pp. 101-110, 2000.

[2]   N. Takeda*, et al.*, "Experimental characterization of microscopic damage progress in quasi-isotropic CFRP laminates: effect of interlaminar-toughened layers," *Advanced Composite Materials,* vol. 7, pp. 183-199, 1998.

[3]   M. Eaton*, et al.*, "Damage in carbon fibre composites: The discrimination of acoustic emission signals using frequency," *Journal of Acoustic Emission,* vol. 25, pp. 140-148, 2007.

[4]   A. Marec*, et al.*, "Damage characterization of polymer-based composite materials: Multivariable analysis and wavelet transform for clustering acoustic emission data," *Mechanical Systems and Signal Processing,* vol. 22, pp. 1441-1464, 2008.

[5]   R. Gutkin*, et al.*, "On acoustic emission for failure investigation in CFRP: Pattern recognition and peak frequency analyses," *Mechanical Systems and Signal Processing,* vol. 25, pp. 1393-1407, 2011.

[6]   D. C. Betz*, et al.*, "Acousto-ultrasonic sensing using fiber Bragg gratings," *Smart Materials and Structures,* vol. 12, p. 122, 2003.

[7]   J. R. Lee*, et al.*, "Apodized fibre Bragg grating acousto-ultrasonic sensor under arbitrary strain using dual Fabry–Perot filters," *Journal of Optics A: Pure and Applied Optics,* vol. 9, p. 95, 2007.

[8]   G. Wild and S. Hinckley, "Acousto-ultrasonic optical fiber sensors: overview and state-of-the-art," *IEEE Sensors Journal,* vol. 8, pp. 1184-1193, 2008.

[9]   M. A. Hamstad, "A review: acoustic emission, a tool for composite-materials studies," *Experimental Mechanics,* vol. 26, pp. 7-13, 1986.

[10]   W. Prosser*, et al.*, "Advanced waveform-based acoustic emission detection of matrix cracking in composites," *Materials Evaluation,* vol. 53, pp. 1052-1058, 1995.

[11]   C. Scruby, "An introduction to acoustic emission," *Journal of Physics E: Scientific Instruments,* vol. 20, pp. 946-953, 1987.

[12]   M. R. Gorman, "Plate wave acoustic emission," *the Journal of the Acoustical Society of America,* vol. 90, pp. 358-364, 1991.

[13]   M. Fuwa*, et al.*, "Acoustic emission during cyclic loading of carbon-fibre-reinforced plastics," *Journal of Physics D: Applied Physics,* vol. 8, pp. 1460-1471, 2001.

[14]   X. Li, "A brief review: acoustic emission method for tool wear monitoring during turning," *International Journal of Machine Tools and Manufacture,* vol. 42, pp. 157-165, 2002.

[15]   M. Gorman and S. Ziola, "Plate waves produced by transverse matrix cracking," *Ultrasonics,* vol. 29, pp. 245-251, 1991.

[16]   M. R. Gorman and W. H. Prosser, "AE source orientation by plate wave analysis," *Journal of Acoustic Emission (USA),* vol. 9, pp. 282-288, 1990.

[17]   M. Lemistre and D. Balageas, "Structural health monitoring system based on diffracted Lamb wave analysis by multiresolution processing," *Smart Materials and Structures,* vol. 10, pp. 504-511, 2001.

[18]   N. Hu*, et al.*, "Identification of delamination position in cross-ply laminated composite beams using S0 Lamb mode," *Composites Science and Technology,* vol. 68, pp. 1548-1554, 2008.

[19]   F. Li*, et al.*, "Optimal mother wavelet selection for Lamb wave analyses," *Journal of Intelligent Material Systems and Structures,* vol. 20, pp. 1147-1161, 2009.

[20]   S. Salamone*, et al.*, "Temperature effects in Lamb-wave structural health monitoring systems," *Proc. SPIE 7295, Health Monitoring of Structural and Biological Systems,* vol. 7295 pp. 72950O1-11, 2009.

[21]   Y. Okabe*, et al.*, "Delamination detection in composite laminates using dispersion change based on mode conversion of Lamb waves," *Smart Materials and Structures,* vol. 19, 115013, 2010.

[22]   V. Giurgiutiu, "Lamb wave generation with piezoelectric wafer active sensors for structural health monitoring," *Smart Structures and Materials 2003,* vol. 5056, pp. 111-122, 2003.

[23]   V. Giurgiutiu, *Structural health monitoring: with piezoelectric wafer active sensors*: Academic Press, MA USA, 2007.

[24]   http://www.fujicera.co.jp/product/e/index.html

[25]   H. A. Sodano, "Macro-fiber composites for sensing, actuation and power generation," Thesis in Virginia Polytechnic Institute and State University, 2003.

[26]   M. Eaton*, et al.*, "Use of macro fibre composite transducers as acoustic emission sensors," *Remote Sensing,* vol. 1, pp. 68-79, 2009.

[27]   R. B. Williams*, et al.*, "Nonlinear tensile and shear behavior of macro fiber composite actuators," *Journal of Composite Materials,* vol. 38, pp. 855-869, 2004.

[28]   R. Chen*, et al.*, "Linear location of acoustic emission using a pair of novel fibre optic sensors," *Measurement Science and Technology,* vol. 17, pp. 2313-2318, 2006.

[29]   W. B. Spillman Jr, "Multimode fiber-optic hydrophone based on a schlieren technique," *Applied Optics,* vol. 20, pp. 465-470, 1981.

[30]   W. B. Spillman Jr and R. Gravel, "Moving fiber-optic hydrophone," *Optics Letters,* vol. 5, pp. 30-31, 1980.

[31]   J. Bucaro, "Optical Fiber Acoustic Sensors," in *Fiber Optics*, Springer, pp. 641-655, 1979.

[32]   J. Bucaro and E. Carome, "Single fiber interferometric acoustic sensor," *Applied Optics,* vol. 17, pp. 330-331, 1978.

[33]   M. Imai*, et al.*, "Fiber-optic Michelson interferometer using an optical power divider," *Optics Letters,* vol. 5, pp. 418-420, 1980.

[34]   E. Udd, "Fiber-optic acoustic sensor based on the Sagnac interferometer," *Proc. SPIE 0425, Single Mode Optical Fibers*, 90, 1983.

[35]   K. Liu and S. M. Ferguson, "Fiber-optic interferometric sensor for the detection of acoustic emission within composite materials," *Optics Letters,* vol. 15, pp. 1255-1257, 1990.

[36]   B. O. Guan*, et al.*, "Polarimetric heterodyning fiber grating laser sensors," *Journal of Lightwave Technology,* vol. 30, pp. 1097-1112, 2012.

[37]   T. Erdogan, "Fiber grating spectra," *Journal of Lightwave Technology,* vol. 15, pp. 1277-1294, 1997.

[38]   A. D. Kersey*, et al.*, "Fiber grating sensors," *Journal of Lightwave Technology,* vol. 15, pp. 1442-1463, 1997.

[39]   A. Othonos, "Fiber Bragg gratings," *Review of Scientific Instruments,* vol. 68, pp. 4309-4341, 1997.

[40]   K. O. Hill and G. Meltz, "Fiber Bragg grating technology fundamentals and overview," *Journal of Lightwave Technology,* vol. 15, pp. 1263-1276, 1997.

[41]   H. Tsuda, "Ultrasound and damage detection in CFRP using fiber Bragg grating sensors," *Composites Science and Technology,* vol. 66, pp. 676-683, 2006.

[42]   Y. Sano and T. Yoshino, "Fast optical wavelength interrogator employing arrayed waveguide grating for distributed fiber Bragg grating sensors," *Journal of Lightwave Technology,* vol. 21, pp. 132-139, 2003.

[43]   P. Niewczas*, et al.*, "Performance analysis of the fiber Bragg grating interrogation system based on an arrayed waveguide grating," *IEEE Transactions on Instrumentation and Measurement,* vol. 53, pp. 1192-1196, 2004.

[44]   N. Takeda*, et al.*, "Development of smart composite structures with small-diameter fiber Bragg grating sensors for damage detection: Quantitative evaluation of delamination length in CFRP laminates using Lamb wave sensing," *Composites Science and Technology,* vol. 65, pp. 2575-2587, 2005.

[45]   M. Davis and A. Kersey, "Matched-filter interrogation technique for fibre Bragg grating arrays," *Electronics Letters,* vol. 31, pp. 822-823, 1995.

[46]   A. Lobo Ribeiro*, et al.*, "Analysis of the reflective-matched fiber Bragg grating sensing interrogation scheme," *Applied Optics,* vol. 36, pp. 934-939, 1997.

[47]   W. Jin, "Investigation of interferometric noise in fiber-optic Bragg grating sensors by use of tunable laser sources," *Applied Optics,* vol. 37, pp. 2517-2525, 1998.

[48]   B. Lissak*, et al.*, "Highly sensitive dynamic strain measurements by locking lasers to fiber Bragg gratings," *Optics Letters,* vol. 23, pp. 1930-1932, 1998.

[49]   A. Arie*, et al.*, "Static fiber-Bragg grating strain sensing using frequency-locked lasers," *Journal of Lightwave Technology,* vol. 17, pp. 1849-1855, 1999.

[50]   J.-R. Lee and H. Tsuda, "A novel fiber Bragg grating acoustic emission sensor head for mechanical tests," *Scripta Materialia,* vol. 53, pp. 1181-1186, 2005.

[51]   H. Tsuda*, et al.*, "Acoustic emission measurement using a strain-insensitive fiber Bragg grating sensor under varying load conditions," *Optics Letters,* vol. 34, pp. 2942-2944, 2009.

[52]   A. Rosenthal*, et al.*, "Wideband optical sensing using pulse interferometry," *Optics Express,* vol. 20, pp. 19016-19029, 2012.

[53]   J. Canning and M. Sceats, "π-phase-shifted periodic distributed structures in optical fibres by UV post-processing," *Electronics Letters,* vol. 30, pp. 1344-1345, 1994.

[54]   R. Kashyap*, et al.*, "UV written reflection grating structures in photosensitive optical fibres using phase-shifted phase masks," *Electronics Letters,* vol. 30, pp. 1977-1978, 1994.

[55]   C. Martinez and P. Ferdinand, "Analysis of phase-shifted fiber Bragg gratings written with phase plates," *Applied Optics,* vol. 38, pp. 3223-3228, 1999.

[56]   G. P. Agrawal and S. Radic, "Phase-shifted fiber Bragg gratings and their application to wavelength demultiplexing," *IEEE Photonics Technology Letters,* vol. 6, pp. 995-997, 1994.

[57]   M. LeBlanc*, et al.*, "Transverse load sensing by use of pi-phase-shifted fiber Bragg gratings," *Optics Letters,* vol. 24, pp. 1091-1093, 1999.

[58]   A. Minardo*, et al.*, "Response of fiber Bragg gratings to longitudinal ultrasonic waves," *IEEE Transactions on Ultrasonics, Ferroelectrics and Frequency Control,* vol. 52, pp. 304-312, 2005.

[59]   Z. Li*, et al.*, "Analysis of ultrasonic frequency response of surface attached fiber Bragg grating," *Applied Optics,* vol. 51, pp. 4709-4714, 2012.

[60]   T. Liu and M. Han, "Analysis of π-phase-shifted fiber Bragg gratings for ultrasonic detection," *IEEE Sensors Journal,* vol. 12, pp. 2368-2373, 2012.

[61]   A. Rosenthal*, et al.*, "High-sensitivity compact ultrasonic detector based on a pi-phase-shifted fiber Bragg grating," *Optics Letters,* vol. 36, pp. 1833-1835, 2011.

[62]   M. Yamada and K. Sakuda, "Analysis of almost-periodic distributed feedback slab waveguides via a fundamental matrix approach," *Applied Optics,* vol. 26, pp. 3474-3478, 1987.

[63]   M. Prabhugoud and K. Peters, "Modified transfer matrix formulation for Bragg grating strain sensors," *Journal of Lightwave Technology,* vol. 22, pp. 2302-2309, 2004.

[64]   A. Rosenthal*, et al.*, "Spatial characterization of the response of a silica optical fiber to wideband ultrasound," *Optics Letters,* vol. 37, pp. 3174-3176, 2012.

[65]   Y. Okabe*, et al.*, "Evaluation of debonding progress in composite bonded structures using ultrasonic waves received in fiber Bragg grating sensors," *Smart Materials and Structures,* vol. 16, pp. 1370-1378, 2007.

[66]   Q. Wu*, et al.*, "Sensitivity distribution properties of a phase-shifted fiber Bragg grating sensor to ultrasonic waves," *Sensors,* vol. 14, pp. 1094-1105, 2014.

[67]   R. J. Van Steenkiste and G. S. Springer, *Strain and temperature measurement with fiber optic sensors*: CRC press, 1997.

[68]   M. Feldman, "Hilbert transform in vibration analysis," *Mechanical Systems and Signal Processing,* vol. 25, pp. 735-802, 2011.

[69]   G. Qi, "Wavelet-based AE characterization of composite materials," *NDT & E International,* vol. 33, pp. 133-144, 2000.

[70]   J. R. Lee*, et al.*, "Impact wave and damage detections using a strain-free fiber Bragg grating ultrasonic receiver," *NDT & E International,* vol. 40, pp. 85-93, 2007.

[71]   I. Perez*, et al.*, "High frequency ultrasonic wave detection using fiber Bragg gratings," *SPIE*

7th Annual International Symposium on Smart Structures and Materials, Mar. 2000.

[72]   I. Perez, "Acoustic emission detection using fiber Bragg gratings," *Proc. SPIE*, vol. 4328, pp. 209–215, 2001.

[73]   A. I. Azmi, *et al.*, "Performance Enhancement of Vibration Sensing Employing Multiple Phase-Shifted Fiber Bragg Grating," *Journal of Lightwave Technology,* vol. 29, pp. 3453-3460, 2011.

[74]   Q. Wu and Y. Okabe, "Ultrasonic sensor employing two cascaded phase-shifted fiber Bragg gratings suitable for multiplexing," *Optics Letters,* vol. 37, pp. 3336-3338, 2012.

[75]   Q. Wu and Y. Okabe, "Novel real-time acousto-ultrasonic sensors using two phase-shifted fiber Bragg gratings," *Journal of Intelligent Material Systems and Structures, doi: 10.1177/1045389X13483028* 2013.

[76]   D. Robertson, *et al.*, "Interrogation of a dual-fiber-Bragg-grating sensor using an arrayed waveguide grating," *IEEE Transactions on Instrumentation and Measurement,* vol. 56, pp. 2641-2645, 2007.

[77]   G. Wild and S. Hinckley, "A transmit reflect detection system for fibre Bragg grating acoustic emission and transmission sensors," *Smart Sensors and Sensing Technology,* pp. 183-197, 2008.

[78]   J. H. Chow, *et al.*, "Laser frequency-noise-limited ultrahigh resolution remote fiber sensing," *Optics Express,* vol. 14, pp. 4617-4624, 2006.

[79]   D. Gatti, *et al.*, "Fiber strain sensor based on a pi-phase-shifted Bragg grating and the Pound-Drever-Hall technique," *Optics Express,* vol. 16, pp. 1945-1950, 2008.

[80]   S. Avino, *et al.*, "Musical instrument pickup based on a laser locked to an optical fiber resonator," *Optics Express,* vol. 19, pp. 25057-25065, 2011.

[81]   Q. Wu and Y. Okabe, "High-sensitivity ultrasonic phase-shifted fiber Bragg grating balanced sensing system," *Optics Express,* vol. 20, pp. 28353-28362, 2012.

[82]   http://assets.newport.com/webDocuments-EN/images/15192.pdf

[83]   M. Saiful Islam, *et al.*, "Distributed balanced photodetectors for broad-band noise suppression," *IEEE Transactions on Microwave Theory and Techniques,* vol. 47, pp. 1282-1288, 1999.

[84]   A. Joshi, *et al.*, "Balanced photoreceivers for analog and digital fiber optic communications," *Proc. SPIE 5814, Enabling Photonics Technologies for Defense, Security, and Aerospace Applications*, vol. 39, pp. 39-50, 2005.

[85]   H. Tsuda, K. Kumakura, and S. Ogihara, "Ultrasonic sensitivity of strain-insensitive fiber Bragg grating sensors and evaluation of ultrasound-induced strain," *Sensors,* vol. 10, pp. 11248-11258, 2010.

[86]   L. Rippert, *et al.*, "Optical and acoustic damage detection in laminated CFRP composite materials," *Composites Science and Technology,* vol. 60, pp. 2713-2724, 2000.

[87]   I. Read, *et al.*, "Optical fibre acoustic emission sensor for damage detection in carbon fibre composite structures," *Measurement Science and Technology,* vol. 13, pp. N5-N9, 2001.

[88]   T. Fu, *et al.*, "Fiber optic acoustic emission sensor and its applications in the structural health monitoring of CFRP materials," *Optics and Lasers in Engineering,* vol. 47, pp. 1056-1062, 2009.

[89]   Raju, *et al.*, "Acoustic emission techniques for failure charactreisation in composite top-hat stiffeners," *Journal of Reinforced Plastics and Composites,* vol. 37, pp. 495-516, 2012.

[90]   T. Prasse, *et al.*, "A comparative investigation of electrical resistance and acoustic emission during cyclic loading of CFRP laminates," *Composites Science and Technology,* vol. 61, pp. 831-835, 2001.

[91]   M. Surgeon and M. Wevers, "Modal analysis of acoustic emission signals from CFRP laminates," *NDT & E International*, vol. 32, pp. 311-322, 1999.

[92]   M. Johnson and P. Gudmundson, "Broad-band transient recording and characterization of acoustic emission events in composite laminates," *Composites Science and Technology,* vol. 60, pp. 2803-2818, 2000.

[93]   P. Liu, *et al.*, "A study on the failure mechanisms of carbon fiber/epoxy composite laminates using acoustic emission," *Materials & Design*, vol. 37, pp. 228-235, 2012.

[94]   P. J. De Groot, P. A. Wijnen, and R. B. Janssen, "Real-time frequency determination of acoustic emission for different fracture mechanisms in carbon/epoxy composites," *Composites Science and Technology*, vol. 55, pp. 405-412, 1995.

[95]   J. Chen, *et al.*, "New insights into the noise reduction Wiener filter," *IEEE Transactions on Audio, Speech, and Language Processing,* vol. 14, pp. 1218-1234, 2006.

[96]   S. M. Ziola, "Source location in thin plates using cross correlation," Doctoral thesis, Naval Postgraduate School Monterey CA USA, 1991.

[97]   J. Jiao, B. Wu, and C. He, "Acoustic emission source location methods using mode and frequency analysis," *Structural Control and Health Monitoring,* vol. 15, pp. 642-651, 2008.

[98]   H. Tsuda, "Fiber Bragg grating vibration-sensing system, insensitive to Bragg wavelength and employing fiber ring laser," *Optics Letters,* vol. 35, pp. 2349-2351, 2010.

[99]   C. R. Giles and E. Desurvire, "Modeling erbium-doped fiber amplifiers," *Journal of Lightwave Technology,* vol. 9, pp. 271-283, 1991.

[100] E. Desurvire, D. Bayart, B. Desthieux, and S. Bigo, *Erbium-doped fiber amplifiers: Device and System Developments* vol. 2: Wiley-Interscience, 2002.

[101] Z. Meng, G. Stewart, and G. Whitenett, "Stable single-mode operation of a narrow-linewidth, linearly polarized, erbium-fiber ring laser using a saturable absorber," *Journal of Lightwave Technology,* vol. 24, pp. 2179-2183, 2006.

[102] X. Chen, Z. Deng, and J. Yao, "Photonic generation of microwave signal using a dual-wavelength single-longitudinal-mode fiber ring laser," *IEEE Transactions on Microwave Theory and Techniques,* vol. 54, pp. 804-809, 2006.

[103] S. Pan and J. Yao, "A wavelength-switchable single-longitudinal-mode dual-wavelength erbium-doped fiber laser for switchable microwave generation," *Optics Express,* vol. 17, pp. 5414-5419, 2009.

[104] B. Y. Kim, "Fiber lasers for sensing," *SPIE European Workshop on Optical Fibre Sensors*, Vol. 3483, pp. 12-19, 1998.

[105] Q. Mao and J. W. Lit, "Multiwavelength erbium-doped fiber lasers with active overlapping linear cavities," *Journal of Lightwave Technology,* vol. 21, pp. 160-169, 2003.

[106] P. C. Peng, K. M. Feng, W. R. Peng, H. Y. Chiou, C. C. Chang, and S. Chi, "Long-distance fiber grating sensor system using a fiber ring laser with EDWA and SOA," *Optics Communications,* vol. 252, pp. 127-131, 2005.

[107] E. Lacot, F. Stoeckel, and M. Chenevier, "Dynamics of an erbium-doped fiber laser," *Physical Review A,* vol. 49, pp. 3997-4008, 1994.

[108] G. Stewart, G. Whitenett, K. Vijayraghavan, and S. Sridaran, "Investigation of the dynamic response of erbium fiber lasers with potential application to sensors," *Journal of Lightwave Technology,* vol. 25, pp. 1786-1796, 2007.

[109] M. A. Mirza and G. Stewart, "Multiwavelength operation of erbium-doped fiber lasers by periodic filtering and phase modulation," *Journal of Lightwave Technology,* vol. 27, pp. 1034-1044, 2009.

[110] M. Han, T. Liu, L. Hu, and Q. Zhang, "Intensity-demodulated fiber-ring laser sensor system for acoustic emission detection," *Optics Express,* vol. 21, pp. 29269-29276, 2013.

[111] T. Liu, L. Hu, and M. Han, "Multiplexed fiber-ring laser sensors for ultrasonic detection," *Optics Express,* vol. 21, pp. 30474-30480, 2013.

[112] Y. Sun, J. Zyskind, and A. Srivastava, "Average inversion level, modeling, and physics of erbium-doped fiber amplifiers," *IEEE Journal of Selected Topics in Quantum Electronics,* vol. 3, pp. 991-1007, 1997.

[113] M. Dinand and C. Schutte, "Theoretical modeling of relaxation oscillations in Er-doped waveguide lasers," *Journal of Lightwave Technology,* vol. 13, pp. 14-23, 1995.

[114] M. Ding and P. K. Cheo, "Analysis of Er-doped fiber laser stability by suppressing relaxation oscillation," *IEEE Photonics Technology Letters,* vol. 8, pp. 1151-1153, 1996.

[115]   W. Thomson, *Theory of vibration with applications*: Prentice-Hall, 1996.

[116]   E. Rønnekleiv, "Frequency and intensity noise of single frequency fiber Bragg grating lasers," *Optical Fiber Technology,* vol. 7, pp. 206-235, 2001.

[117]   C. C. Ye and R. P. Tatam, "Ultrasonic sensing using Yb3+/Er3+-codoped distributed feedback fibre grating lasers," *Smart Materials and Structures,* vol. 14, pp. 170-176, 2005.

ACKNOWLEDGEMENTS

Furthermore, I would like to extend these acknowledgements to all the friends and people who helped me during these three years, e.g., the friends from Japan-China Friendship Center, the friends from Department of Systems Innovation, the friends from the Institute of Industrial Science. They were always ready to help when I needed it. It is my pleasure to meet you in my living overseas. I will always remember our friendship in future.

Finally, I would like to thank my whole family. My parents, Hangui Wu and Heying Jiang, gave me enough understanding and supports in my entire research process. It is my honor to be your child. I also want to say thank you to my wife, Siyuan Chen for being the most important person in my life and her encouragement and dedication to the whole family.

PUBLICATIONS

(a) Journal Papers

[1]   **Qi Wu*** and Yoji Okabe, Investigation of dynamic properties of erbium fiber laser for ultrasonic sensing, *Optics Express*, 2014, 22(7), 8405-8419.

[2]   **Qi Wu*** and Yoji Okabe, Novel real-time acousto-ultrasonic sensors using two phase-shifted fiber Bragg gratings, *Journal of Intelligent Material Systems and Structures*, 2014, 25(5), 640-646.

[3]   **Qi Wu*,** Yoji Okabe, Kazuya Saito and Fengming Yu, Sensitivity distribution properties of a phase-shifted fiber Bragg grating sensor to ultrasonic waves, *Sensors*, 2014, 14(1), 1094-1105.

[4]   **Qi Wu*** and Yoji Okabe, High-sensitivity ultrasonic phase-shifted fiber Bragg grating balanced sensing system, *Optics Express*, 2012, 20(27), 28353-28362.

[5]   **Qi Wu*** and Yoji Okabe, Ultrasonic sensor employing two cascaded phase-shifted fiber Bragg gratings suitable for multiplexing, *Optics Letters*, 2012, 37(16), 3336-3338.

(b) Conference Papers

[1]   **Qi Wu***, Yoji Okabe and Junqiang Sun, Novel optical fiber ultrasonic sensor based on fiber laser, SPIE's 21st Annual International Symposium on Smart Structures and Material Systems + Nondestructive Evaluation and Health Monitoring (SPIE Smart Structures/NDE), March 9~13, 2014, San Diego, USA.

[2]   **Qi Wu*** and Yoji Okabe, Impact damage detection in composite materials by novel laser-sensor system, Proceedings of Japan Conference for Composite Materials-5, March 4~6, 2014, Kyoto, Japan.

[3]   Fengming Yu*, Yoji Okabe, **Qi Wu**, Satoshi Kobayashi and Kazuya Saito, Identification of Damage Types in CFRP laminates from AE signals detected by a new optical fiber sensor, Symposium on Non-Destructive Inspection with Ultrasonic Wave, 1-3, January 20~21, 2014, Tokyo, Japan.

[4]   **Qi Wu***, Fengming Yu, Yoji Okabe, Satoshi Kobayashi and Kazuya Saito, AE detection in CFRP composites by a novel optical fiber sensor, M&P 2013, 311, November 8~10, 2013, Tokyo, Japan.

[5]   Fengming Yu*, **Qi Wu**, Yoji Okabe, Satoshi Kobayashi and Kazuya Saito, Evaluation of AE signals detected by an optical fiber sensor to identify the damage in composites, M&P 2013, 323, November 8~10, 2013, Tokyo, Japan.

[6]   **Qi Wu***, Fengming Yu, Yoji Okabe, Kazuya Saito and Satoshi Kobayashi, Acoustic emission detection in CFRP cross-ply laminates by novel PS-FBG optical fiber ultrasonic sensor, Proceedings of 38th Symposium on Composite Materials, A1-1-4 17, September 24&26, 2013, Kagoshima, Japan.

[7]   **Qi Wu***, Yoji Okabe, Fengming Yu and Kazuya Saito, Ultrasensitive optical-fiber ultrasonic sensor based on phase-shifted fiber Bragg gratings, 9th International Workshop on Structural Health Monitoring, 2063, September 10~12, 2013, Stanford, USA.

[8] **Qi Wu***, Fengming Yu, Kazuya Saito, Yoji Okabe and Satoshi Kobayashi, Phase-shifted fiber Bragg grating balanced sensing system for detection of acoustic emission, 3rd International Symposium on Laser Ultrasonics and Advanced Sensing, 1B4 53, June 25~28, 2013, Yokohama, Japan.

[9] Fengming Yu*, **Qi Wu**, Yoji Okabe, Kazuya Saito and Satoshi Kobayashi, Application of a novel optical fiber sensing system to acoustic emission detection in CFRP laminates, 3rd International Symposium on Laser Ultrasonics and Advanced Sensing, 94, June 25~28, 2013, Yokohama, Japan.

[10] **Qi Wu***, Fengming Yu, Yoji Okabe and Kazuya Saito, High sensitive PS-FBG ultrasonic sensor for SHM of composite materials, Proceedings of Japan Conference for Composite Materials-4, 2A-12, March 7~9, 2013, Tokyo, Japan.

[11] **Qi Wu***, Fengming Yu and Yoji Okabe, High sensitive optical sensing system based on phase-shifted FBG to detect AE signals and impacts in CFRP laminates, Proceedings of 37th Symposium on Composite Materials, C-9 105-106, October 18~19, 2012, Nagoya, Japan.

[12] **Qi Wu*** and Yoji Okabe, Novel acoustic emission sensor system based on two cascaded phase-shifted fiber Bragg gratings, 22nd International Conference on Optical Fiber Sensors, Proc. SPIE 8421, October 15~19, 2012, Beijing, China.

[13] **Qi Wu*** and Yoji Okabe, Novel real-time acousto-ultrasonic sensor system using two phase-shifted FBGs, Proceedings of Advances in Structural Health Management and Composite Structures 2012, Volume I, P09, August 29~31, 2012, Jeonju, Republic of Korea.

[14] Fengming Yu*, **Qi Wu**, Yoji Okabe, Satoshi Kobayashi and Kazuya Saito, Identification of damage types in carbon fiber reinforced plastic laminates by a novel optical fiber acoustic emission sensor, 7th European Workshop on Structural Health Monitoring, July 8~11, 2014, Nantes, France.

PATENTS

[1] Hideki Soejima, Yoji Okabe, **Qi Wu**, Vibration detection device and vibration detection method, No.2014/039087, Japan, 2014.

[2] Yoji Okabe, **Qi Wu**, Hideki Soejima, Koji Omichi, Displacement measuring device and displacement measuring method, No.13/959076, USA, 2013.

[3] Yoji Okabe, **Qi Wu**, Hideki Soejima, Koji Omichi, Displacement measuring device and displacement measuring method, No.2013/020928, Japan, 2013.